NOTE TO USERS

DISSERTATION

TEMPLATE SYNTHESIS OF ONE-DIMENSIONAL PEROVSKITES (ABO_3): THE EFFECTS OF GRAIN SIZE AND ASPECT RATIO ON THE ELECTRONIC PROPERTIES

Submitted by

Bernadette A. Hernandez-Sanchez

Chemistry Department

In partial fulfillment of the requirements

For the Degree of Doctor in Philosophy

Colorado State University

Fort Collins, Colorado

Fall 2004

COLORADO STATE UNIVERSTIY

June 16, 2004

WE HERBY RECOMMEND THAT THE DISERTATION PREPARED UNDER OUR SUPERVISION BY BERNADETTE A. HERNANDEZ-SANCHEZ ENTITLED TEMPLATE SYNTHESIS OF ONE-DIMENSIONAL PEROVSKITES (ABO_3): THE EFFECTS OF GRAIN SIZE AND ASPECT RATIO ON THE ELECTRONIC PROPERTIES BE ACCEPTED AS FULLIFILLING IN PART REQUIRMENTS FOR THE DEGREE OF DOCTOR OF PHILOSOPHY.

Committee on Graduate Work

S. A. Lee

R. G. Finke

G. Szamel

E. R. Fisher/Co-Advisor

P. K. Dorhout/Co-Advisor

A. K. Rappe/ Department Head

ABSTRACT OF DISSERTATION

TEMPLATE SYNTHESIS OF ONE-DIMENSIONAL PEROVSKITES (ABO_3): THE EFFECTS OF GRAIN SIZE AND ASPECT RATIO ON THE ELECTRONIC PROPERTIES

Metal oxides, that have the perovskite (ABO_3) crystal structure, are versatile materials known for their dielectric (paraelectric), ferroelectric, magnetic, piezoelectric, optic, and superconductivity. The phase or symmetry of the unit cell, concentrations of the cations within solid solutions, and defects in the crystalline lattice, can influence these properties. Thus, it is imperative to understand how crystal chemistry is affected by nanoscaling. A plethora of compounds within the perovskite family exist, however; this work has focused on a few choice pervoskites known for being examples of paraelectric, ferroelectric, antiferroelectric, and magnetic materials. Barium titanate ($BaTiO_3$), strontium titanate ($SrTiO_3$), lead titanate ($PbTiO_3$), lead zirconate ($PbZrO_3$), and neodymium nickelate ($NdNiO_3$) were chosen for this study. Template synthesis was used to fabricate one-dimensional materials for the investigation on the effects of grain size, crystallite size, and aspect ratio upon the physical properties of the perovskites.

This dissertation reports on the sol-gel template synthesis and characterization of the first perovskite nanotubes. Methods were further developed to include the formation of perovskite nanofibers. Chelate and Pechini sol-gel routes were employed to coat inorganic and organic membrane templates. Nanotubes were formed within 200 nm pore Whatman anodisc aluminum oxide membranes. Both nanotubes and nanofibers were prepared using 50, 100, and 200 nm Whatman track-etched polycarbonate membranes. Electron microscopy revealed that morphology depended upon the selection of templates employed, concentration of the precursor sol-gel, and crystallization conditions.

A fundamental study of how grain/crystallite size and aspect ratio of the one dimensional morphologies affect the electronic phase transitions were monitored through the comparison of bulk powders to nanostructured materials using electron diffraction, X-ray diffraction, Raman spectroscopy, differential scanning calorimetry, and UV-visible optical diffuse reflectance spectroscopy. Results indicated that the perovskites synthesized through the templates used in this research did not show significant deviations in their properties from the bulk control powders except in crystallite sizes formed.

Bernadette A. Hernandez-Sanchez
Department of Chemistry
Colorado State University
Fort Collins, CO 80523
Fall 2004

ACKNOWLEDGMENTS

I believe in the philosophy that it takes a community of people to help intellectually raise an individual to their success. And I am sincerely thankful for those significant individuals who have graciously passed down their knowledge and expertise to help me achieve success in my education and in research. To my advisors, Ellen R. Fisher and Peter K. Dorhout, thank you for patience, support, and your passion to teach. Your enthusiasm for chemistry and teaching, both in and outside the classroom, was inspirational. To past and present group members, I had an awesome time working and learning alongside of you. All of you were my eyes and ears for many practice talks and group meetings. To my closest group member, Ina T. Martin, your support and friendship made my graduate school experience special. I am glad that we were able to help each other and experience all the "hoops" together. I extend my gratitude to John Chandler, Sandeep Kohli, Pat McCurdy, and Jennifer Burris for their technical support. And acknowledge The Department of Energy and Colorado AGEP for financial support of my research. Finally, to Timothy J. Boyle, who took a chance on a kid from Rio Grande High School to work at the Advanced Materials Laboratory and showed me how fun chemistry is. You initiated the path towards my career.

DEDICATION

Para mi familia. To my loving husband Andres Sanchez. I love you! Thank you for supporting my decisions, motivating me, and believing in me. To Dusty and Taylor for being silly dogs and making me laugh. To my sisters and brothers: Nicolette M. Hernandez, Eduardo D. B. Vigil, Joseph I. Hernandez, Sarah, D. M. Vigil, Rebecca P. A. Vigil, and Isaiah D. Hernandez. To my niece Zion D. Hernandez. Talking and laughing with you on the phone while we were apart always made me feel better when I was homesick. My parents: Yolanda M. Vigil, Daniel L. Vigil, Joseph R. Hernandez, and Deborah A. Hernandez. And to my grandmother Emma C. Gabaldon. Each of you, in your own way, has helped me to finish school. Thank you for your love, support, and prayers while I finished. And finally to my heavenly father, who blessed me with my experiences, family, friends, and those who have helped me to succeed.

TABLE OF CONTENTS

LIST OF FIGURES

LIST OF TABLES

ABBREVIATIONS

Å	Angstroms
°C	Centigrade
nm	Nanometers
μm	Microns
PXRD	Powder X-ray Diffraction
SEM	Scanning Electron Microscopy
TEM	Transmission Electron Microscopy
EDS	Energy Dispersive X-ray Analysis
AAO	Anodized Aluminum Oxide
PC	Track-Etched Polycarbonate
T_C	Curie Transition Temperature
PE	Paraelectric
FE	Ferroelectic
PL	Photoluminescence
E_g	Optical Band Gap
eV	Electron Volts
STE	Single Trapped Excitation
MI	Metal-Insulator
T_{MI}	Metal-Insulator Transition Temperature

CHAPTER 1

Introduction to One-Dimensional Perovskites

I. One Dimensional Nanostructures.

The synthesis and characterization of nanomaterials have become an important research area across all disciplines of science.[1-3] The major thrusts behind such interest are deviations in the physical properties observed for the nanomaterials in relation to their bulk counter parts. Examples of such phenomena include: quantum confinement effects in semiconductors, increased surface area to volume ratios of cluster catalyst, changes in phase transitions, lattice parameters, melting points, and reductions of domains found in magnetic nanoparticles, to name a few.[3-6] The size regime that affects certain physical properties has defined this area of research. Nanomaterials are conventionally defined as having one measurable length scale of 1-100 nm.[5,7] Features of processed materials, such as particle diameter, grain size, layer thickness, and width of a conducting line on an electronic chip, have been applied to this length scale.[5] In addition to their length scale, nanomaterials have also been categorized by their dimensionality.

The dimensionality of nanomaterials ranges from zero to three. In mathematics, dimension is defined as the property of vector space or the extension in a given direction and has been applied to categorize the morphologies of the nanostructures generated.[8] A zero-dimension is a point in space (quantum dots), one-dimension describes the property of a line (nanowires), two-dimensions describe the property of a plane (quantum wells), and three dimensions describe the property of parallelepipeds (frameworks).[9] One-dimensional (1-D) nanomaterials are typically structures identified as wires, rods, belts, and tubes.[7,10-12]

The interest in 1-D materials was brought about by the initial discovery of the carbon nanotube.[10] Since then, a variety of inorganic materials have been investigated

for the synthesis of these high aspect ratio structures, and are considered technologically relevant systems for the investigation of size effects on thermal or electrical transport and mechanical properties of inorganic materials.[9] Aspect ratio is defined as the relationship between length to diameter for 1-D materials. This definition applies to rods, wires, and fibers, however, this definition is not clear when tubes are discussed because of the presence of an inner and outer diameters. For the purposes of this research, we defined aspect ratio for our tubes as the relationship between the length and outer diameter. A variety of synthetic techniques have been employed to grow inorganic 1-D materials and include: anisotropic growth dictated by the crystallographic structure of a solid material, anisotropic growth confined and directed by various templates, and anisotropic growth kinetically controlled by supersaturation or through the use of an appropriate capping reagent.[7] A key goal for these methods and other synthetic techniques used to produce inorganic nanomaterials is the control of composition, size, and crystallinity.[11] Having synthetic control over the crystal chemistry is crucial in determining structure-property relationships for inorganic systems, and is revelant to the research presented here. In the next sections, the properties of the perovskites and the synthetic techniques developed for this research are presented. Finally, the scope of this research is reviewed.

II. Perovskites and Their Electronic Properties

Before addressing the physical properties of perovskite materials, an understanding of the structure-property relationship must be made. The perovkites are versatile materials known for their dielectric (paraelectric), ferroelectric, magnetic, piezoelectric, optic, superconductivity, and catalytic properties.[13,14] The physical

characteristics dependent on the crystal chemistry of the perovskite synthesized. The symmetry of the unit cell, stoichiometry, and defects in the crystalline lattice material, influence the properties. It is therefore imperative to understand how the crystal chemistry is affected by nanoscaling the pervoskites. There is a plethora of compounds within the perovskite family. However, the work presented here has focused on the synthesis and characterization of a few choice pervoskites known for being examples of paraelectric, ferroelectric, antiferroelectric, and magnetic materials. Barium titanate ($BaTiO_3$), strontium titanate ($SrTiO_3$), lead titanate ($PbTiO_3$), lead zirconate ($PbZrO_3$), and neodymium nickelate ($NdNiO_3$) were chosen for this study.

ABO_3 Crystal Chemistry. An initial examination of the perovskite crystal chemistry begins with a simpler system known as the parent structure.[15] Figures 1.1a. & 1.1b illustrate the polyhedral views of the rhenium oxide (ReO_3) parent structure. Each polyhedra represents the octahedral coordination of ReO_6. Oxygen atoms are represented by small black dots. Networks of polyhedra are made through corner-shared oxygen. To generate the perovskite structure, the addition of A-site cation within the empty Oh holes of the ReO_3 structure is made. The B-site now becomes the octahedral coordination of BO_6. The perovskite structure, Figure 1.1c & 1.1d, illustrate the cubic phase of barium titanate, $BaTiO_3$. The A-Site cation is Ba^{2+} and the polyhedra represent the TiO_6 octahedra. Several of the Ba^{2+} were removed from the unit cell for clarity. The perovskites derive their name and structure from the naturally occurring mineral calcium titanate $CaTiO_3$.[16] $BaTiO_3$ is a prototypical perovskite and can undergo a series of displacive phase transition as the Bravais Lattice symmetry changes.[17] During a displacive transition from the cubic symmetry towards the tetragonal symmetry, the TiO_6

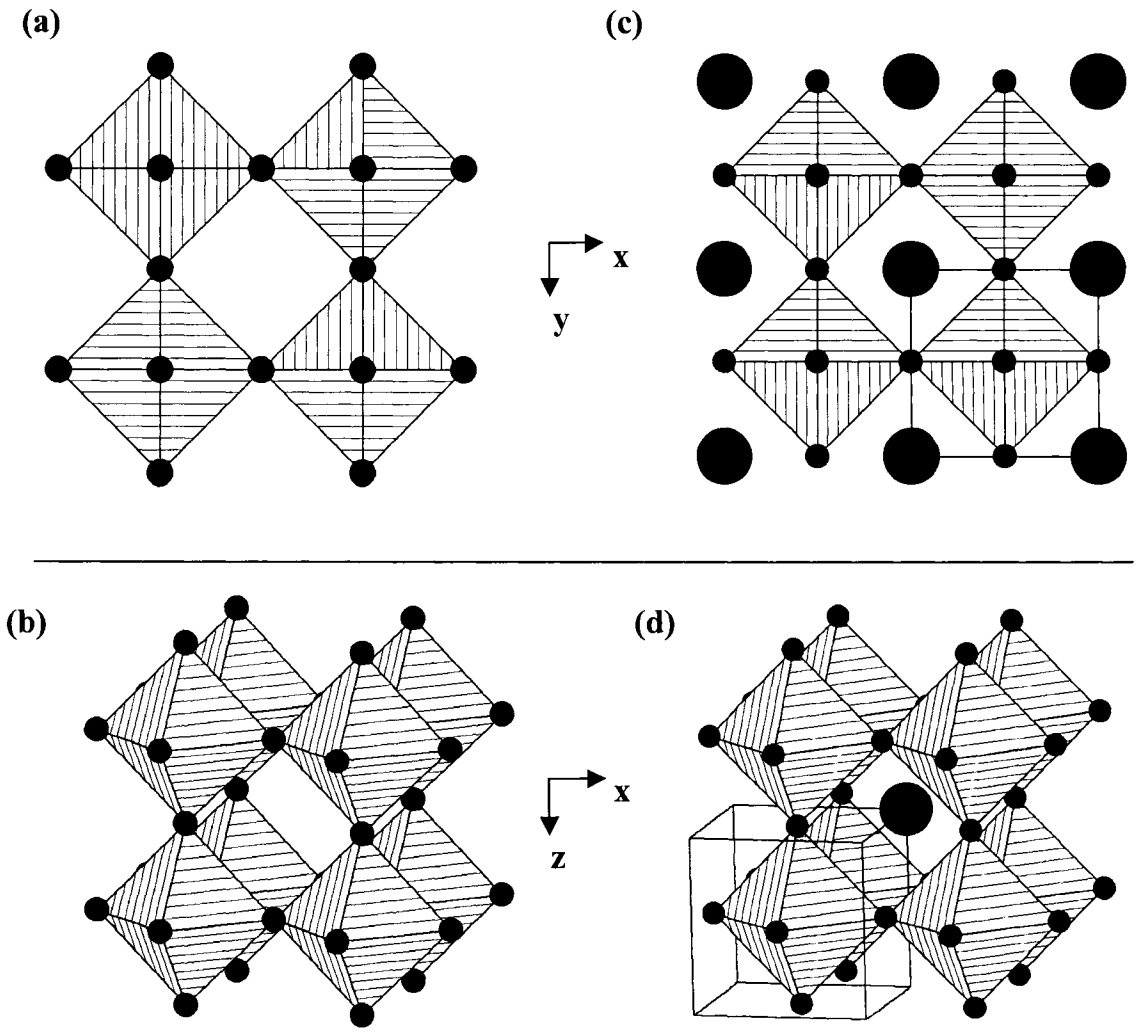

Figure 1.1 Polyhedral top view (a) and side view (b) of the unit cell for the ReO_3 parent structure. Networks of polyhedrons are formed through corner-shared oxygen (small black dots). The perovskites are derived from the ReO_3 structure by the insertion of a cation into Oh holes. (c) Polyhedral top view and (d) side view of the $BaTiO_3$ cubic structure. Large black dots represent Ba^{2+} and polyhedrons represent TiO_6. Several Ba^{2+} have been removed from (d) for clarity.

bond lengths change and the octahedra becomes distorted. Figure 1.2 illustrates the tetragonal unit cell parameters for $PbTiO_3$ and demonstrates the difference in Ti-O bond lengths.[16] $BaTiO_3$ and $PbTiO_3$ can crystallize in both the cubic and tetragonal forms, and are known to have high dielectric constants at room temperature.[18] However, it is the tetragonal form that possesses ferroelectric behavior. The electrical properties of these two phases can be explained in terms of their crystal chemistry.[18]

Ferroelectricity. The electrical properties associated with both the cubic (paraelectric) and tetragonal (ferroelectric) phase is a result of the change in symmetry within the unit cell. The unit cell for the non-polar cubic phase is centrosymmetric and belongs to the point group Pm3m. The symmetry of the polar phase is tetragonal and belongs to the point group P4mm. The lowering of symmetry from the cubic to tetragonal unit cell is a result of the elongation of one cube edge to become the tetragonal c-axis, while the other two cube edges are compressed to become the equivalent tetragonal a-axes (c/a = 1.010), Figure 1.2. The extra room provided in the c axis of the tetragonal unit cell allows for the off centered displacement of the Ti^{+4} within the TiO_6 octahedra. This displacement creates an electric dipole moment within the unit cell and the direction of spontaneous polarization (polar axis) is parallel to the four-fold rotation axis and occurs in the absence of an electric field. This effect is illustrated in Figure 1.3b[17] The direction of the spontaneous polarization, created from the dipole moment, can be changed when an external field is applied.

The net movements of the dipole moments are illustrated by the hysteresis curve, Figure 1.3a. The ferroelectric hysteresis loop represents the polarization of the material as a function of applied electric field. The loop begins at zero applied electric field,

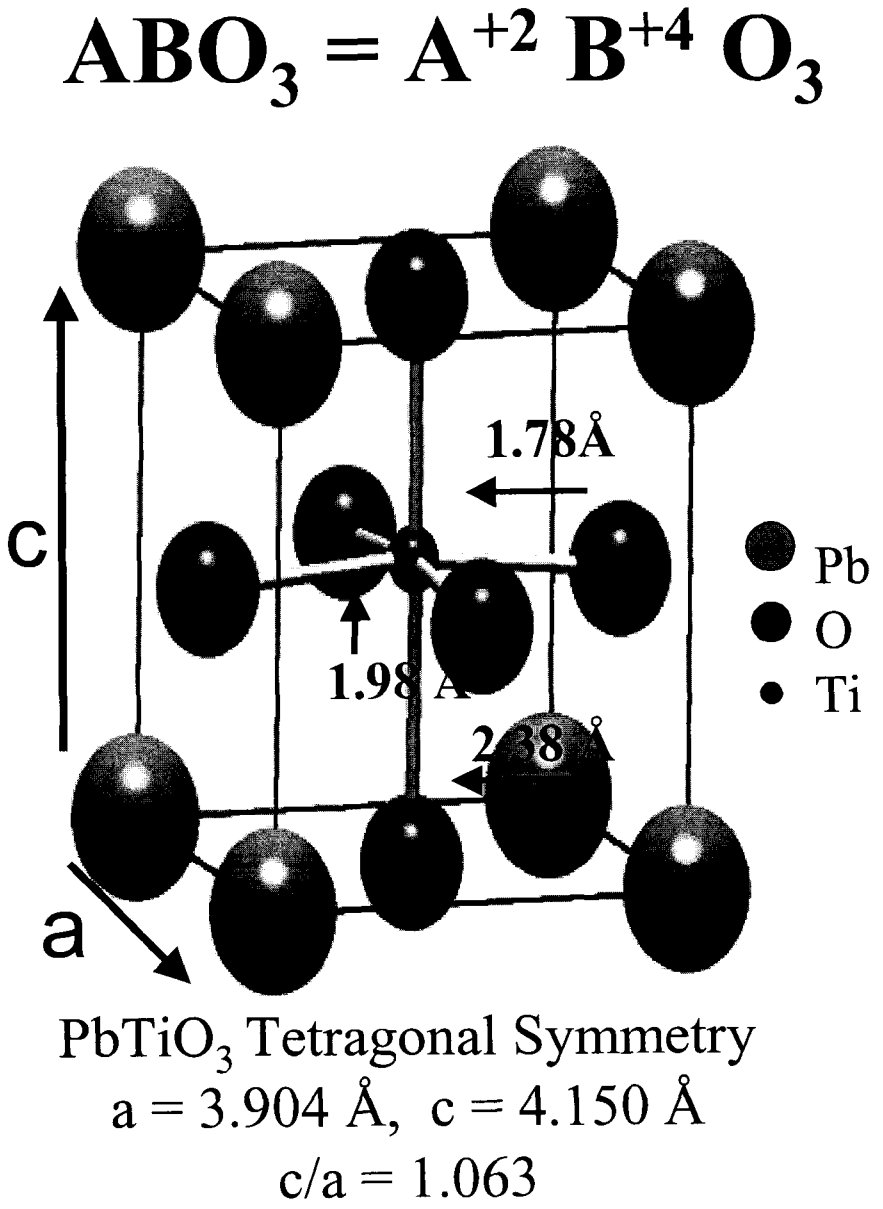

Figure 1.2. $PbTiO_3$ tetragonal unit cell illustrating lattice parameters and bond distances for the TiO_6 octahedra. The non-centrosymmetric unit cell allows for spontaneous polarization.

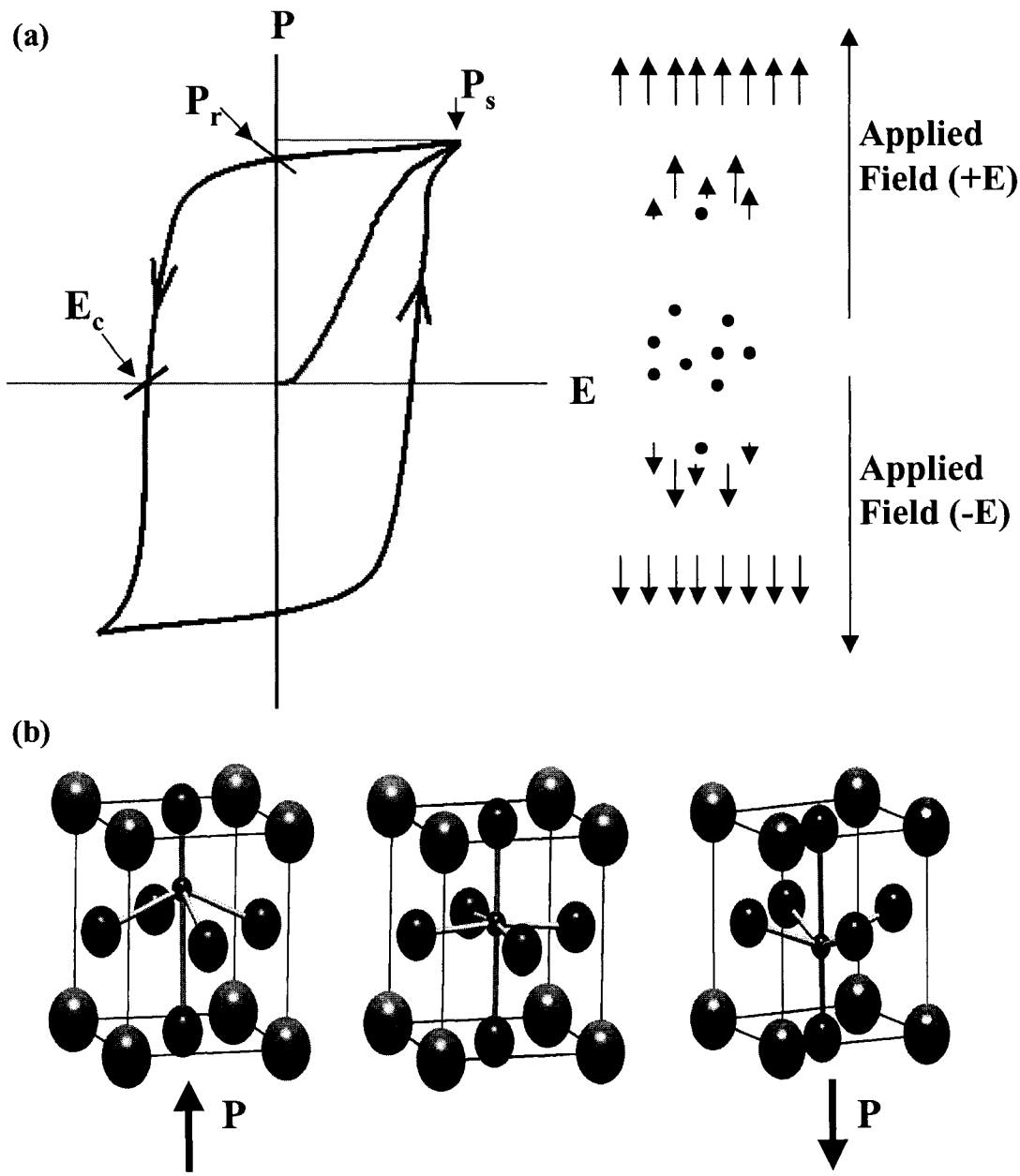

Figure 1.3. (a) Ferroelectric hysteresis curve representing the alignment of dipole moments (polarization) within an applied electric field. (b) Exaggerated cartoon of the TiO6 displacement during hysteresis.

where polarization is in many directions. This point is labeled as Ec, coercive energy. As the positive electric field is applied, cooperative behaviors of dipole moments begin to align . At the applied field where polarization saturation (Ps) occurs, the dipole moments are completely parallel with each other. This is the opposite effect of antiferroelectricity, wherein the dipole moments orient themselves antiparallel to one another. A unique feature of ferroelectric is the ability to retain polarization once the applied field is removed. This point is known as remnant polarization, Pr. This process can be repeated in the negative applied field and the ferroelectric materials can undergo several cycles.

Dielectric (Paraelectricty). A dielectric material is one that is electrically insulating, exhibits or may exhibit an electric dipole structure.[19] These properties are a result of the short range electrical charges under the influence of an applied field. Unlike ferroelectrics, polarization is lost as the applied field is removed. The cubic phase of the perovskite exhibits normal dielectric or paraelectric properties and has the ability to store charge or behave as a capacitor.

III. Size Effects on the Ferroelectric Properties of Perovskites: Investigations on Powders, Nanoparticles, and 1-D Morphologies.

Advances toward nano-scale electronics have created interest in the effects of particle size on the properties of ferroelectric ceramics. These materials are employed for their dielectric, piezoelectric, electrostrictive, pyroelectric, and electrooptic properties, with applications for ferroelectrics accounting for ~60% of the global market for high technology functional ceramics.[1,2] The desirable properties of ferroelectric ceramics arise from their non-centrosymmetric unit cells that produce a polarization state.[3]

Understanding how the crystal structure and state of polarization is influenced by particle size is vital to the performance of ferroelectric ceramics in many applications.

The majority of research on the sources of size effects in ferroelectrics has focused on tetragonal barium titanate ($BaTiO_3$) through investigations of ultra-fine grain powders (< 1 μm), with only a few reports on lead titanate ($PbTiO_3$).[2] The research conducted has demonstrated that size affects the structure-property relationships. As grain size is reduced, there is a decrease in the tetragonal lattice ratio constant (c/a) for room temperature crystal structures.[2,4-7] The main issue with categorizing this effect lies in the synthetic methods. Different synthetic techniques and calcination temperatures influence the grain growth, resulting in widely varying "critical sizes" of $BaTiO_3$. For perovskites, the literature describes critical size as the crystallite size and or grain size where ferroelectric properties diminish.[6] Ultra-fine grained (< 100 μm) ceramic powders are also difficult to prepare because of their high surface areas and agglomeration.[13,16] The reduction in size also changes the ferroelectric to paraelectric transition temperature (T_c ~120 °C) of $BaTiO_3$. Several researchers have reported a lowering of T_c with the synthesis of smaller particles.[2,5,6,8,9]

Two different dielectric behaviors have been observed as the grain size decreases. For grain sizes ranging from about 50 μm to 0.8 μm the dielectric constant generally increases with decreasing grain size.[2,7,10,11] Buessem et al. reported that the increase in permittivity was a result of the absence of 90° twinning, which gives rise to internal stress below T_c.[12] For grains smaller than 0.8 μm there is a decrease in dielectric constant which is not yet fully understood. Arlt et al. have argued that this decrease resulted from changes in crystal structure from tetragonal to cubic with grain size reduction, while Frey

et al. suggested that the decrease was the result of dielectric mixing of interior grain volumes with ferroelectric ordering in the presence of disordered grain-boundary regions.[10,13]

The effects of depolarization in submicron particles have been explained in terms of a randomly oriented surface charge layer that begins to dominate the highly ordered ferroelectric interior as particle size decreases.[5] Eventually, the particle reaches a critical size where polarization becomes zero. Accounting for depolarization and using Landau-Devonshire theory, Wang and co-workers reported a critical size of 44 nm for $BaTiO_3$ particles.[14] Frey et al. reported a smaller critical size and showed experimental ferroelectric behavior in ceramics having grain sizes of 40 nm.[13]

Since these reports, the investigations on the effects of size on the perovskites have evolved with the synthesis of nanoparticles[20,21] (1-20 nm) and 1-D nanostructures.[22-28] Recently, four independent research groups led by Cao, [22-25] Dorhout,[29,30] Park,[26,27] Mallouk,[28] and Wong[31] have reported on the synthesis and characterization of one-dimensional perovskite materials while O'Brien[20] and Zhang[21] have reported on nanoparticle synthesis. The following synthetic techniques were used to form 1-D perovskites: sol-gel electrophoretic deposition into polycarbonate membranes, [22-25] sol-gel template synthesis using capillary action to deposit material in to both aluminum oxide and polycarbonate membranes,[29,30] bimetallic decomposition of alkoxides, [26,27] exfoliation of Ruddelson-Poppler perovskites, [28] and hydrothermal synthesis. [31] Each of these methods, with the exception of decomposition of bimetallic alkoxides generated polycrystalline samples. Of the synthetic techniques, only synthesis with templates had control over apect ratio.

Characterization of $BaTiO_3$, $PbTiO_3$, and $Pb(Zr,Ti)O_4$ nanoparticles and 1-D structures have all identified the cubic paraelectric phase of these materials by X-ray diffraction techniques. Chapter 3 describes the limitations of perovskite crystallite size on X-ray analysis and demonstrates how Raman spectroscopy may be a better analysis tool for determining nanocrystalline symmetry. Surprisingly, probably due to the observation of cubic symmetry by XRD, many have not reported on ferroelectric nature of these materials.

Out of this group of researchers only Park and the research presented in this thesis has investigated the ferroelectric properties of 1-D structures. Both research, has shown that 1-D perovskites have become excellent models to investigate how the ferroelectric crystal structure and state of polarization may be influenced by size and dimensionality by allowing for a unique geometrical constraint on domain behavior. The Park group demonstrated that crystalline single $BaTiO_3$ nanowires with diameters of 10-60 nm could be polarized under vacuum conditions using scanning probe techniques.[27] The wires had ferroelectric domains, with dimensions of several nanometers along the c-axis that were used to write and store information. These results are relevant to the investigation of size effects by experimentally contributing to the identification of a critical size that is lower than what was previously reported. Using particle models, Wang et al., determined the critical size of $BaTiO_3$ by Landau-Devonshire theory to be 44 nm, where as Akdogan et al. experimentally determined this value to be 67 nm through interpolation.[32,33]

Although, polarization results of individual tubes and fibers were not obtained, research presented in this thesis describes the most extensive characterization of electronic phase and composition for nanostructured perovskites through X-ray

diffraction, Raman spectroscopy, differential scanning calorimetry, thermogravametric analysis, mass spectrometry, energy dispersive spectroscopy, and electron imaging techniques. This research has also demonstrated the first reports on perovskite nanotube synthesis using both aluminum oxide and polycarbonate templates. Finally, this research demonstrates the importance of investigating size on structure-property relationships for the nanoregime.

IV. Sol-Gel Template Synthesis

Templates. The template method involves using a material that can serve as a host or mold with a particular net size and shape.[34] Template assisted growth of 1-D materials described in this dissertation occurs within narrow channels of porous materials. Production of our one-dimensional perovskites, described in Chapter 2, was achieved by filling the channels of two types of porous membranes: anodized aluminum oxide (AAO) films and track-etched polycarbonate (PC) films. If completely filled, each template has cylindrical nanochannels that will form fibers, or tubes if they are incompletely filled.[10] Figure 1.4, describe the dimension of the AAO and PC membrane templates. The templates used are commercially available from Whatman. AAO templates can be purchased with a 200 nm and 20 nm pore diameter, and PC templates with 50, 100, and 200 nm pore diameters. Although a 20 nm pore size is available form Whatman, these membranes are asymmetric with 20 nm pore opening that branch out to

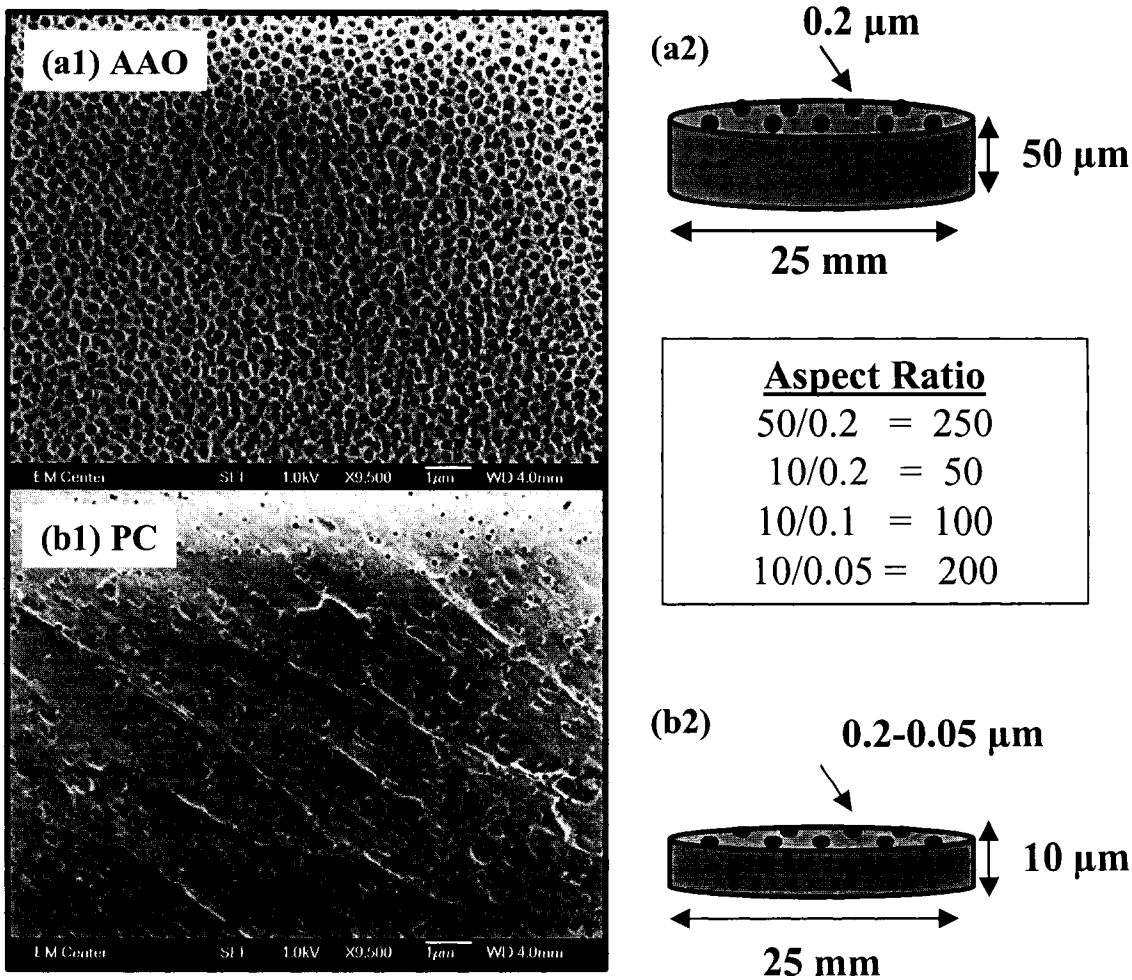

Figure 1.4. SEM images of an untreated Whatman Ò (a1) anodized aluminum oxide (AAO) and (b1) track-etched polycarbonate (PC) membranes (magnification at x9,500). Both templates shown have 200 nm pore channels. The dimensions and aspect ratios of the respective templates are shown in (a2) and (b2).

200-300 nm pore channels. This design allows for efficient liquid flow during filtration but was not useful in changing the aspect ratio of the materials.

Sol-Gel Routes. Sol-gel processing provides an alternative route for the synthesis of metal oxide materials. Perovskites can be prepared through high temperature solid-state reactions between alkaline earth carbonates and transition metal oxides.[35] Under these conditions, polycrystalline powders of relatively large and varied grain sizes along with varying impurity content were formed.[35,36] In contrast, sol-gel techniques require lower processing temperatures, allow for easy compositional control, and can produce polycrystalline samples with smaller particle sizes.[37,38] For example, submicron grain sizes have been reported for both films and powders of the perovskite barium titanate ($BaTiO_3$) made by sol-gel routes.[35,37,39-41] Hence, sol-gel processing is considered an attractive tool for template synthesis of nanostructured materials for two main reasons. First, sol-gel reactions take place at the nanometer level. During synthesis, oligomers or colloids on the order of 0.5-1000 nm form.[38] Second, the sol-gel process can be considered a near net shape process.[5] Materials with various shapes and sizes can be acquired when the sol-gel is set in a template. The two synthetic routes chosen for the synthesis of the perovskite materials generated by this research were the chelate "hybrid" and Pechini methods.

The solution chemistry involved in the sol-gel process to synthesize perovskites (ABO_3) typically involves the hydrolysis and condensation reactions of metal alkoxides, $M(OR)_x$, or metal salts.[14,38] Sol-gel reactions employ organic precursors to aid in chelating or modifying the metallic precursors and provide combustion heat for calcination process. However, the presence of too much organic content will lead to an

increase in calcination temperature.[38] High temperatures are sometimes needed to grow large crystallites or obtain single-phase material. However, in the electronics industry, high temperatures are avoided to keep substrates and other components on electronic chips from being thermally damaged.[35] Sol-gel processes that use low temperature ensure smaller crystallite size, but can contribute to not fully removing organic material, leading to phase impurities, defects, and amorphous materials.[42] Therefore, a balance between precursors and temperatures used in this research was needed.

Sol-Gel Method.[14,38,43] Figure 1.5 outlines the general reaction pathway described for this process. The traditional sol-gel route uses the 2-methoxyethanol as a solvent and undergoes alcohol exchange with the B-site cation precursor, titanium IV butoxide's ligands. The electronegative alkoxide ligand makes titanium highly susceptible to nucleophilic attack by water, and the alcohol exchange is used to slow down this process. The next steps involve the hydrolysis and condensation of the metal alkoxide to form a polymeric network of M-O-M. A second solution of the A-site cation precursor, usually a metal salt such as lead acetate, is dissolved in 2-methoxyethananol is made and refluxed. This method typically requires a long processing time. The two solutions are combined, refluxed, distilled, and diluted to a desired volume. After this step, the solution is then hydrolyzed.

Chelate Method.[14,39,44] In this method, metal alkoxides are modified with a multidentate ligand to help control the sensitivity towards hydrolysis reactions. A typical chelator used is acetic acid. A benefit of using this method is the reduction in time needed to produce the sol. However, this method has been shown to undergo a different reaction pathway known as esterification, Figure 1.6. During this process, ligand

Alcohol Exchange

$Ti(OBu)_4 + 4CH_3O(CH_2)_2OH \longrightarrow Ti[O(CH_2)_2OCH_3]_4 + 4\ BuOH$

Hydrolysis

$M(OR)_X + H_2O \longrightarrow M(OR)_{X-1}(OH) + ROH$

Condensation (alcohol elimination)

$2M(OR)_{X-1}(OH) \longrightarrow M_2O(OR)_{2X-3}(OH) + ROH$

Condensation (water elimination)

$2M(OR)_{X-1}(OH) \longrightarrow M_2O(OR)_{2X-2} + H_2O$

Figure 1.5. Solution chemistry for the sol-gel process using 2-methoxyethanol as reactant and solvent with titaninum (IV) butoxide.

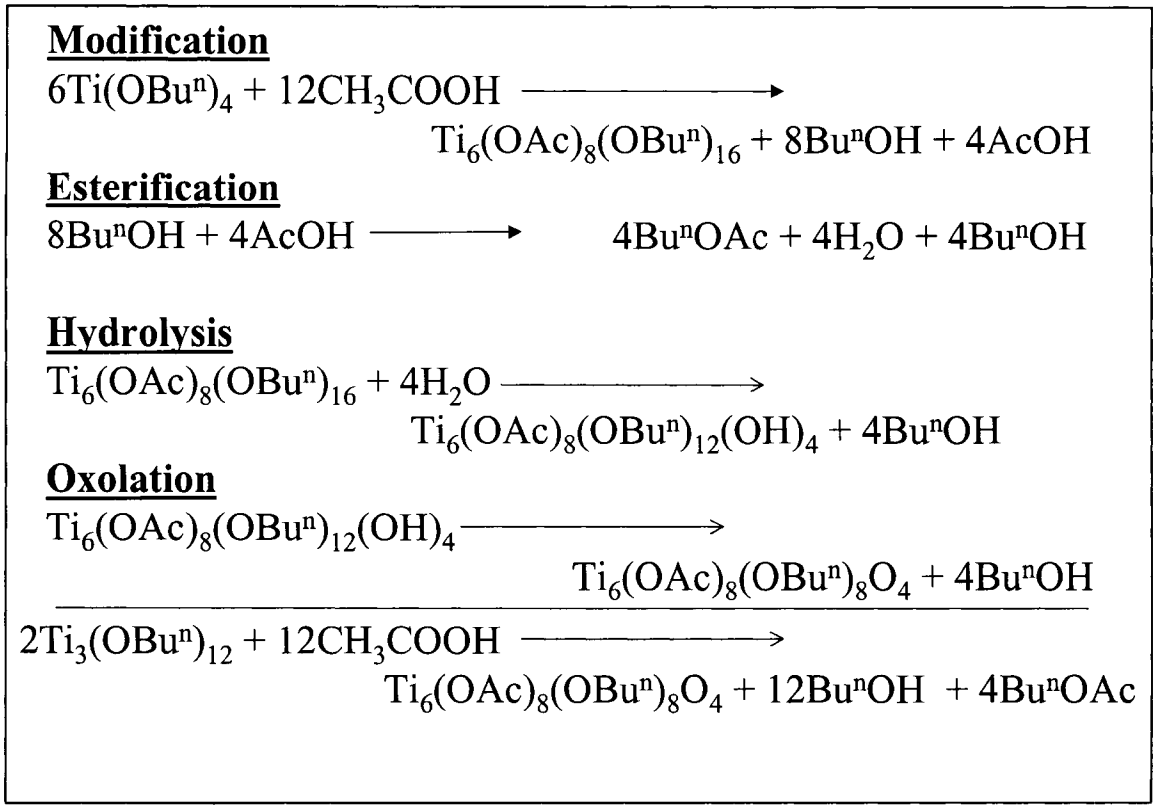

Figure 1.6. Solution chemistry for the chelate process using acetic acid as a modifier and solvent. Reaction is the esterification of metal alkoxides.

exchange promotes the formation of alcohol that is used in the esterification process to form esters and water. The next step is hydrolysis that is promoted by H_2O generated during esterification, and is followed by oxolation-the formation of oxo bridges between two metals. This reaction is also known as aging, and can affect the final microstructure of the perovskites. It was found that small uniform grain growth was formed with fresh solutions, whereas aged solutions had large uniform grain sizes. Based on this study, only fresh sols synthesized from this method and the Pechini method were used to coat templates.

The Pechini Method.[14,45] The chelating agent used in the Pechini method is citric acid, which has three carboxylic groups and one hydroxyl group available for reactivity. Nitrate and citric acid solutions are mixed with 2-methoxyethanol, and is heated around 80 °C to dissolve the citric acid. Temperatures of ~150-250 °C and acid catalyst (HNO_3) cause the condensation of water between ethylene glycol, the citric aid, and the chelated citric acid to form M-O-M bonding. It was observed that final powder morphology could be affected by changes in mixing process, water:ethylene:gylco:citric ratio, and heating/calcination profiles. Citric acid has been found to influence the density and crystallite/morphology of the final sintered powders. The 60:40 citric acid to alcohol was shown synthesized the most "puffed" resin that can be obtained. The puffed resin allows for the synthesis of crystallite with a narrow particle size and particle sizes of around 0.1 μm.

Scope of Dissertation. This research was aimed towards understanding the effects of grain size, crystallite size, and aspect ratio on the structure-property relationships for the perovskite materials. A second goal was to determine the critical

size where the physical properties of the nanocrystalline perovskites no longer behaved like the bulk material. Perovskite nanotubes and nanorods were used as experimental models to study systematically the aspect ratio and grain size on the electronic properties.

Traditionally, electronic size effects were evaluated using powder synthesis or thin film morphologies, which has limited control over grain size. [6,36,46,47] The research presented here was based on hypothesis that template synthesis would control grain/crystallite growth behavior and possibly aid in the preferred orientation of the crystal system down the axis or length of a nanowire. Templates synthesis was preferred for this research because the templates offer the advantage of controlling the physical dimensions of the material being synthesized. Therefore, templates could be applied to aid in a systematic investigation on size. Here, the previously reported techniques for the synthesis of metal oxide nanotubes were applied to the synthesis of the perovskites.[48] Thus far, we have synthesized and characterized the following nanotubes and nanofibers: $BaTiO_3$, $SrTiO_3$, $PbTiO_3$, $PbZrO_3$, the solid solution $Pb(Zr_xTi_{1-x})O_3$ (PZT), and $NdNiO_3$.

In Chapter 2, the development of the synthetic methods and characterization techniques required to fabricate one-dimensional materials used for the investigation on size effects is described.

Chapter 3 reports on the application of sol-gel template synthesis to the investigation of size-induced ferroelectric lead titanate ($PbTiO_3$) and antiferroelectric lead zirconate ($PbZrO_3$) phase transitions in nanotubes and nanofibers. Scanning and transmission electron microscopy indicate that the two observed morphologies depended upon the selection of two different templates employed and selection of a 0.8 M chelate sol-gel, made from titanium (IV) tetrabutoxide and lead (II) trihydrate acetate.

Nanotubes were formed within 200 nm pore Whatman Anodisc aluminum oxide membranes and nanofibers were prepared using 50, 100, and 200 nm Whatman Track-Etched polycarbonate membranes. Transmission electron microscopy images revealed that the tubes comprised grains of ≤ 20 nm and the fibers comprised individual grains ≤ 200 nm in width when a 200 nm pore size template is used. An examination of how the grain/crystallite size and aspect ratio of one dimensional morphologies affect the ferroelectric phase transition was monitored through the comparison of bulk powders and the nanostructured materials using electron diffraction, X-ray diffraction, Raman spectroscopy, and differential scanning calorimetry.

Chapter 4 describes a second investigation where the morphology of the $BaTiO_3$ and $SrTiO_3$ nanostructures is varied through sol-gel concentration, template, and heating conditions. For the first time $SrTiO_3$ nanotubes formed from the polycarbonate templates have been demonstrated. Studies concluded that grain size influenced observed fiber and tube morphology. Both nanostructures and bulk materials were also examined for symmetry and electronic properties. $BaTiO_3$ was found to be ferroelectric and $SrTiO_3$ was found paraelectric. Size effects on these two perovskites are presented. The examination of size effects on the optical properties showed that the nanocrystalline materials did not exhibit and significant deviations from the bulk materials.

Chapter 5 reports the synthesis and characterization of the first neodymium nickelate ($NdNiO_3$) nanofibers produced through sol-gel template synthesis. The Pechini method was used to prepare the sol for the fibers. Whatman track-etched polycarbonate membranes (200 nm and 100 nm pore size), which served as the template, were coated with the sol and allowed to air-dry. The templates were sintered at 50 °C/h to 800 °C in

air. The 100 nm templates were heated for 40 h and the 200 nm fibers were heated for 120 h. The fibers were cooled to room temperature at 30 °C/h. Scanning electron microscopy demonstrated that the structures formed are ~6 μm long fibers with diameters approximately the same size as the template used. Transmission electron microscopy showed that the 100 nm fibers have a string of grains morphology with grain size diameters of 90-100 nm. X-ray diffraction patterns for the two samples were indexed to the rhombohedral phase of $NdNiO_3$. An average crystallite size of 18 nm and 14 nm were calculated for 200 nm fibers sintered for a 120 h and 100 nm fibers sintered for 40 h, respectively.

Finally, Chapter 6 reports on the application of the template synthetic method towards the formation of WO_3 and fluorocarbon nanofibers. Preliminary data for proposed future research is presented.

Overall, the research reported demonstrates that template synthesis can control size and morphology. Crystalline symmetry and crystallite size were examined. Based on the crystallite size range and aspect ratio of $PbTiO_3$ fibers or tubes formed within the templates used for this research, it was shown that the two variables did not contribute to significant deviations in ferroelectric phase transition temperature, T_c,, when compared to the bulk powders. In general, perovksites synthesized through the templates used in this research did not show significant deviations in their properties from the bulk control powders except in crystallite sizes formed.

References

(1) Tolles, W. M.; Rath, B. B., *Curr. Sci.* **2003,** 85, 174-1759.

(2) West, J. L.; Halas, N. J., *Annu. Rev. Biomed. Eng.* **2003,** 5, 285-292.

(3) Jortner, J.; Rao, C. N. R., *Pure Appl. Chem.* **2002,** 74, 1491-1506.

(4) Trindade, T.; O'Brien, P.; Pickett, N. L., *Chem. Mater.* **2001,** 13, 3843-3858.

(5) Edelstein, A. S.; Cammarata, A. S., *Nanomaterials*. 1st ed.; Institute of Physics Publishing: Bristol and Philadelphia, **1996**.

(6) Akdogan, E. K.; Leonard, M. R.; Safari, A., Size Effects in Ferroelectric Ceramics. In *Handbook of Low and High Dielectric Constant Materials and Their Applications*, ed.; Academic Press: **1999**;pp 61-112.

(7) Xia, Y.; Yang, P.; Sun, Y.; Wu, Y.; Mayers, B.; Gates, B.; Yin, Y.; Kim, F.; Yan, H., *Adv. Mater.* **2003,** 15, 353-388.

(8) *Webseters Unabridged Dictionary*. 2nd ed.; Random House: New York, p 555.

(9) Dai, Z. R.; Pan, W. Z.; Wang, Z. L., *Adv. Funct. Mater.* **2003,** 13, 9-20.

(10) Patzke, G.; Krumeich, F.; Nesper, R., *Angew. Chem., Int. Ed. Engl.* **2003,** 41, 2446-2461.

(11) Rao, C. N. R.; Deepak, F. L.; Gundiah, G.; Govindaraj, A., *Prog. Solid State Chem.* **2003,** 31, 5-147.

(12) Rao, C. N. R.; Nath, M., *Dalton Trans.* **2003,** 1, 1-24.

(13) Pena, M. A.; Fierro, J. L. G., *Chem. Rev.* **2001,** 101, 1981-2017.

(14) Schwartz, R. W., *Chem. Mater.* **1997,** 9, 2325-2340.

(15) Shriver, D. F.; Atkins, P. W., *Inorganic Chemistry*. 3 rd ed.; W. H. Freeman and Company: New York, **1999**; p 629-634.

(16) Jona, F.; Shirane, G., *Ferroelectric Crystals*. ed.; MacMillan: New York, **1962**.

(17) Buchanan, R. C.; Park, T., *Materials Crystal Chemistry*. 1st ed.; Marcel Dekker, INC.: New York, **1997**,292-296, 337-342.

(18) Thomas, N. W., *Br. Ceram. Proc.* **1994,** 52, 1-12.

(19) Smith, W., *Principles of Materials Science and Engineering*. 3rd ed.; McGraw-Hill: New York, **1996**.

(20) O'Brien, S.; Brus, L.; Murray, C. B., *J. Am. Chem. Soc.* **2001,** 123, 12085-12086.

(21) Liu, C.; Zho, B.; Rondione, A. J.; Zhang, Z. J., *J. Am. Chem. Soc.* **2001,** 123, 4344-4345.

(22) Limmer, S. J.; Cao, G., *Adv. Mater.* **2003,** 15, 427-431.

(23) Limmer, S. J.; Hubler, T. L.; Cao, G., *J. Sol-Gel Sci. Tech.* **2003,** 26, 577-581.

(24) Limmer, S. J.; Seraji, S.; Forbess, M. J.; Wu, Y.; Chou, T. P.; Nguyen, C.; Cao, G., *Adv. Mater.* **2001,** 13, 1269-1272.

(25) Limmer, S. J.; Seraji, S.; Wu, Y.; Chou, T. P.; Nguyen, C.; Cao, G., *Adv. Funct. Mater.* **2002,** 12, 59-64.

(26) Urban, J.; Yun, W. S.; Gu, Q.; Park, H., *J. Am. Chem. Soc.* **2002,** 124, 1186-1187.

(27) Yun, W. S.; Urban, J. J.; Gu, Q.; Park, H., *Nano Letters* **2002,** 2, 447-450.

(28) Schaak, R. E.; Mallouk, T., *Chem. Mater.* **2000,** 12, 3427-3434.

(29) Hernandez, B. A.; Chang, K.-S.; Fisher, E. R.; Dorhout, P. K., *Chem. Mater.* **2002,** 14, 480-482.

(30) Chang, K.-S.; Hernandez, B. A.; Fisher, E. R.; Dorhout, P. K., *J. Korean Chem. Soc.* **2002,** 46, 242-251.

(31) Mao, Y.; Banerjee, S.; Wong, S. S., *Chem. Commun.* **2003**, 408-409.

(32) Wang, Y. G.; Zhong, W. L.; Zhang, P. L., *Soild State Commun.* **1994,** 90, 329-332.

(33) Akdogan, E. K.; Safri, A., *Jpn. J. Appl. Phys.* **2002,** 41, 7170-7175.

(34) Lakshmi, B. B. Separtions Using Biological Carrier Immobilized in Porous Polymeric and Sol-Gel Templated Synthesized Nanotubular Membranes. Dissertation, Colorado State University, Fort Collins, **1998**.

(35) Pfaff, G., *J. Mater. Chem.* **1992,** 2, 591-594.

(36) Escote, M. T.; da Silva, A. M. L.; Matos, J. R.; Jardim, R. F., *J. Solid State. Chem.* **2000,** 151, 298-307.

(37) Sharma, H. B.; Mansingh, A., *J. Mater. Sci.* **1998,** 33, 4455-4459.

(38) Brinker, C. J.; Scherer, G. W., *Sol-Gel Science: The Physics and Chemistry of Sol-Gel Processing*. ed.; Academic Presss, INC Hartcourt Brace Jovanovich: San Diego, **1990**.

(39) Boyle, T. J.; Dimos, D.; Schwartz, R. W.; Alam, T. M.; Sinclair, M. B.; Buchheit, C. D., *J. Mater. Res.* **1997,** 12, 1022-1030.

(40) Moreno, J.; Dominguez, J. M.; Montoya, A.; Vincente, L.; Viveros, T., *J. Mater. Res.* **1995,** 5, 509-512.

(41) Kamalasanan, M. N.; Chandra, S.; Joshi, P. C.; Mansingh, A., *Appl. Phys. Lett.* **1991,** 59, 3547-3549.

(42) Cheung, M. C.; Chan, H. L. W.; Choy, C. L., *J. Mater. Sci.* **2001,** 36, 381-387.

(43) Livage, J.; Henry, M.; Sanchez, C., *Prog. Solid State Chem.* **1988,** 18, 259-341.

(44) Doeuff, S.; Dromzee, Y.; Taulelle, F.; Sanchez, C., *Inorg. Chem* **1989,** 28, 4439-4445.

(45) Lessing, P. A., *Ceram. Bull.* **1989,** 68, 1002-1007.

(46) Kwun , S.-I.; K., S. T., *Ferrolectrics* **1997,** 197, 125-130.

(47) Lanciotti, F.; Pizani, P. S.; Campos, C. E. M.; Leite, E. R.; Santos, L. P. S.; Carreno, N. L. V.; Longo, E., *Appl. Phys. A* **2002,** 74, 787-789.

(48) Lakshmi, B. B.; Dorhout, P. K.; Martin, C. R., *Chem. Mater.* **1997,** 9, 857-862.

CHAPTER 2

Template Synthesis Techniques and Methodology for One-Dimensional Perovskite Materials

I. Introduction

This chapter reports the synthesis, characterization, and methodology development employed to produce high-aspect-ratio perovskite materials. Section II describes the general experimental methods that were employed to synthesize the sol-gel precursors that lead to the metal oxide solids and the crystallization parameters for the production of the $PbTiO_3$, $PbZrO_3$, $BaTiO_3$, and $NdNiO_3$ nanotubes and fibers presented in the subsequent chapters. Also included in this section is a description of the sol-gel precursor synthesis of solid WO_3 reported in Chapter 6. (Note: plasma deposition parameters used to form fluorcarbon nanofibers are described in Chapter 6). Section III describes sample preparation for the characterization techniques used to determine morphology, crystal symmetry, and physical properties associated with the materials listed above. Finally, Section IV outlines the sol-gel template synthetic technique and discusses the optimization studies used to produce nanofibers and nanotubes.

II. Experimental Methods

Materials: Titanium (IV) tetrabutoxide, $Ti[O(CH_2)_3CH_3]_4$, zirconium (IV) tetrabutoxide (80% by weight in butanol), $Zr[O(CH_2)_3CH_3]_4$, lead (II) trihydrate acetate, $Pb(CH_3CO_2)_2{\cdot}3H_2O$, tungsten (VI) chloride, WCl_6, and 2,4-pentadione, were purchased from Aldrich and were used as received. Strontium acetate, $Sr(CH_3CO_2)_2$, was purchased from Pfaltz & Bauer. Neodymium (III) nitrate hexahydrate, $Nd(NO_3)_3{\cdot}6H_2O$ (99.9%), and nickel (II) nitrate hexahydrate, $Ni(NO_3)_2{\cdot}6H_20$ (99.9985%), were purchased from AESAR. Glacial acetic acid (CH_3CO_2H), 1-butanol ($CH_3(CH_2)_3OH$), barium acetate ($Ba(CH_3CO_2)_2$), anhydrous citric acid ($C_6H_8O_7$), 2-methoxyethanol ($CH_3OCH_2CH_2OH$),

Whatman® anodisc aluminum oxide membranes (200 nm pore size, 50 μm thick, 25 mm diameter), Whatman® track-etched polycarbonate membranes with pore sizes of 200, 100, and 50 nm (10 μm thick, 25 mm diameter), and CoorsTek combustion boats were purchased from Fisher. To prevent or minimize the formation of surface film on the templates during the coating process, one side was masked with 3M cellulose tape prior to coating. Sodium hydroxide (NaOH) pellets and nitric acid (HNO_3) were obtained from Mallinckrodt. Purified water was obtained by passing house-distilled water through a Milli-Q (Millipore) water purification system. Sandpaper (1500 grit, 3M) and quick-dry epoxy from Cole-Parmer Instrument Co. were used to prepare samples for electron microscopy studies. Formvar-coated 200 mesh copper grids were purchased from Ted Pella Inc., and double-sided carbon disks were purchased from Electron Microscopy Sciences.

Synthetic Methods: The following sol-gel precursors were used to coat anodized aluminum oxide (AAO) and track-etched polycarbonate (PC) templates.

0.8 M $PbTiO_3$, I, Chelate Sol-Gel. A 5% excess of lead salt was added to the solution to compensate for lead volatility. $Pb(CH_3CO_2)_2{\cdot}3H_2O$, 4.779 g (12.59 mmol), were dissolved in 6 mL of acetic acid, refluxed at 60 °C for ~ 20 minutes, and then allowed to cool to room temperature. A second solution of $Ti[O(CH_2)_3CH_3]_4$, 4.083 g (11.99 mmol), and 2.5 mL 1-butanol was prepared and added to the room temperature lead acetate solution yielding a clear sol. The solution was stirred for 5 minutes before it was applied to the template.

0.8 M $PbZrO_3$, II, Chelate Sol-Gel. A 5% excess of lead salt was added to the solution to compensate for lead volatility. $Pb(CH_3CO_2)_2{\cdot}3H_2O$, 3.186 g (8.399 mmol),

were dissolved in 5 mL of acetic acid, refluxed at 60 °C for ~ 20 minutes, and then allowed to cool to room temperature. Next, 3.836 g (9.998 mmol) of $Zr[O(CH_2)_3CH_3]_4$, 80% by weight in 1-butanol, was added to the room temperature lead acetate solution yielding a clear sol. The solution was stirred for 5 minutes before it was applied to the template.

0.8 M $BaTiO_3$, III, Chelate Sol-Gel. $Ba(CH_3CO_2)_2$, 2.043 g (7.998 mmol), were dissolved in 7 mL of acetic acid, refluxed at 60 °C for ~ 20 minutes, and then allowed to cool to room temperature. A second solution of $Ti[O(CH_2)_3CH_3]_4$, 2.723 g (8.000 mmol), and 1.0 mL ethanol was prepared and added to the room temperature barium acetate solution yielding a clear sol. The solution was stirred for 5 minutes before it was applied to the template.

0.5 M $SrTiO_3$, IV,Chelate Sol-Gel. $Sr(CH_3CO_2)_2$, 1.029g (5.002 mmol), were dissolved in 5 mL of acetic acid, refluxed at 60 °C for ~ 20 minutes, and then allowed to cool to room temperature. A second solution of $Ti[O(CH_2)_3CH_3]_4$, 1.702 g (5.001 mmol), and 5 mL of 1-butanol was prepared and added to the room temperature strontium acetate solution leading to the formation of a clear sol. The solution was stirred for 5 minutes before it was applied to the template.

$NdNiO_3$, V, Pechini Sol-Gel. The Pechini method, reported by Fernandes et al., was used to prepare **V**.[1,2] The sol was prepared from a 1:1:2.5 molar ratio of Nd:Ni:citric acid and a 60:40 ratio of citric acid to 2-methoxyethanol. $Nd(NO_3)_3{\cdot}6H_2O$, 4.383 g, and $Ni(NO_3)_2{\cdot}6H_2O$, 2.908 g were dissolved in 6.68 mL of purified Milli-Q (Millipore) water and formed a clear green solution. Citric acid, 4.803g, were added to the metal nitrate solution and stirred for 15 minutes before dissolving. Next, 3.32 mL of 2-

methoxyethanol were added to the metal citrate solution. A drop of nitric acid was used to maintain a pH of 2 and catalyze gel formation.[3] The solution was heated to 90 °C to remove excess HNO_3. After 20 minutes of heating, gelation was initiated and the solution became viscous. This solution was added dropwise onto Whatman® track-etched polycarbonate (PC) template membranes with 200 nm and 100 nm pore size (10 μm thick, 25 mm diameter).

WO_3, VI, Sol-Gel. The colloidal sol-gel synthesis, reported by Nishide et al., was used to prepare the sol-gel precursor for VI.[4] N_2 gas was bubbled through 10 mL of ethanol to remove air. 1.000 g of WCl_6 (2.522 mmol) were added to the ethanol with continued N_2 bubbling. The solution was stirred until WCl_6 was fully dissolved. The resulting solution changed colors from yellow to green-blue. 2 mL (19.41 mmol) of 2,4-pentadione chelating agent were added to the tungsten solution, and 0.05 mL of H_2O was added to initiate hydrolysis. The resulting solution turned dark blue to form a colloidal sol. The solution was used immediately to coat templates.

I-IV perovskite nanotubes, fibers, and bulk powders were prepared from chelate sol-gels with a total volume of 10 mL. Because of the esterfication pathways of the chelate sol and its effect on microstructure, only fresh sols were used to fabricate tubes and fibers.[5,6] **V** was prepared with the Pechini method and **VI** was prepared using a colloidal sol-gel route. All sol-gel procedures were performed outside the glove box.

Coating Process. One side of the template was covered with 3M transparent cellulose tape prior to coating. After the sols were prepared, the unmasked side of the template was coated by the drop-wise addition of the sol. Through capillary action, the sol penetrated the nano-channels of the templates. Excess sol was removed from the

template with a Kim-wipe and the template was allowed to dry in air for 30 minutes or overnight. Prior to the calcination process, templates were reinforced by inserting them between Al_2O_3 plates (dimensions of a microscope slide) and placed upright in a combustion boat. This step was used to prevent the AAO templates from curling while being calcined, and aids in the polishing process to remove surface film afterwards. PC templates were also reinforeced to prevent the formation of undulated thin films, See Section VI, page 49.

Crystallization Process. Samples were calcined in air at a rate of 50 °C/hour to the desired temperature and were kept at this temperature for 6 hours or longer before being slowly cooled to room temperature at a rate of 30 °C/hour. The remaining unused sol was allowed to gel and was calcined using the same heating procedures to produce our "bulk" powders as the control samples.

III. Characterization Methods:

Scanning Electron Microscopy. The microscopic morphologies and elemental compositions of the structures were investigated using a JEOL JSM6500F field emission scanning electron microscope (FESEM) coupled with X-ray energy dispersive spectroscopy (EDS) from NORAN Vantage System. Pristine templates were coated with 5 nm of Au using an Anatech Hummer VII sputter coater prior to being attached to SEM stubs with double-sided carbon tape. Additionally, the control sample powders, as well as the nanostructures of interest were all examined without the Au coating. Micrographs of the powders and fibers were obtained by spreading the calcined samples directly onto carbon tape. Images of the tubes were obtained by adhering the calcined AAO template

containing our samples to a piece of paper towel embedded with epoxy. After the epoxy hardened, any perovskite surface film was removed by polishing. Then the AAO template was removed from the tubes by immersing the sample in 6M NaOH for 6 hours. The sample was rinsed several times with Millipore water until the filtrate pH reached 7. After drying overnight in air, the samples were attached to SEM stubs using double-sided carbon tape.

Transmission Electron Microscopy. The microstructures of the nanostructured materials were determined by transmission electron microscopy (TEM). Tubes were prepared for TEM in a manner similar to that described above without the application of an epoxy backing to the AAO template. After dissolution of the AAO templates in 6M NaOH, the supernate was removed by decantion after centrifugation. The remaining solid residue was rinsed several times with water and centrifuged again. When the washings reached a neutral pH, the sample was sonicated to disperse the material in solution. A pipette was used to transfer an aliquot of sample water onto a Formvar-coated 200 mesh copper grid and allowed to dry overnight on the grid. A small sample of the calcined nanofibers were added to water and sonicated before being dispersed onto the TEM grids. Images and selected area electron diffraction (SAD) patterns were taken on a JEOL JEM 2000 EXII microscope. The accelerating voltage was 100 kV and the camera length raged from 100 cm to 80 cm depending on the sample. Typically, diffraction rings for nanotubes were best observed at 100 cm and 80 cm for fibers.

SAD patterns were evaluated by the method of comparative *d*-spacings resulting in an error of 6%.[7,8] Measurement of the radii of the concentric ring powder patterns was

performed with a meteric ruler where the error associated with the measurement was ± 0.5 mm.

Powder X-Ray Diffraction. The average Bravais lattice crystal symmetry and the cell parameters for the bulk and nanoscale material were found using powder X-ray diffraction (PXRD) patterns collected on one of two instruments. Initial surveys of the specimens were collected on a Philips 1203 powder diffractometer with Cu K_α radiation (1.5406 Å) and a scintillation counter detector. Crystallite size analysis was performed on a Scintag X2 diffractometer with Cu K_α radiation (1.5406 Å) and a Peltier detector. Samples were scanned at a rate of 0.02°/2 sec in the 2θ range of 5-60° for **I-IV** and in the 20-80° range for **V** and **VI**. Lattice parameters were calculated with the JADE software program.[9] Bulk powders were prepared by grinding the samples with an agate mortar and pestle and mounting them on to a glass holder. Nanotubes and fibers were mounted directly onto the glass holder without initial grinding.

The average crystallite sizes for the materials were determined from the full width at half maximum (FWHM) of the (111) reflection for the tetragonal phase of **I and II** and the (101) reflection for the cubic phase of **III-V** using the single line parameterized Warren-Averbach method.[10] Instrument broadening was corrected using a standard: NIST SRM 1976.

Raman Spectroscopy. The crystalline Bravais symmetry was evaluated by room temperature Raman scattering on a home-built optical bench using an Acton Research Spectra Pro-275 LN_2-cooled CCD detector (256x1024) and controller model 51130 with an Argon laser line at 514.5 nm. The system was calibrated with an Argon pencil-style calibration lamp from ORIEL Instruments and a sulfur standard. Raman spectra were

evaluated using the GRAMS/AI software system.[11] This instrument was used to evaluated size effects in **I and III.** A Nicolet Magna-IR Spectrometer with FT-Raman Module attachment using a Nd:YAG Laser (1064) was also used for samples **II** and **III**. Samples were prepared by placing a small amount of powder on to a microscope glass slide and covering with transparent 3M cellulose tape.

Differential Scanning Calorimetry. The ferroelectric-paraelectric phase transition temperatures of **I, III,** the antiferroelectric-paracelectric phase transition temperatures (T_c) of **II,** and enthalpy of phase transitions (ΔH) were monitored by differential scanning calorimetery (DSC). Samples (5-10 mg) were sealed in aluminum DSC pans by crimping them closed. Data were collected using a TA Instruments DSC 2929 Modulated DSC under N_2 flow at 10°C/min. in the temperature range of 28-600 °C. The metal-insulator transition temperature (T_{MI}) of **V** was monitored under N_2 flow at 10°C/min. in the temperature range of –140-0 °C.

UV-Visible Diffuse Reflectance Spectroscopy. Ultraviolet-visible (UV-vis) diffuse reflectance spectra of the **I-V** and **VI** samples were obtained using a Varian Cary 500 spectrophotometer with a Harrick-Scientific praying-mantis diffuse reflectance accessory. Teflon powder was used as a reference (100% reflectance). Adsorption data were calculated from the reflectance data using the Kubelka-Munk function[12]

$$\alpha/S = (1-R)^2/2 \qquad (2.1)$$

where R is the reflectance at a given wavelength, and α is the scattering coefficient. The optical band gap energy (Eg) value was extracted from the $(\alpha/S)^2$ versus energy plot. The Eg was taken as the point where the extrapolated linear portion of the plot intersected the energy axis at $(\alpha/S)^2 = 0$.

IV. Development and Optimization of Template Synthesis.

Commercially available anodized aluminum oxide (AAO) and polycarbonate track-etched membrane templates from Whatman® were used to fabricate nanofibers and nanotubes. SEM images, Figure 2.1, illustrate the pore density and size while the accompanying diagrams demonstrate the physical dimensions of the membrane templates. An initial investigation on sol-gel template synthesis began with reviewing the process developed from the work of Lakshmi et al. to synthesize TiO_2 nanotubes and nanofibers.[7] Figure 2.2 illustrates the general procedure used for the template synthesis performed by Lakshimi and in this research. AAO templates were dip-coated in sols for predetermined time periods, allowed to air dry for 30 minutes, and then calcined.

The processed templates were adhered to epoxy and the surface of the template was polished to any remove film deposited during the dip-coat procedure. The template was removed through dissolution in 6 M NaOH for ten minutes, rinsed until a neutral pH was achieved, and dried in air at room temperature. This general procedure was applied to the synthesis of the pervoskite nanostructures, but was later optimized. The subsequent chapters in this dissertation discuss the subtleties of the unique morphologies obtained from a series of experiments aimed towards the synthesis of well-defined one-dimensional materials. Below an overview of the methodology developed is presented.

V. Synopsis of Procedures Used for AAO Templates.

Dip-Coating Process. Early studies were conducted to evaluate AAO template removal in NaOH for dip-coated templates. Polished samples that were attached to epoxy were placed in NaOH for 10 minutes to 1 hour. SEM images, Figure 2.3, illustrate

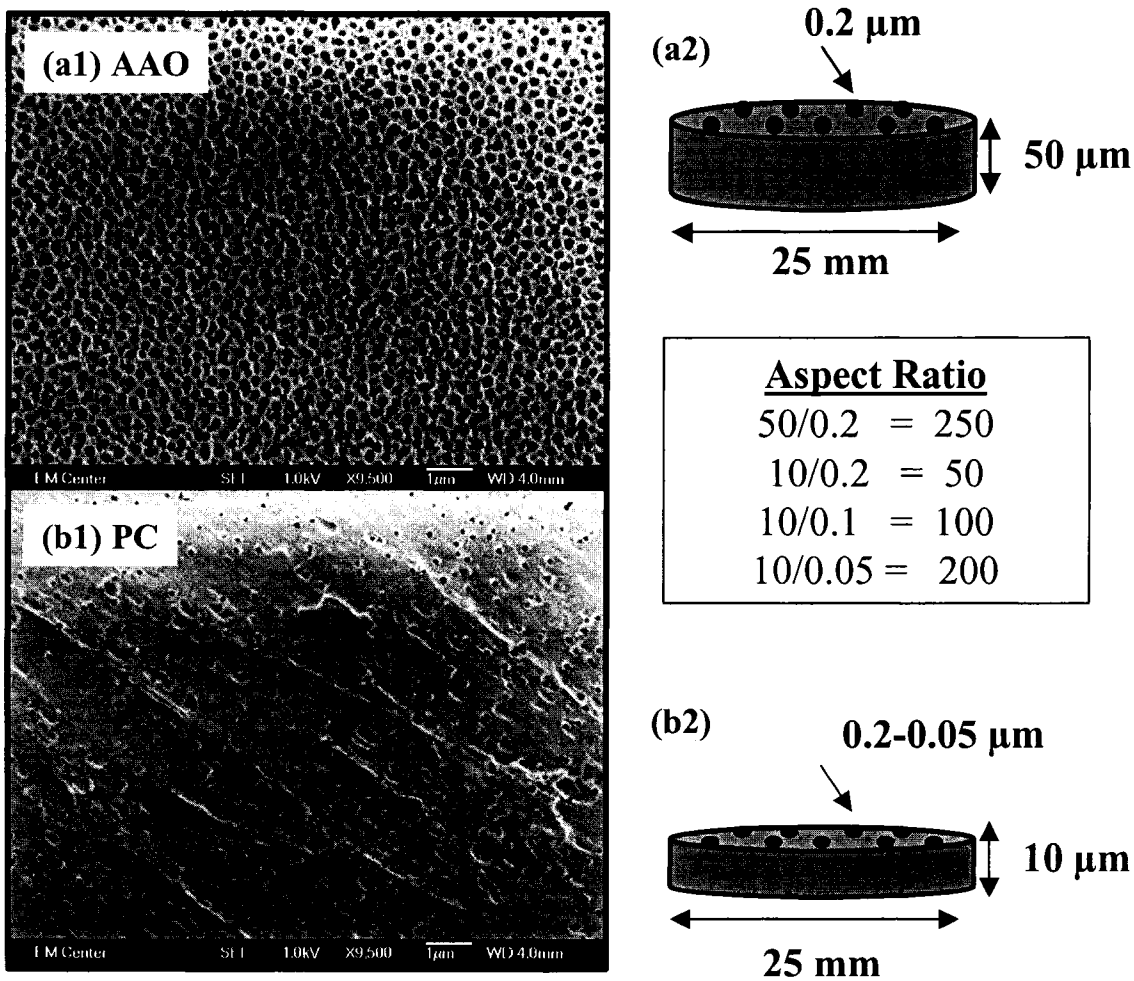

Figure 2.1. SEM images of an untreated Whatman® (a1) anodized aluminum oxide (AAO) and (b1) track-etched polycarbonate (PC) membranes (magnification at x9,500). Both templates shown have an average 200 nm pore channels. The dimensions and aspect ratios of the respective templates are shown in (a2) and (b2).

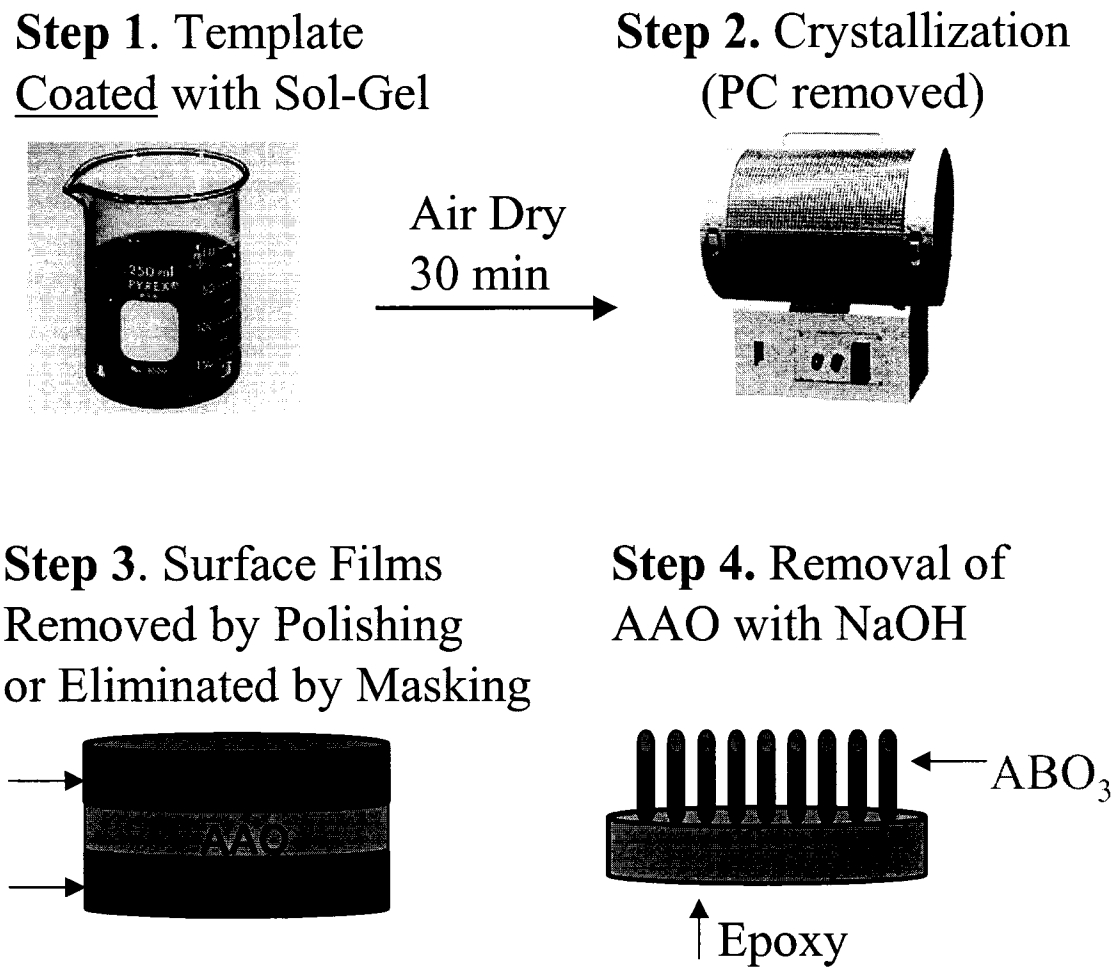

Scheme 2.1. General sol-gel template synthetic approach used for anodized aluminum oxide (AAO) and track-etched polycarbonate (PC) membrane templates.

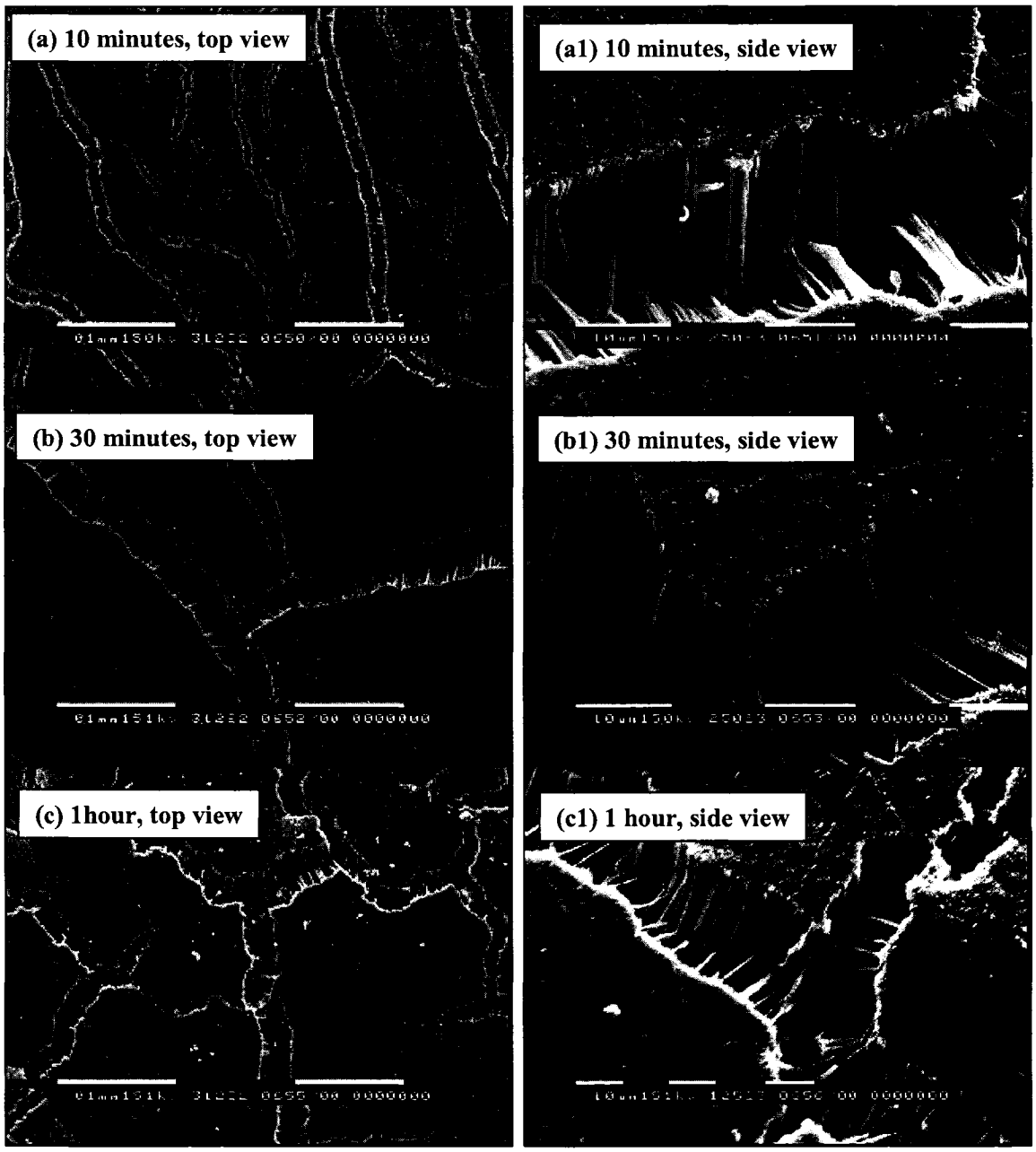

Figure 2.3. The effects of soak time in 6 M NaOH for removal of the AAO template and bundle formation. SEM images of the top and side views of TiO_2 nanotubes after the AAO template has been removed. As time increases, smaller bundles of nanotubes are formed. Bundles are held together by surface film.

the effect of soak time in 6 M NaOH on the removal of the AAO template. As time increased, the amount of AAO template removed increased. This is evident by the 40% increase in bundle formation for 1 hour in contrast to the 10 minutes employed by Lakshimi.[7] Based on this examination, samples were usually left overnight in NaOH to maximize the amount of template removed. Another experimental variable that inhibited the removal of the template was the calcination temperature. Calcination temperatures below 750 °C had no effect on the dissolution of empty and uncalcined templates. Temperatures above 750 °C, however, began to crystallize the amorphous AAO and dissolution of the template became difficult. In addition, the reasonably flat templates curled when calcined above 500 °C making the polishing process difficult. To minimize this problem, the templates were placed between Al_2O_3 slides (dimensions of a microscope slide) to keep the template flat for polishing.

Figure 2.4 highlights the SEM results for $BaTiO_3$ calcined at 650 °C and shows the entire dip-coating process incorporating template reinforcement by Al_2O_3 slides and overnight template removal. An evaluation of the surface films, Figure 2.4a, revealed that thin films of $BaTiO_3$ formed on both faces of the template (when not masked) which possessed many cracks. The surface film shown was not polished. The cracks may have resulted from cutting a piece of the epoxy-template sample for SEM analysis. The formation of interconnected bundles, Figure 2.4b, is significantly enhanced by longer soak times in base. Closer evaluation of the bundles end surfaces, Figure 2.4c, reveals that thick layers surface film often still remained on the structure even after some polishing. This film masked the identity of the structural morphology determined by SEM. However, TEM analysis clarified that the structures formed during the dip-coating

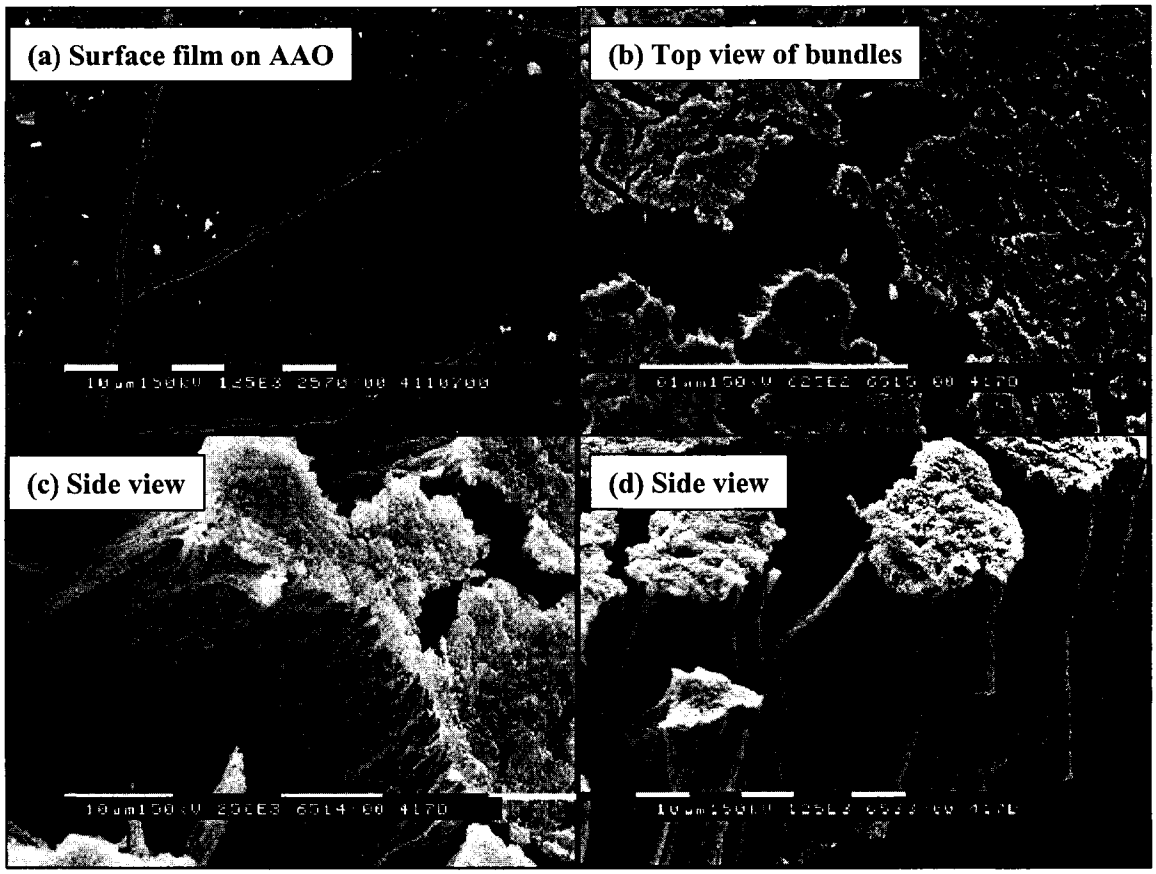

Figure 2.4. The effects of using an unmasked template on the identification of tube morphology with SEM. Images illustrate process outcome for templates dip-coated with sol, calcined, surface film removed by polishing, and AAO template removed with 6M NaOH. (a) Surface film on AAO after coating and calcination. (b) Top view of bundle formation. (c) Tube tops covered with residual amounts of surface film hindering identification of tube openings. (d) Side view illustrating the ~50 μm tube length. Material shown is $BaTiO_3$.

process were ~200 nm outer diameter tubes. The length of the tubes were almost always ~50 μm, as seen in Figure 2.4d. Fiber formation was tested by increasing the time of dip-coating in the sol. Varying the concentration of the sol and the time the template was in contact with the sol only yielded tube morphology. Further details specific to the ABO_3 materials will be discussed in Chapters 3 and 4. Finally, the surface film found on the ends of the nanotubes raised a general concern about the measurement of physical properties associated with the grain/crystallite size effects found in perovskites. A second optimization to the template synthetic technique was needed to remove or eliminate the surface film, which was found to have a larger grain/crystallite size than the nanotubes.

The polishing methods reported by Lakshmi for metal oxides such as TiO_2 that had been calcined below 650 °C were not as successful for the perovskite materials. The difficulty in removing the surface films was related to the increased hardness of the perovskite materials when grain size becomes smaller.[13] Different grits of sand paper ranging from 400-2000 and a Dremmel® sander were evaluated on both calcined and uncalcined surfaces. Experiments revealed that AAO templates that had been adhered to an epoxy surface were more resilient to the polishing techniques than were free-standing templates. The brittle AAO template easily fractured during the polishing procedure and a minimal amount of surface film could be removed. A study conducted on polishing the surface film before calcination occurred found that uncalcined AAO templates were slightly more pliable than calcined templates. The polished surface of an uncalcined template, Figure 2.5, illustrates the combined effects of 2000 and 1500 grit sand paper

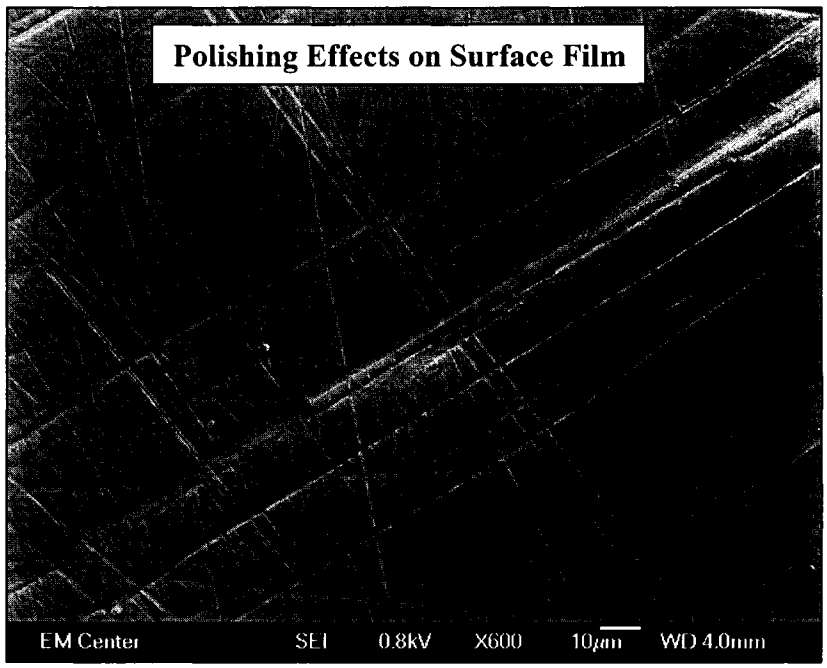

Figure 2.5. SEM image of a surface film. Sample was polished with 2000 and 1500 grit sand paper along with a dremmel sander. $BaTiO_3$ sample shown in image was not calcined.

and 84922 Dremel® grinding stone. The grinding stone produced the deepest ravines seen in the SEM image. The Sample shown was polished briefly by all three methods.

Drop-Wise Coating Process Using Masked AAO. To reduce and eliminate the surface film produced, two processes were tested that minimized the amount of sol in contact with the template were used. In the first method, one side of the template was masked or covered with 3M cellulose tape, in the second method, the drop-wise addition of sol to the template was tested. Experiments that explored the viability of masking the template with cellulose tape included determining which composition of tape best adhered to the surface. Cellulose tape that was opaque did not adhere as well as transparent cellulose tape. Masked templates were dipcoated. SEM analysis on these sample showed that the transparent tape adhered to the surface better than opaque tape leading to large areas that were free of surface film on the masked side. However, no significant reduction in surface film was observed with the dip-coat process.

The method of drop-wise addition of the sol was used in conjunction with the masked template method described above. SEM images of the resulting process, Figure 2.6, illustrate the effectiveness of the method. The unmasked side of the template was coated with a few drops of sol delivered by pipette. One drop was spread over the template with the pipet tip and the sol entered the template through capillary action, changing the appearance of the template from white to transparent as the sol enters the pore channels. Additional drops were added if needed. After the template was coated, excess sol was wiped off the surface and allowed to dry. While being reinforced with the tape, the coated side was polished with the Dremmel®. Samples were calcined at 650 °C while being reinforced by the Al_2O_3 slides to prevent template curl. SEM analysis of the

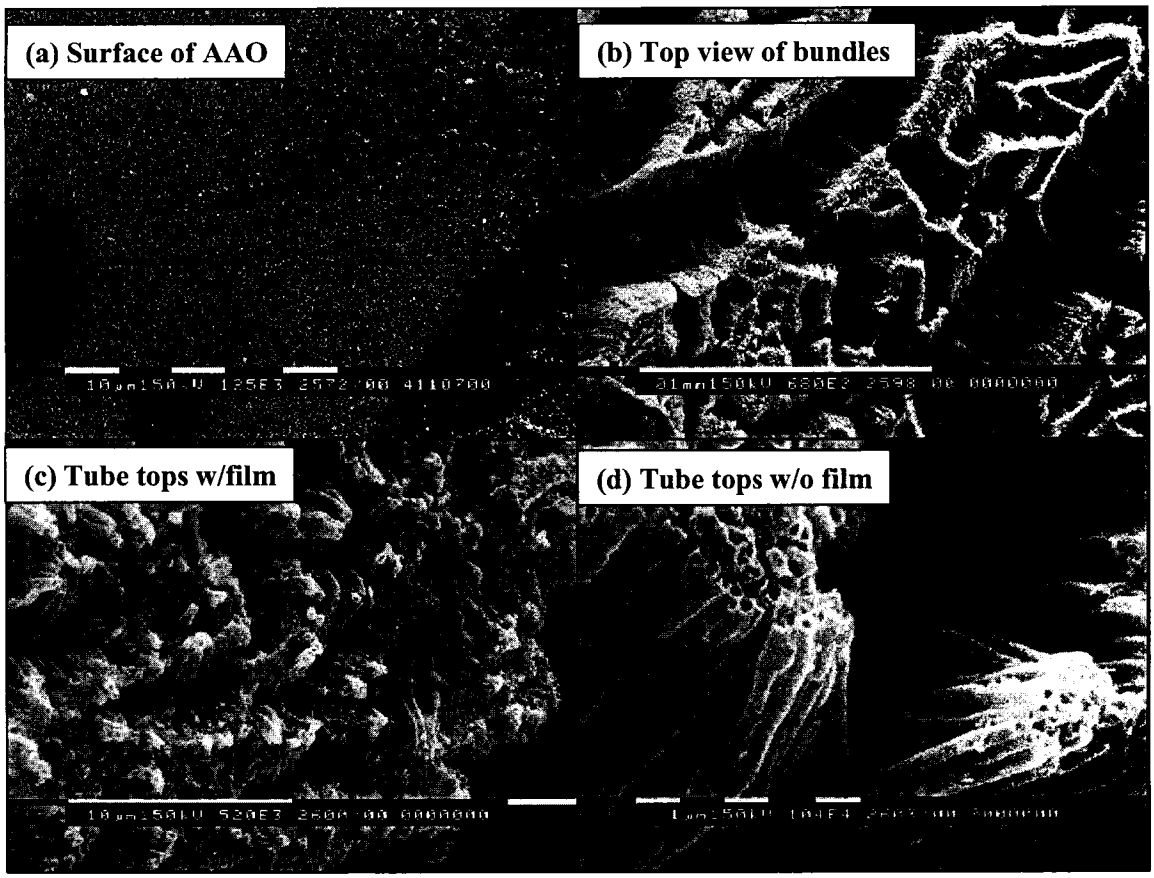

Figure 2.6. The effects of using a masked template for the identification of tube morphology. SEM images illustrating process outcome for templates masked prior to drop-wise coating with sol, calcined and AAO removed with 6M NaOH. (a) Surface of the masked side after coating and calcination. (b) Top view of bundle formation in an area without surface film. (c) Tube tops covered with residual amounts of surface film. (d) Surface film free area of tubes with an outer diameter of 200 nm. Nanotubes shown are $BaTiO_3$.

unmasked surface, Figure 2.6a, revealed small amounts of surface film (dark area) on the template. The surface film on the unmasked side was a result of excess sol that had penetrated through the channel coating areas where the mask did not adhere properly. The morphology of the bundles, Figure 2.6b, is different from bundles shown in Figure 2.4b. Magnified regions of the structures, Figures 2.6c and 2.6d, reveal tube morphology. Residual amounts of surface film are seen in Figure 2.6c, and an area free of surface film is shown Figure 2.6d.

Samples prepared from the drop-wise coating of masked templates were used in the investigation of size effects with 1-D perovskites. Characterizations of the size effects were performed on nanotubes removed from the template using the TEM sample preparation techniques. SEM images of sonicated $PbTiO_3$ nanotubes prepared by this technique are shown in Figure 2.7. Several hours of sample washings with H_2O were required to affect the base solution since base was often drawn inside the nanotubes by capillary action. During TEM analysis, clear evidence for bundle formation was observed, Figure 2.7b. The bundles were often held together by the incomplete removal of perovskite coated surfaces and imperfection in the template itself. The AAO template has a branched channel structure that forms during preparation. The sol can enter the branched channels and defects within the channels, allowing formation of interconnected nanostructures that cannot be removed though base wash or sonication. During TEM analysis, thin layers of the perovskite-coated AAO honeycomb structure was sometimes observed. Analysis of the samples revealed that any remaining template did not interfer with characterization techniques described in Chapter 3.

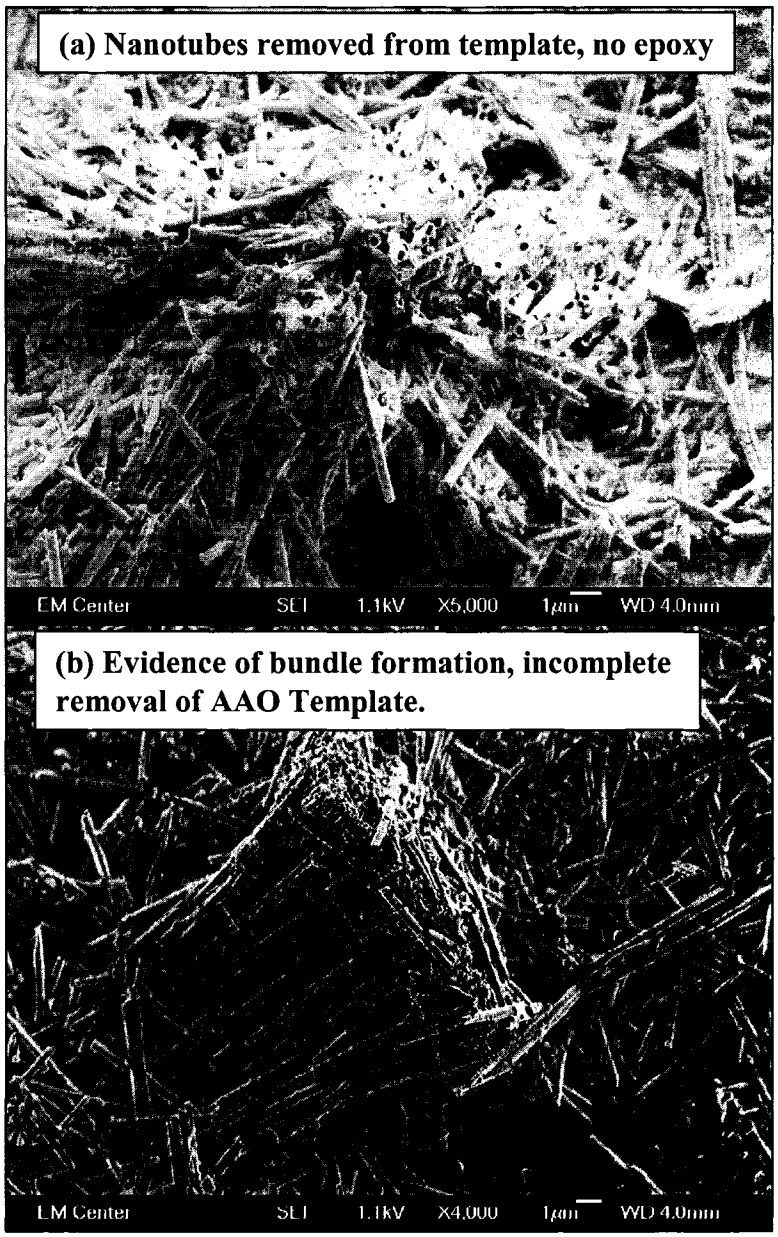

Figure 2.7. SEM images of $PbTiO_3$ tubes removed from the AAO template with 6 M NaOH. Samples shown have been sonicated. (a) Free nanotubes without surface film and AAO template. (b) Evidence of bundle formation resulting from the incomplete removal of AAO coated with surface film

VI. Synopsis of Procedures Used for PC Templates

Initial investigations using PC templates began with reviewing the work of sol-gel template synthesis using the electrodeposition methods proposed by Limmer et al.[14] Various metal oxide nanorods, including $BaTiO_3$ and PZT ($Pb(Ti,Zr)O_3$) were produced with this method. PC templates were filled with sol and dried. The samples were then placed directly into a furnace at the desired temperature and heated for 15 minutes. Limmer's methodology was optimized for sol-gel template synthesis using capillary action as a means to fill the nanochannels in the PC template. The next section describes the developmental process taken. SEM images, Figure 2.8, illustrate the results of this study.

Dip-Coating Process. PC templates were dip-coated into desired sols. After being removed from the sol, the membranes would often curl and stick to themselves. The filled template was placed onto a paper towel and uncurled before it was set to dry. As the sol began to gel, the template began to shrink through forces generated by the tension of the gelling film. After air-drying, samples were placed in a furnace set at 650 °C for 15 minutes. An undulated thin film morphology, Figure 2.8a, was the result when flash heating was used with the dip-coated PC template. No evidence of tubes or fibers were present on these films. The slow heating of samples at a rate of 50 °C/h to the desired temperatures, similar to those used for the AAO templates, was adopted for the dip-coating method. SEM analysis of templates calcined from this procedure also resulted in the formation of an undulated material. The undulated morphology was found to occur because the PC template would shrink as it was heated. The undulated film morphology was prohibited through reinforcement of the templates between Al_2O_3 slides

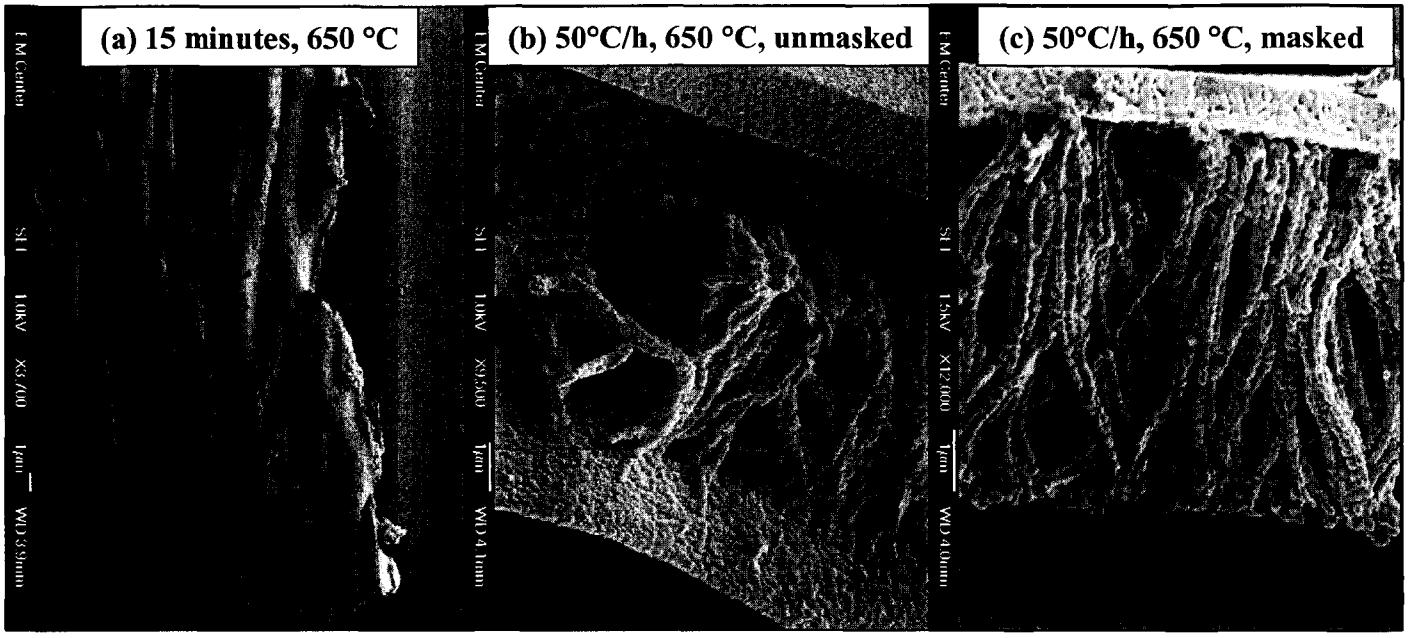

Figure 2.8. SEM images that illustrate the development of the sol-gel template synthesis for PbTiO3 samples using PC templates. (a) Undulated thin film morphology resulting from a dip-coated template flash calcined at 650 °C for 15 minutes. (b) Nanofibers between two surface films resulting from a dip-coated PC template, reinforced between Al_2O_3 plates and slowly calcined at 50 °C/h to 650 °C. (c) Fibers attached to surface film resulting from drop-wise coating onto a masked template. Templates were reinforced between Al_2O_3 and calcined at 50 °C/h to 650 °C.

during the calcination process similar to the treatment of the AAO templates. SEM analysis of the resulting morphology, Figure 2.8b, revealed the formation of fibers sandwiched between two surface films. This method allowed for the identification of fibers adhered to straight or flat films.

Drop-Wise Coating Process Using Masked PC. The optimized methodology for the AAO templates was applied to the PC template procedures. Templates were masked and coated with one or two drops of sol to wet the template. The masked surface did provide stability to the template during the coating process. The template no longer curled upon itself and shrinkage was reduced upon drying. Polishing the uncalcined surface film could not be performed because the polishing tools were too abrasive and would tear the template. The dried templates were inserted between Al_2O_3 slides and calcined at 50 °C/h to 650 °C. The resulting morphology, Figure 2.8c, was fibers attached to one surface film. Fibers that were free of both surface films were observed by SEM and TEM analysis in many samples.

VII. Summary.

Sol-gel template synthesis was applied to the perovskite materials. Several experiments were performed to optimize a specific methodology developed from the techniques practiced by Lakshimi and Limmer.[7,14] The results in this thesis demonstrated that removal of the AAO template is difficult to perform when it is calcined above 400 °C. Characterization of our materials presented in the subsequent chapters does not detect any remaining AAO template. Attention to the elimination or reduction of surface film was made in an effort to accurately measure the grain/crystallite effect of the

nanostructures formed within the commercially available templates. This was performed by masking one side of the template prior to coating, and polishing surface films before calcination. Finally, the synthetic and characterization techniques developed for this research were reviewed.

References

(1) Lessing, P. A., *Ceram. Bull.* **1989,** 68, 1002-1007.

(2) Fernandes, J. D. G.; Araujo Melo, D. M.; Zinner, L. B.; Salustiano, C. M.; Silva, Z. R.; Alves Junior, C.; da Costa, J. A. P.; Longo, E., *J. Alloys Compd.* **2002,** 344, 157-160.

(3) Vassiliou, J. K.; Hornbostel, M.; Ziebarth, R.; Disalvo, F. J., *J. Solid State Chem* **1989,** 81, 208-216.

(4) Nishide, T.; Yamaguchi, H.; Mizukami, F., *J. Mater. Sci.* **1995,** 30, 4946.

(5) Boyle, T. J.; Dimos, D.; Schwartz, R. W.; Alam, T. M.; Sinclair, M. B.; Buchheit, C. D., *J. Mater. Res.* **1997,** 12, 1022-1030.

(6) Doeuff, S.; Dromzee, Y.; Taulelle, F.; Sanchez, C., *Inorg. Chem* **1989,** 28, 4439-4445.

(7) Lakshmi, B. B. Separtions Using Biological Carrier Immobilized in Porous Polymeric and Sol-Gel Templated Synthesized Nanotubular Membranes. Dissertation, Colorado State University, Fort Collins, **1998**.

(8) Zelenski, C. M. Growth of Chalcogenide Semiconductors Within a Nanoporous Aluminum Oxide Template. Dissertation, Colorado State University, Fort Collins, **1998**.

(9) Jade; Inc., M. D., *XRD Pattern Processing* **1999**.

(10) Klug, H. P.; Alexander, L. E., *X-ray Diffraction Procedures For Polycrystalline and Amorphous Materials*. 2nd ed.; John Willey & Sons: New York, **1974**.

(11) Grams/AI, *Thermo Glatic* **2001**.

(12) Kortum, G., *Reflectance Spectroscopy: Principles, Methods, Applications*. ed.; Springer-Verlag: New York, **1969**; p 111.

(13) Smith, W., *Principles of Materials Science and Engineering*. 3rd ed.; McGraw-Hill: New York, **1996**.

(14) Limmer, S. J.; Cao, G., *Adv. Mater.* **2003,** 15, 427-431.

CHAPTER 3

Examination of Size–Induced Ferroelectric and Antiferroelectric Phase Transitions for Template Synthesized One-Dimensional $PbTiO_3$ and $PbZrO_3$

I. Introduction

One-dimensional (1-D) metal oxides are of significant interest in the research and development of nanotechnology.[1-3] The morphologies of 1-D materials, which include tubes, rods, fibers, and wires, provide unique systems in which the investigation of both aspect ratio and dimensionality can be examined.[4] One approach to an investigation is to systematically produce and study the physical properties of 1-D morphologies derived from the assistance of well-defined templates that ensure control over parameters such as the diameter and length of the materials in question. In an initial communication, we reported the results for an experimental investigation on how sol-gel synthesis could be applied to a template to affect the preparation of nanometer-sized perovskite materials.[5] Our experiments demonstrated that template synthesis not only aided in the control over the geometrical constraints, but also constricted the grain/crystallite size of the perovskites. Our procedure, discussed in Chapter 2, generated interesting models for the examination of size effects that occur with perovskite ceramics having grain sizes below 1.0 μm.

The influence of crystal chemistry and size on the properties of ferroelectric perovskites is of general concern because of the interest in fabricating micro-and nano-scale electronic components. Prior research on ferroelectric ceramics had found the following deviations in polycrystalline samples with grain sizes below 1.0 μm: a decrease in the lattice parameter ratio (c/a) for the ferroelectric unit cell, a decrease in both the ferroelectric phase transition temperature (T_c) and enthalpy (H), which caused the observation of a decrease in polarization and dielectric constants.[6,7] These size effects have been observed in both bulk powder and thin film morphologies, but the fundamental

source of the size effects is still unclear. Several possible mechanisms have been proposed to explain the effects of particle size on the ferroelectric phase transition temperature in perovskites. These have included depolarization effects, the absence of long-range cooperative interactions, structural defects, and elastics constraints.[7]

Among the many commercially relevant displacive ferroelectrics, the $PbTiO_3$-$PbZrO_3$ (PZT) solid solution system is well suited for this research. Also, in contrast to $BaTiO_3$, few studies have appeared that address size effects in $PbTiO_3$ and $PbZrO_3$ systems.[8-20] This chapter reports the examination of the ferroelectric phase transition of $PbTiO_3$ nanotubes and nanofibers as the particle size and, potentially, the aspect ratio are controlled. After the discussion on $PbTiO_3$, results from the investigation on size-induced antiferroelectric phase transitions of $PbZrO_3$ is presented. This is the first report on size induced ferroelectric and antiferrolectric phase transition temperature (T_c) deviations for 1-D perovskites.

Recently, four independent research groups led by Cao, [21-24] Park,[25,26] Mallouk,[27] and Wong[28] have reported on the synthesis and characterization of one-dimensional perovskite materials. In addition to their nanoparticle counterparts, 1-D perovskites have become excellent models to investigate how the ferroelectric crystal structure and state of polarization may be influenced by size and dimensionality by allowing for a unique geometrical constraint on domain behavior. The Park group demonstrated that crystalline single $BaTiO_3$ nanowires with diameters of 10-60 nm could be polarized under vacuum conditions using scanning probe techniques.[26] The wires had ferroelectric domains, with dimensions of several nanometers along the c-axis that were used to write and store information. These results are relevant to the investigation of size effects by

experimentally contributing to the identification of a critical size that is lower than what was previously reported. Using nanoparticle models, Wang et al., determined the critical size of $BaTiO_3$ by Landau-Devonshire theory to be 44 nm, where as Akdogan et al. experimentally determined this value to be 67 nm through interpolation.[18,29]

The ferroelectric $PbTiO_3$ system was also well suited for these studies because of its relatively low processing temperature for the chelate sol-gel method (between 450-800 °C) versus $BaTiO_3$ (above 1100 °C).[7,30,31] Chapter 4 discusses the $BaTiO_3$ system in further detail. The processing temperature needed to obtain the ferroelectric phase is critical in considering the stability of the alumina template used to form the sub-micron sized particles. Synthetic processing conditions as well as the important size effects on the ferroelectric transition temperature of one-dimenisonal perovskites will be addressed in this chapter.

II. Experimental Method: The perovskite nanotubes, fibers, and bulk powders were prepared from 0.8 M chelate sol-gels as described in Chapter 2. Because of the esterfication pathways of the chelate sol and its effect on microstructure, only fresh sols were used to fabricate tubes and fibers.[32,33] The nanostructures were calcined in air at a rate of 50 °C/hour to 650 °C, and were kept at this temperature for 6 hours before being slowly cooled to room temperature at a rate of 30 °C/hour. The remaining unused sol was allowed to gel and was calcined using the same heating procedures to produce our "bulk" powders as the control sample. The $PbTiO_3$ bulk powder samples were calcined at the following temperatures: 450°, 550°, and 650 °C. The $PbZrO_3$ bulk powders were calcined at 650 °C.

III. Results and Discussion

The effect of each template on the morphology of the $PbTiO_3$ nanostructures made using a 0.8 M chelate sol and the influence of crystallite size and aspect ratio upon the room temperature crystalline symmetry of these structures have been explored. In reviewing the experimental literature on size effects upon the $PbTiO_3$ ferroelectric phase transition, it is difficult to determine an exact critical size. $PbTiO_3$ nanoparticles, with crystallites on the order of 8-200 nm, have been prepared by the sol-gel, chelate, nitrate, citrate, coprecipitation, Pechini, and injection-hydrolysis procedures and various physical characterization and theoretical techniques have been employed acquire the critical size.[8-16,18-20,30,31,34-39] Therefore, we compared our results of the nanotubes and fibers to those of control samples made with the same solution chemistry in the absence of any templates.

III A. Examination of 1-D Ferroelectric Materials

Morphologies and Microstructures of $PbTiO_3$ Bulk Powders, Nanotubes, and Nanofibers. Through electron microscopy, it was determined that each template had an effect on the morphology and microstructure of the samples produced from the 0.8 M chelate sol. With powder processing and no template, the size and shape of the polycrystalline grains were controlled by the heating conditions as in the literature. SEM micrographs of the bulk powder, Figure 3.1, illustrate the effect of this methodology on grain growth after three heat treatments of 450°, 550°, and 650 °C. Grain sizes were measured from the images to be on average ~0.1, 0.3, 0.7 μm, respectively, with increasing temperature. The micrographs also illustrate that there was some distribution

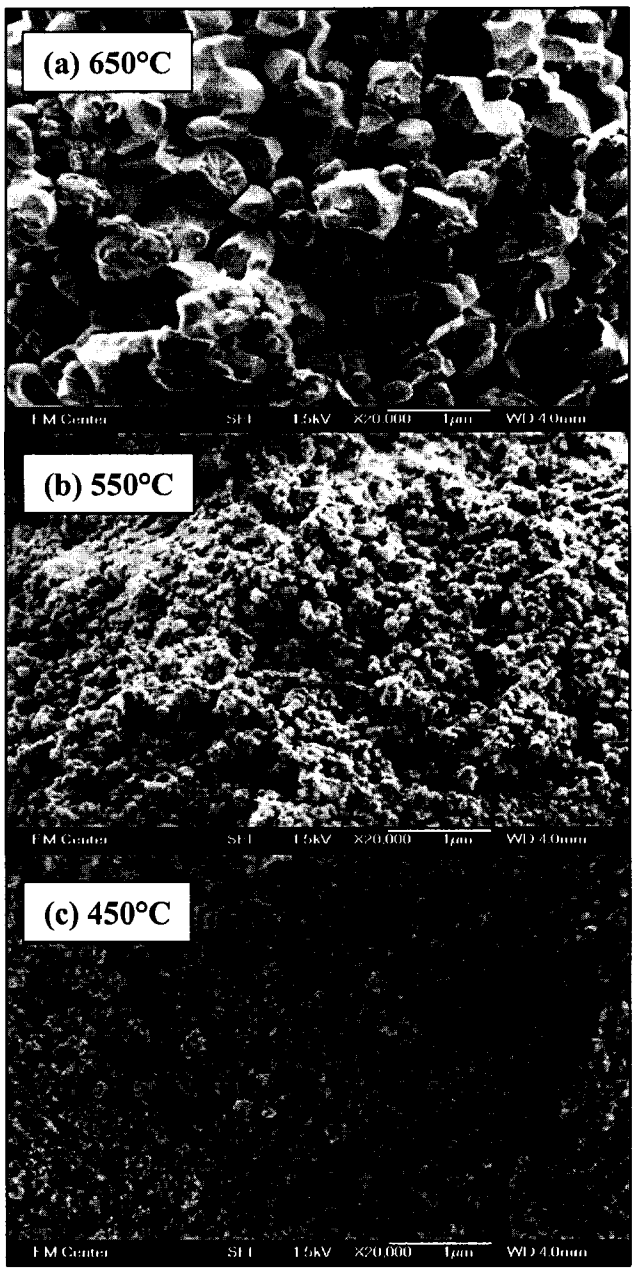

Figure. 3.1. SEM images of the $PbTiO_3$ bulk powder illustrating grain growth and morphologies obtained for calcination temperatures of (a) 650 °C, (b) 550 °C, and (c) 450 °C. Scale bar is 1 μm and micrographs were taken at a magnification of ×20,000.

of grain sizes within each sample. To address this variable, our approach to investigating grain/crystallite size effects on the T_C and the critical size uses the systematic incorporation of membrane templates with 200, 100, and 50 nm pore sizes. In addition to the heating conditions, the templates serve as a second control over grain growth and distribution of grain size. Production of our one-dimensional perovskites was achieved by filling the channels of two types of porous membranes: anodized alumina films and track-etched polycarbonate films. If completely filled, each template has cylindrical nanochannels that will form fibers, or tubes if they are incompletely filled.[1]

The nearly hexagonally close-packed pore surface of the pristine amorphous alumina (AAO) template is shown in Figure 3.2a. After the templates have been filled, heat-treated, and their surface films removed by polishing, the nanostructures could be revealed when the AAO was removed with 6 M NaOH. SEM images, Figures 3.2b and 3.2c, show the top and side views of the calcined $PbTiO_3$ nanostructures that were yielded by our methods. Electron microscopy also revealed that the nanostructures prepared in AAO were typically tubes with outer diameters of ~200 nm, and the lengths were ~50 μm, corresponding to the dimensions of the template. The rounded or smooth film-like features on top of the tube openings were a result of the incomplete removal of the $PbTiO_3$ surface film, see discussion in Chapter 2. Elemental analysis of the nanotubes determined by EDS showed emission lines associated with Pb, Ti, and O, and no emission lines from Al, confirming that the template had been removed. The TEM image and SAD pattern taken for a single $PbTiO_3$ nanotube, Figure 3.2d, revealed that the

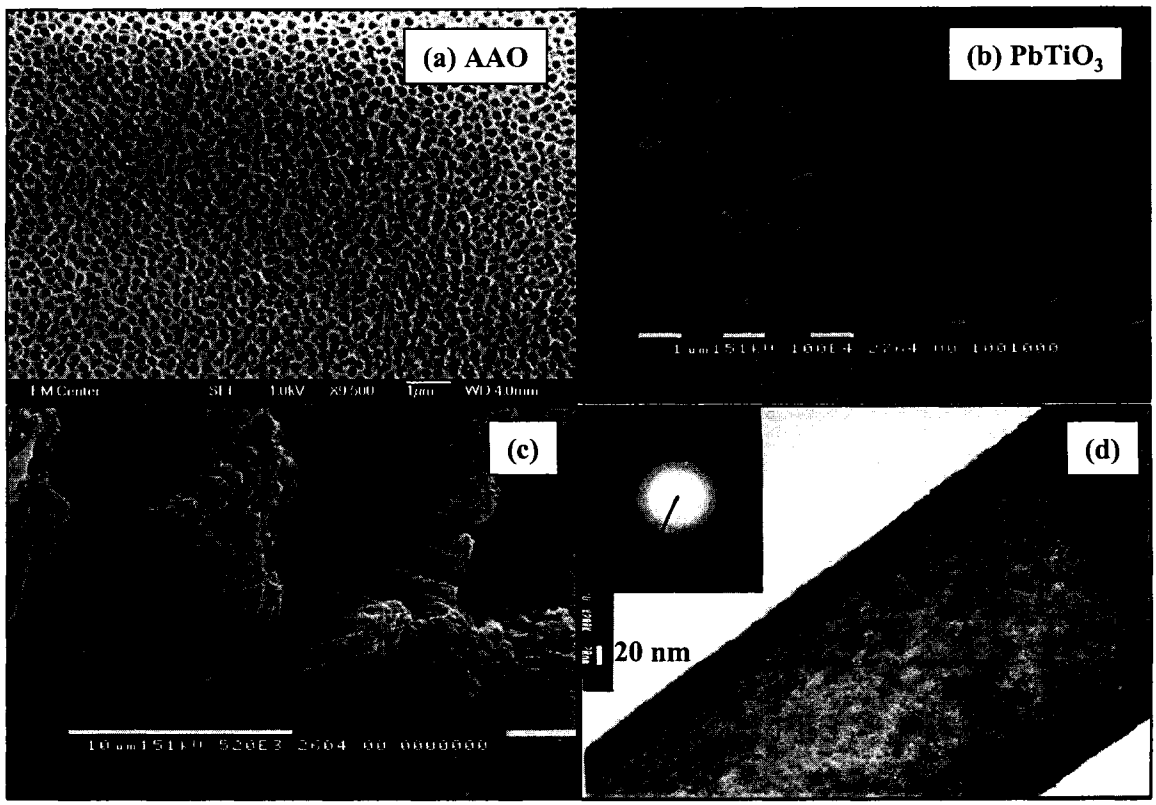

Figure 3.2. FESEM images of (a) the pristine surface of an AAO template, (b) the top view and (c) side view of calcined $PbTiO_3$ nanotubes, showing bundle formation after the removal of AAO. The tubes have an o.d. of 200 nm and are ~50 μm long. The TEM image (d) of a single nanotube, shows that these structures comprise grains < 20 nm, and the inset of the ring pattern indicates that the small grains are polycrystalline. Tubes shown were calcined at 650 °C.

tubes comprised grains that were smaller than the 20 nm scale bar and the electron diffraction ring patterns indicate that these nanostructures were polycrystalline assemblies of smaller crystallites.

Tube formation using the AAO template was the only nanostructure morphology resulting from the chelate sol-gel template method. Attempts to produce nanorods by allowing the template to soak in the sol for longer periods of time (e.g. 30 seconds to 5 minutes), or by changing the concentration of the sol from 0.3-0.8 M, were unsuccessful and yielded only tubes. Previously, the formation of TiO_2 nanorods from tube structures was achieved when the template was in contact with a colloidal sol for increasing time periods; however, the sol used in our experiments was homogenous and stable colloidal sols did not readily form.[40] Through analysis of SEM images, it appeared that varying the concentration of the Pb/Ti chelate sol did not have a significant effect on the tube wall thickness. One additional experiment, aimed at the formation of rods rather than tubes, was to build up the wall thickness by successive coatings of the template. Due to the fragility of the AAO template, polishing of the surface films destroyed the template before it could be recoated.

The rough, untreated surface of the track-etched polycarbonate (PC) membrane template, with its randomly distributed 200 nm pores, is shown in Figure 3.3a. This template was removed from the structures during the calcination process by combustion in air. Figure 3.3b is the SEM top view and Figure 3.3c is the side view of the resulting fiber structures formed within the 200 nm PC template when calcined at 650°C. Masking one surface of the PC template prevented film formation on one side of the membrane. Figure 3.3c shows that the ~6 μm long fibers were adhered to a ~1 μm thin film formed

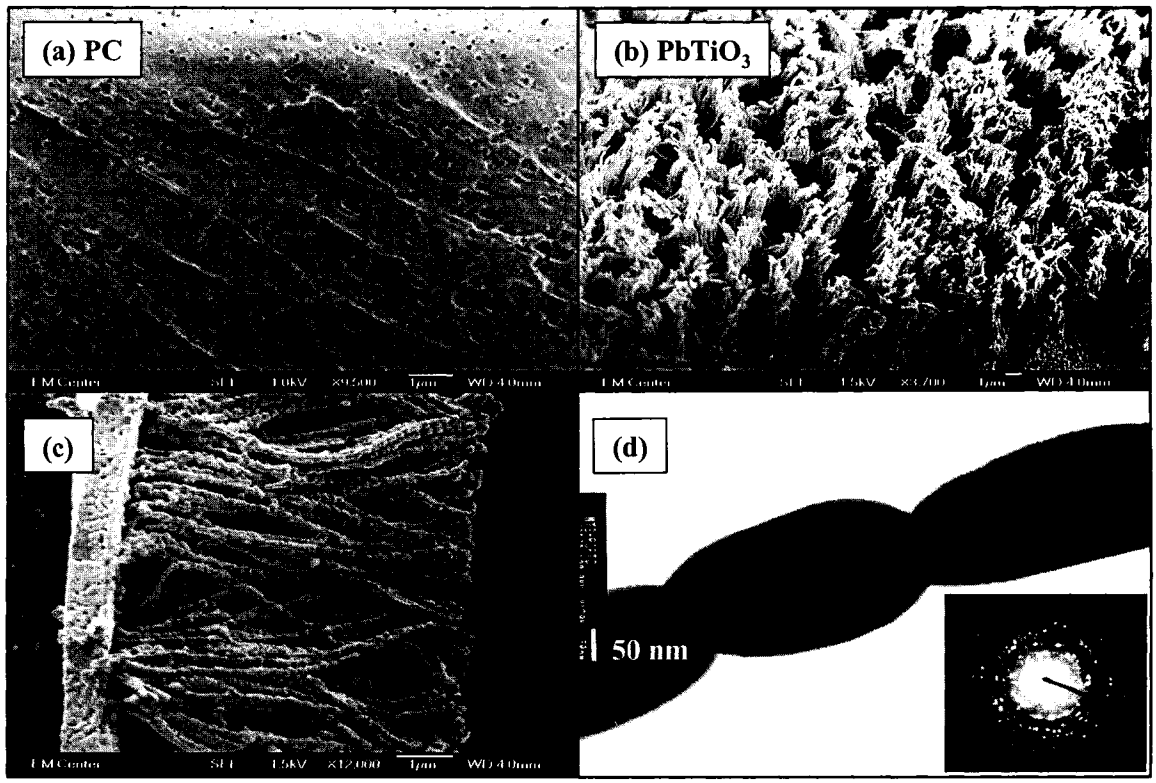

Figure 3.3. FESEM images of (a) the pristine surface of the 200 nm pore PC template, (b) the top view of $PbTiO_3$ nanofibers and (c) side view showing the attached (~6 μm) fibers to a 1 μm thick surface film, after the removal of the template. The TEM image (d) confirms that the structures are solid and are made up of a string of grains ~200 nm in diameter. The inset shows that these grains are polycrystalline. Fibers shown were calcined at 650 °C.

on the coated side. The grain sizes of the surface film were on average 0.75 μm. The TEM image and SAD pattern for a single $PbTiO_3$ nanofiber are shown in Figure 3.3d. Solid fibers comprised a string of individual grains that were polycrystalline and vary in length, but were ~200 nm wide in diameter.

The uniquely different morphologies and grain sizes of our nanostructures made from sols of the same concentrations but different templates, illustrates *for the first time* a significant template effect. One explanation for fiber versus tube formation may be the difference in the length of the nanochannels within the templates. Production of a fiber from tube morphology is a result of complete versus incomplete filling of the nanochannels within the template.[1-4] During our coating process, the sol entered the channels through capillary action. Each template used had hydrophilic surfaces and uptake of a polar solution should have easily occurred. As the 0.8 M solution entered the 200 nm template channels of different lengths (~50 μm for AAO and ~10 μm for PC), incomplete filling or coating of the AAO template for the longer channel may have resulted, while complete filling was observed in the PC channel. In effect, the shorter channel length allowed for more solution to enter.

Completely filled templates and unique sintering profiles heating at 50 °C/hr to 650 °C may also explain why the fibers have the "string" of grains morphology from the PC template with diameters very close to the 200 nm template pore diameter. Recently, 200 nm polycarbonate templates were used in the growth of $BaTiO_3$, $Pb(Zr_{0.53}Ti_{0.48})O_3$, and other oxide nanorods using sol-gel electrophoresis.[21-24] The templated sols were heat treated at 700 °C for 15 minutes. The metal oxide rods produced from this flash heating method resulted in structures having rod diameters and grains quite smaller than the

fibers observed here.[22,23] During the heating stage, the templated sol-gels underwent densification and shrinkage to produce rods ~125-180 nm in diameter. This flash heat treatment probably helped ensure the growth of smaller polycrystalline grains. An examination of Limmer's flash heating method resulted in the formation of an undulated thin film morphology, Figure 2.7a. Structural analysis by PXRD and Raman spectroscopy, on bulk powders and templated samples heated at 650 °C for 15 minutes and 1 hour, revealed a significant amount of PbO present. Because of these poor results, the flash heating method was abandoned. The formation of nanotubes from the PC templates was explored by changing the concentration of the sol and the results from these experiments are presented in Chapter 4.

Evaluating Room-Temperature Lattice Structure of $PbTiO_3$ Powders, Tubes and Fibers. The room-temperature crystalline symmetry of the nanotubes and fibers was determined by powder X-ray diffraction, electron diffraction, the method of comparative *d*-spacing, and Raman spectroscopy. These methods were used to verify whether the templates used in this experiment were successful in both limiting grain/crystallite size and retaining the tetragonal ferroelectric phase.

Powder X-ray Diffraction. The average room-temperature crystal structure was evaluated with PXRD. Lattice parameters and average crystallite size calculated from the PXRD data are summarized in Table 3.1. Bulk powders, were calcined at 450°, 550°, and 650°C and their respective powder patterns, Figure 3.4, illustrate the effects of crystallite size on the relative intensity and broadening of the peaks. Each pattern was indexed to the tetragonal unit cell and space group P4/mmm (123).[20] PbO (small broad peak $2\theta = 29°$) was observed in the bulk sample calcined at 650°C.

The average crystallite size found within the grains of the bulk powders calculated from the (111) reflection using the single line parameterized Warren-Averbach method were 29 ± 3, 49 ± 5, and 157 ± 16 nm for the respective heating conditions. This method of analysis was used instead of the Scherrer equation because it considers both microstrain and crystallite size, while the Scherrer equation assumes that loose powder is free of microstrain.[41,42] Akogdan's recent work on the measurement of critical size using diffraction techniques illustrated that microstrain increased for $PbTiO_3$ nanoparticles < 75 nm and therefore is not negligible for mesocopic ferrolectrics when evaluating size.[8] In addition, the SEM images indicated that these powders were agglomerated and both tubes and fibers have grains that are under some strain to form the morphology; thus, it could not assumed that microstrain had no effect. The average crystallite sizes calculated for the powders are also smaller than average grain size measured from the FESEM image, Figure 3.1. This discrepancy implies that the grains of the bulk powders were composed of multiple crystals and were not single-crystalline. The effect of crystallite size on the relative tetragonality (c/a) of each sample was monitored and compared to the c/a = 1.065 from the PDF file.[43] A decrease in the c/a of ~ 0.6, 0.5, and 0.2% was found for the powders with crystallite sizes of 29, 49, and 157 nm, respectively.

Diffraction patterns of the nanofibers, Figure 3.5, made from the 200, 100, and 50 nm pores of PC templates were also indexed to the tetragonal phase. Crystallite sizes for the fibers made from their respective templates were determined to be 72 ± 7, 57 ± 6, and 53 ± 5 nm, respectively. It is important to note that these results are based on crystallites measured from fibers attached to a thin film, each with different sized grains. The (c/a) values for the fibers were similar to the bulk powders having 29 and 49 nm

Table 3.1. Unit Cell Parameters and Crystallite Size Data for $PbTiO_3$

Material & Processing Temperature	a (Å)	c (Å)	c/a	V (Å^3)	Crystallite [a,b]Size (nm)
Reference 42	3.899	4.153	1.065	63.1	---
650 °C Powder	3.887(2)	4.132(5)	1.063	62.4	157 ± 16
550 °C Powder	3.894(1)	4.126(4)	1.060	62.6	49 ± 5
450 °C Powder	3.903(1)	4.132(4)	1.059	62.9	29 ± 3
650 °C Fibers 50 nm	3.906(1)	4.141(2)	1.060	63.2	53 ± 5
650 °C Fibers 100 nm	3.899(1)	4.128(1)	1.059	62.7	57 ± 6
650 °C Fibers 200 nm	3.899(1)	4.132(1)	1.060	62.8	72 ± 7
Reference 45	3.961		1.000	62.2	---
650 °C Tubes 200 nm	3.966(3)		1.000	62.4	11 ± 1
650 °C Thin Film on AAO	3.895(1)	4.113(1)	1.056	62.4	29 ± 3

[a] Tetragonal crystallite size determined with the (111) reflection
[b] Cubic crystallite size determined with the(110) reflection

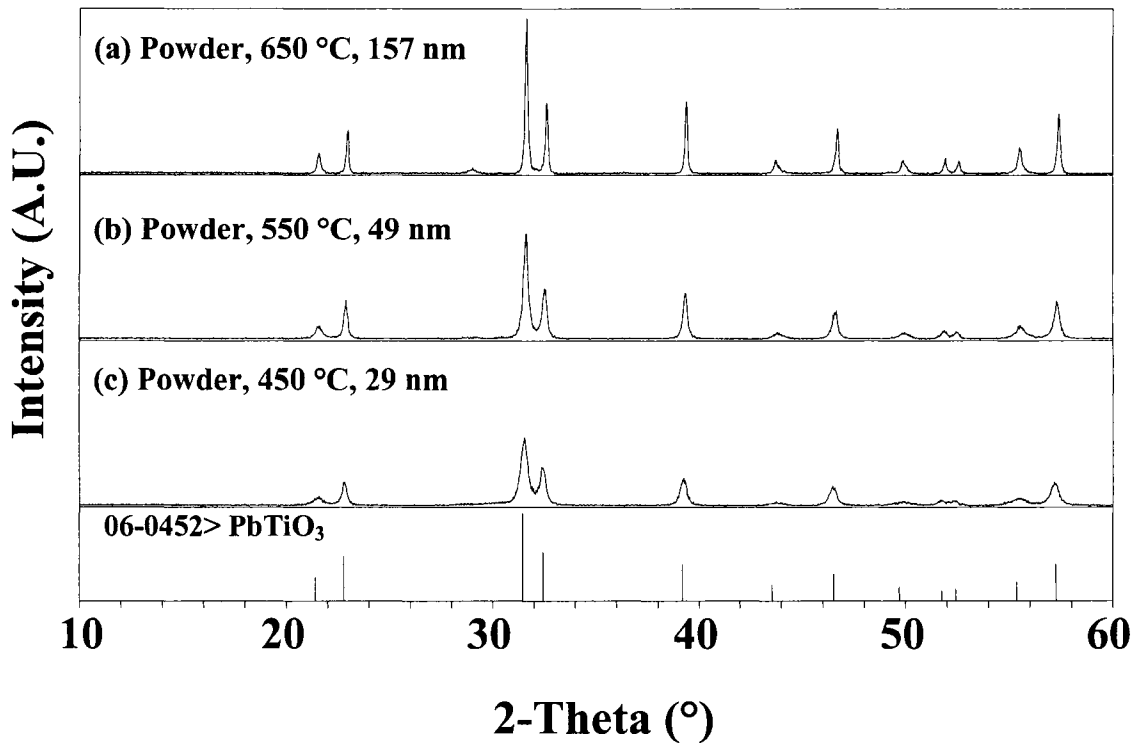

Figure 3.4. Powder XRD patterns for the bulk material calcined at (a) 650 °C, (b) 550 °C, and (c) 450 °C with 157, 49, and 29 nm crystallite sizes, respectively. Each sample was indexed to have the tetragonal phase and illustrated the effects of grain/crystallite size on the relative intensity and broadening of the peaks.

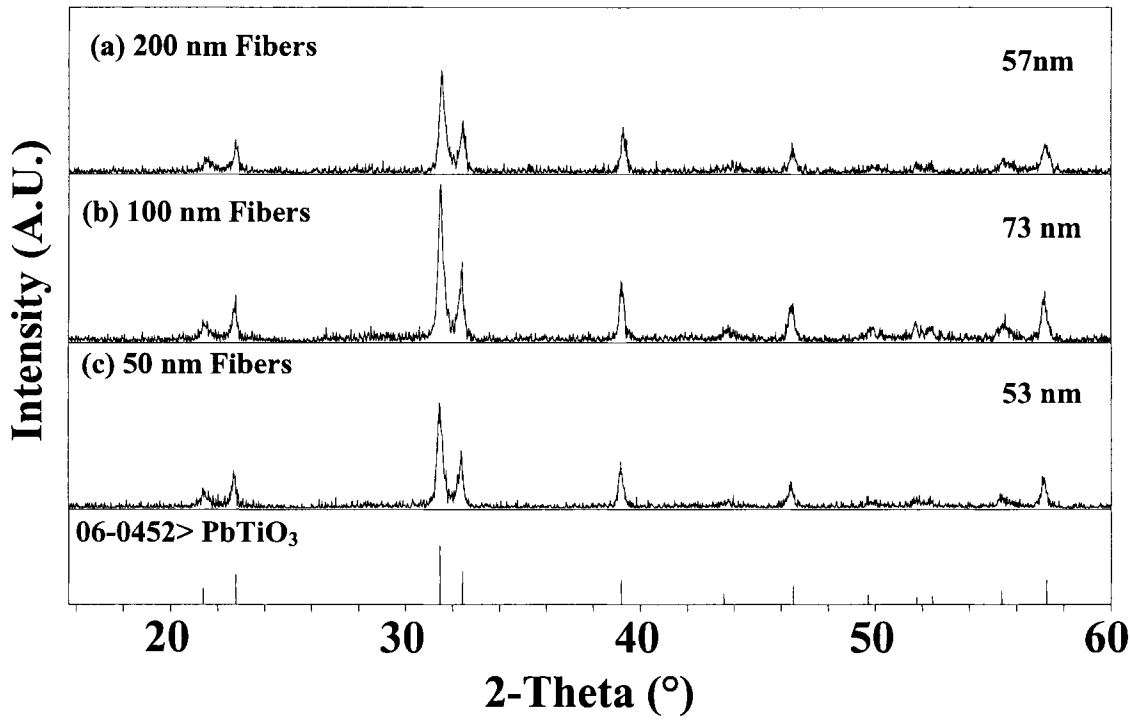

Figure 3.5. Powder XRD patterns of tetragonal $PbTiO_3$ fibers formed inside of (a) 0.2 μm (b) 0.1 μm and (c) 0.05 μm pore diameter PC templates calcined at 650 °C. Average crystallite sizes were determined to be 57, 73, and 53 nm for the respective sample size.

crystallite sizes. Figure 3.6 shows that two displacive phases were obtained from the 200 nm AAO template. After calcination, the coated side of the AAO templates had a surface film with the tetragonal ferroelectric phase of $PbTiO_3$, an average crystallite size of 29 nm, and a c/a = 1.056. After the surface film was removed and the AAO dissolved, the sample was reevaluated and found to have the cubic paraelectric phase of $PbTiO_3$.[44] The (110) reflection was used to calculate an average crystallite size of 11 nm which is in accordance with the grain size measurement from TEM, Figure 3.2d, and may be single-domain.[9] The conflicting analysis between the two XRD patterns are a result of the measured crystallite size for the nanotubes and surface film.

A limitation in using PXRD to evaluate nano-scale materials is the effect of line broadening that occurs as the particle or grain size decreases, thus causing a pseudocubic structure to be oberved.[42] Therefore, a complementary evaluation was required to determine if the nanotubes were tetragonal. Table 3.2 lists the measured and calculated values for the tetragonal phase obtained from the PXRD data and the SAD ring pattern for the method of comparative *d*-spacings. Comparing the observed ratios of the ring pattern radii, it was concluded that they were close to the ratios of the literature and measured d-*spacing* values for the tetragonal phase. To confirm this result further, Raman scattering, which has shown to be more sensitive for the detection of tetragonal symmetry and phase transitions in nano-scale particles of $PbTiO_3$ and $BaTiO_3$ was used in conjunction with PXRD. [7]

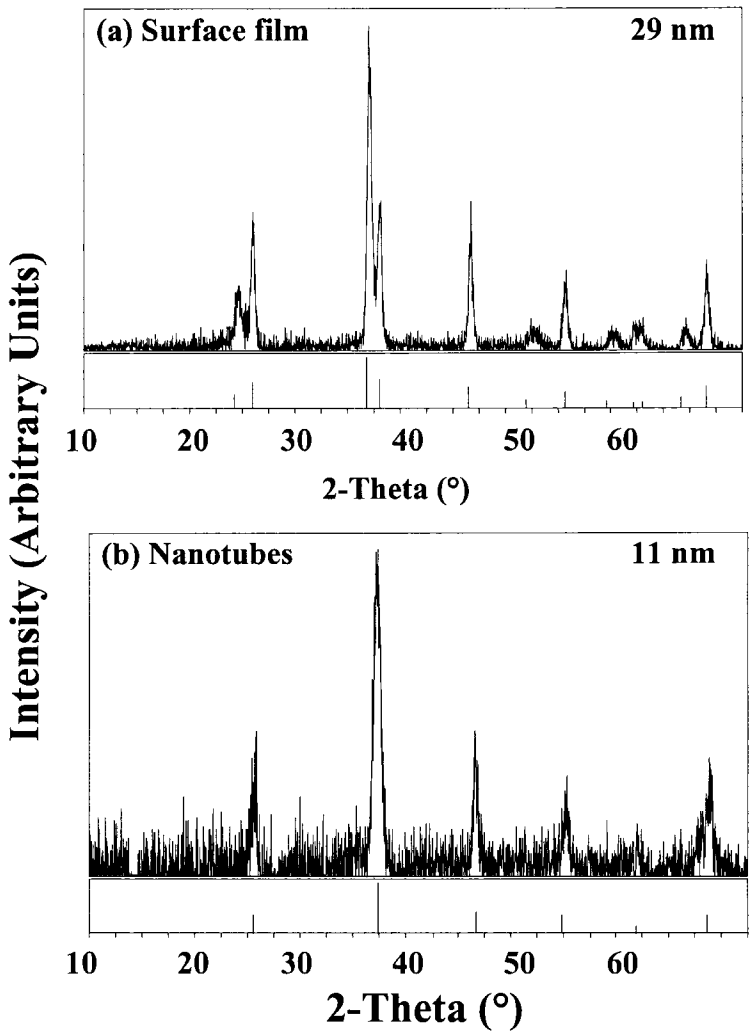

Figure 3.6. Powder XRD patterns for two phases obtained with samples made with AAO and calcined at 650 °C. Pattern (a) is of the residual surface thin film on the template after polishing and has the tetragonal phase. Pattern (b) is of the isolated nanotubes and has the cubic phase. Differences in the two phases are a result of the average crystallite size measured from the samples. The average crystallite size for the surface film was calculated to be 29 nm, whereas the tubes were 11 nm

Table 3.2. Comparative d-spacing Measurements for $PbTiO_3$ Nanotubes and Bulk Powder Calcined at 650 °C

Ref. 44 d-spacing (XRD) Å	Measured *d*-spacing (XRD) Å	Measured Radius (SAD) mm (± 0.5)	Calculated[a] d-spacing (SAD) Å
$d_{100} = 3.90$	$d_{100} = 3.87$	$r_{100} = 10.50$	$d_{100} = 3.90$
$d_{110} = 2.76$	$d_{110} = 2.75$	$r_{110} = 15.00$	$d_{110} = 2.73 \pm 0.17$
$d_{200} = 1.95$	$d_{200} = 1.94$	$r_{200} = 21.25$	$d_{200} = 1.93 \pm 0.12$
$d_{211} = 1.61$	$d_{211} = 1.60$	$r_{211} = 25.25$	$d_{211} = 1.62 \pm 0.10$

[a]First line was assumed to be $d_{100} = 3.90$ from Reference 44.

Raman Spectroscopy. The crystal symmetry of the perovskites was confirmed by Raman spectroscopy at room temperature. These results are summarized in Table 3.3. Ferroelectric $PbTiO_3$ is an ideal perovskite to study with Raman because the selection rules below the transition temperature (T_c) in the tetragonal ferroelectric phase are obeyed for all the modes, and the Raman scattering peaks are sharp and the modes are under damped below T_c.[45,46] According to group theory, the cubic (m3m) phase for $PbTiO_3$ has 12 optical modes that transform in to the $3T_{1u}$ $+T_{2u}$ irreducible representations.[47] The T_{2u} "silent" mode is neither Raman nor infrared active, whereas the three T_{1u} modes are infrared active. In the tetragonal structure, the spontaneous polarization resulting from the elongation of the c-axis and displacement of the Ti^{4+} with in the TiO_6 causes the triply degenerate modes to be reducible. Through correlation of the site symmetry from the cubic (m3m) to the tetragonal (4mm) phase, we find that these representations reduce as follows: $3T_{1u} \rightarrow 3A_1 + 3E$ and $T_{2u} \rightarrow B_1 + E$. These modes are all Raman active.

The spectra for the bulk powders, Figure 3.7, have peaks that are assigned to the vibrational modes for tetragonal symmetry determined for single crystals of $PbTiO_3$.[46,48] Peaks marked with an asterisk are lattice modes that undergo changes resulting from both phase transformation and crystallite size. The $E+B_1$ is designated as a silent mode and appears to be independent of size effects and phase behavior. The effect of reducing crystallite size is observed in the spectra through two parts. The E(2TO) peak undergoes a decrease in its relative intensity and the frequency of the low energy E(1TO) soft mode near 88 cm^{-1} decreases with line broadening. This lowest energy mode is an indicator of

Table 3.3. Raman Scattering Data for $PbTiO_3$ Bulk Powders, Tubes and Fibers

Sample Material	PXRD Symm. d_{XRD} (nm)	$\nu_1(cm^{-1})$ E1(TO)	$\nu_2(cm^{-1})$ A_1(1TO)	$\nu_3(cm^{-1})$ E(2TO)	$\nu_4(cm^{-1})$ E + B1	$\nu_5(cm^{-1})$ A_1(2TO)	$\nu_6(cm^{-1})$	$\nu_7(cm^{-1})$ E(3TO)	$\nu_8(cm^{-1})$ A_1(3TO)
650 °C Powder	Tetr 157	88	151	216	289	334	414	506	626
550 °C Powder	Tetr 49	88	151	216	289	344	447	507	615
450 °C Powder	Tetr 29	86	154	219	290	----	----	507	----
650 °C Tubes 200 nm	Cubic 11	85	155	216	293	----	439	509	613
650 °C Fibers 200 nm	Tetra 73	88	152	219	290	347	449	508	612
650 °C Fibers 100 nm	Tetra 57	88	151	219	290	346	433	508	918
650 °C Fibers 50 nm	Tetra 53	87	151	218	290	----	----	507	623

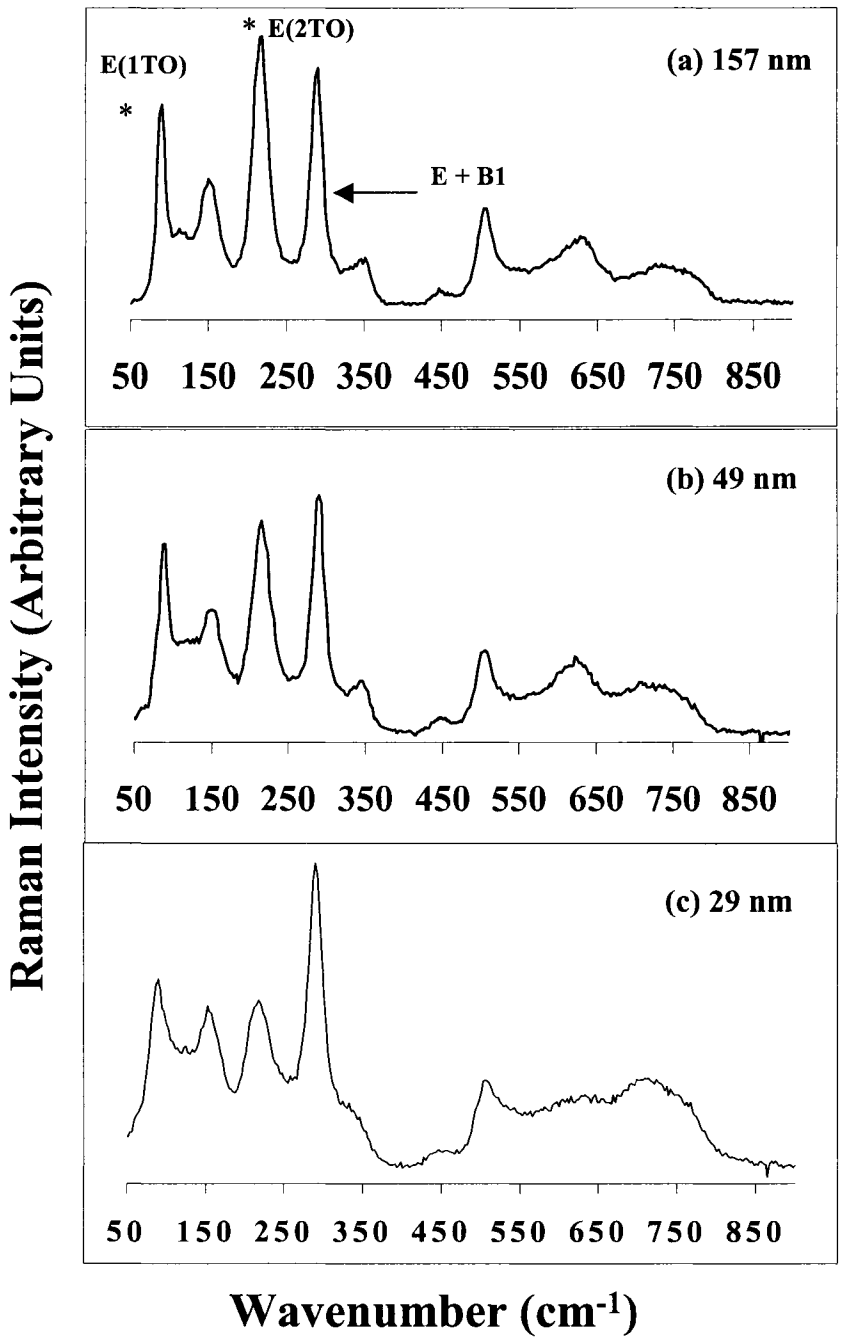

Figure 3.7. Room temperature Raman spectra of the bulk powders with (a) 157 nm, (b) 49 nm, and (c) 29 nm crystallite sizes. The effects of reducing grain/crystallite size are seen with a decrease in relative intensity of E(2TO) and frequency of E(1TO) modes (marked with asterisks).

phase transition and dielectric behavior.[45] Evaluation of our bulk powders showed an E(1TO) mode frequency decrease from 88 to 86 cm^{-1} as crystallite size was reduced. These deviations were first reported in polycrystalline $PbTiO_3$ derived from sol-gel processing.[30,31]

Spectra for the nanofibers and nanotubes produced from the 200 nm pore templates confirm that they are tetragonal, Figure 3.8. Nanofibers made from 100 and 50 nm PC templates have spectral line shapes similar to the 200 nm sample. The fibers have E(1TO) frequencies of 88 cm^{-1} for crystallite sizes of 73 and 57 nm, and 87 cm^{-1} for 53 nm. These results can be compared to Ishikawa's work wherein nanoparticles above 52 nm had no significant difference in Raman shift when compared to single crystal data.[49] Observing lattice modes for tetragonal symmetry for the nanotubes with an 11 nm crystallite size indicated that the tubes were in the ferroelecetric phase and not in the paraelectric phase. The nanotubes had an E(1TO) frequency of 85 cm^{-1}. Similar room temperature Raman spectra have been reported by Fu et al., for nanocrystalline material made by sol-gel techniques having a 17 nm average crystallite size and by Zhou *et al.*, for 18 nm crystallites.[13,20] A broad and undefinable spectrum was also reported by Zhou for a sample with 15 nm crystallite size.[20] In comparing the effects of crystallite size on the E(1TO) mode for the tubes and the fibers, it was found that the soft mode frequency are less than the reported single crystal frequency of 89 cm^{-1}, but not significantly different from the bulk powder control samples. The nanotubes, which displayed the lowest frequency, were comparable to Zhou's data for an 18 nm crystallite size of E(1TO) = 84 cm^{-1}; whereas, the 15 nm crystallite size had an E(1TO) mode of 74 cm^{-1} determined from peak fitting poorly-resolved spectrum.[20]

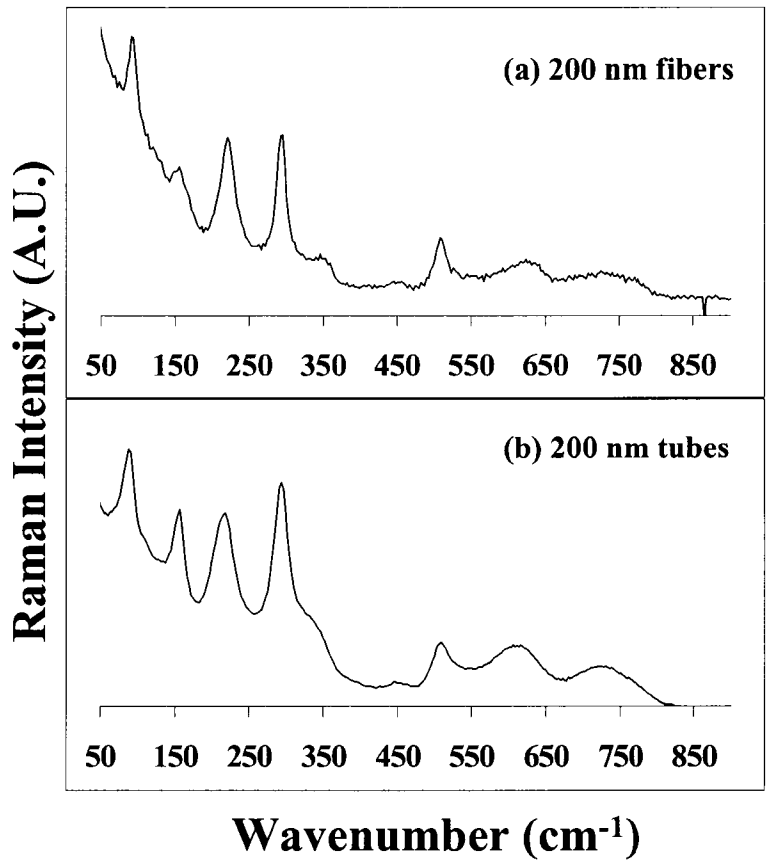

Figure 3.8. Room temperature Raman spectra for the 200 nm $PbTiO_3$ (a) fibers and (b) tubes calcined at 650°C verifying tetragonal symmetry in both samples.

In contrast to single crystal data under ambient conditions, these Raman shifts are the most distinct feature for nanoparticulate polycrystalline powders. Burns and Scott demonstrated, using in situ temperature experiments, that there was a temperature dependence on mode strength for $PbTiO_3$ single crystals.[46] They observed that as the Curie temperature (T_c = 493 °C) was approached, the E(1TO) soft mode, located at 89 cm^{-1}, moved toward lower energy. This feature also occurred with high-pressure experiments that forced the tetragonal unit cell towards the cubic phase.[50] The decrease in E(1TO) frequency with nanocrystalline material under ambient conditions has been attributed to an increase in surface tension as nanoparticles become smaller. Blum,[31] Ma et al.,[15] and Zhou et al.,[20] who have all postulated that the decreases in frequency of the peaks could be due to hydrostatic pressure, provided the initial explanation for the frequency shift coupled to the particle size. These studies compared their nanocrystalline $PbTiO_3$ powders to single crystals that were placed under hydrostatic pressure. Blum's data was compared to a single crystal that was under 1GPa.[50] Ma reported that particles with ~40 nm crystallites had Raman scattering frequencies similar to a single crystal under 2 GPa with an E(1TO) = 78 cm^{-1}. Hydrostatic pressure has also been used to explain phonon mode behaviors observed with thin films of $PbTiO_3$ deposited on Pt/Si substrates.[51] Fu et al. reported that $PbTiO_3$ films with an average grain size of 47 nm had E(1TO) = 80 cm^{-1} (~1.35 GPa). The studies concluded that because nanocrystals have a large surface to volume ratio, the large surface tension could cause internal stress analogous to the hydrostatic pressure effect on single crystals. The results reported in this Chapter confirm a slight decrease in energy, but do not conclude that the crystallites in the nanostructures were undergoing internal stresses equivalent to 1-2 GPa.

The results of both the X-ray diffraction and Raman scattering experiments demonstrated that the templates and chemistry used were successful in obtaining the ferroelectric phase in one-dimensional materials. Analysis of the effects of crystallite size on the tetragonal crystal system of our samples indicates that deviations from unit cell parameters occurred. The largest tetragonal lattice strain, ~0.6%, was observed in the bulk powders and fibers, and the tetragonal lattice symmetry was determined for our nanotubes. Our data indicate that the stresses of surface to volume ratio of our grains on the crystallites are not equal to the 2 GPa reported by Ma and Zhou. Based on the electron micrograph results that both fibers and tubes are geometries composed of grains, which should be under a certain amount of "hydrostatic pressure", it would be expected to observe larger deviations in the E(1TO) soft mode frequency, especially for the nanotubes.

There are two explanations for the deviation from Ma and Zhou's hypotheses. First, the soft mode frequency shifts may result from the larger grain/crystallite sizes of the minor surface film that remain on our tube samples and thin film attached to the fibers; therefore, the E(1TO) frequency of the nanotubes and fibers appeared similar to the bulk powders. Second, under ambient conditions, the decrease in soft mode frequency due to hydrostatic pressure on the individual grains created by surface tension is not as dramatic as previously reported and may be misleading. Recently, Akdogan et al., confirmed the latter explanation. They reported that the (c/a)$\rightarrow$1 with decreasing particle size could not be attributed to surface effects since the requirement of several gigaPascals of pressure created by the surface itself was a physically unrealistic situation.[29]

Research on nanoparticles generally concludes that the spherical particle model is appropriate because it is unbounded and relieved of the microstrains that occur with thin films due to grain boundaries and internal stresses; however, a drawback to this notion is that agglomeration of the particles does occur as seen with our bulk powders, Figure 3.1. So nanoparticles are not entirely free of these constraints. A more appropriate understanding of the reduction in ferrolectricity may lie with what is happening within the core of the nanoparticle and not its surface tension.[29]

III B. Examination of 1-D Antiferroelectric Materials.

Both PC and AAO templates were employed to fabricate 1-D materials of the prototypical antiferroelctric perovskite $PbZrO_3$. This is the second compound in the solid solution of $Pb(Ti,Zr)O_3$ (PZT) materials. Grain size effects of $PbZrO_3$ and PZT have shown similar changes observed with $PbTiO_3$ and $BaTiO_3$ in transition temperature and dielectric constants.[17,52,53] In the studies herein, the resulting morphologies of 1-D $PbZrO_3$ were nanotubes from AAO and nanofibers from PC templates, Figure 3.9. The grain sizes observed for the nanotubes were ~20 nm with TEM. Nanofibers were not examined with TEM.

Powder X-ray Diffraction. The room-temperature crystal structure was evaluated with PXRD. Lattice parameters and average crystallite sizes calculated from the PXRD data are summarized in Table 3.4. $PbZrO_3$ bulk powder and 200 nm fibers, Figure 3.10, calcined at 650 °C were indexed to have the orthorhombic unit cell and space group P2bc (32).[54] The average crystallite size for the respective samples calculated from the (240) reflection was 79 ± 8 and 23 ± 2 nm. The diffraction pattern for the nanotubes,

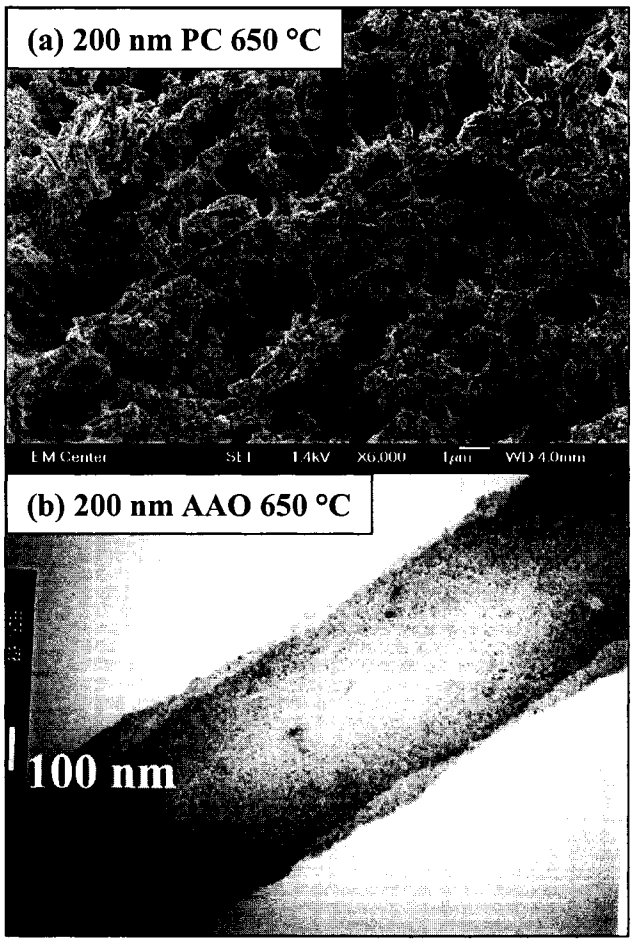

Figure 3.9. FSEM images of $PbZrO_3$ (a) 200 nm fibers formed form a PC template. TEM image (b) of $PbZrO_3$ nanotubes formed from AAO template. Samples were calcined at 650 °C.

Table 3.4. Cell Parameters and Crystallite Size for $PbZrO_3$ Calcined at 650 °C

Material	a (Å)	b (Å)	c (Å	V ($Å^3$)	Crystallite [a]Size (nm)
Reference 53	8.232	11.776	5.882	570.17	----
Powder	8.223(6)	11.717(9)	5.861(5)	564.72	79 ± 8
200 nm Fibers	8.235(4)	11.863(10)	5.852(3)	571.65	23 ± 2
200 nm Tubes	8.237(1)	11.794(10)	5.887(5)	571.87	15 ± 2

[a]Crystallite size calculated from the (249) reflection

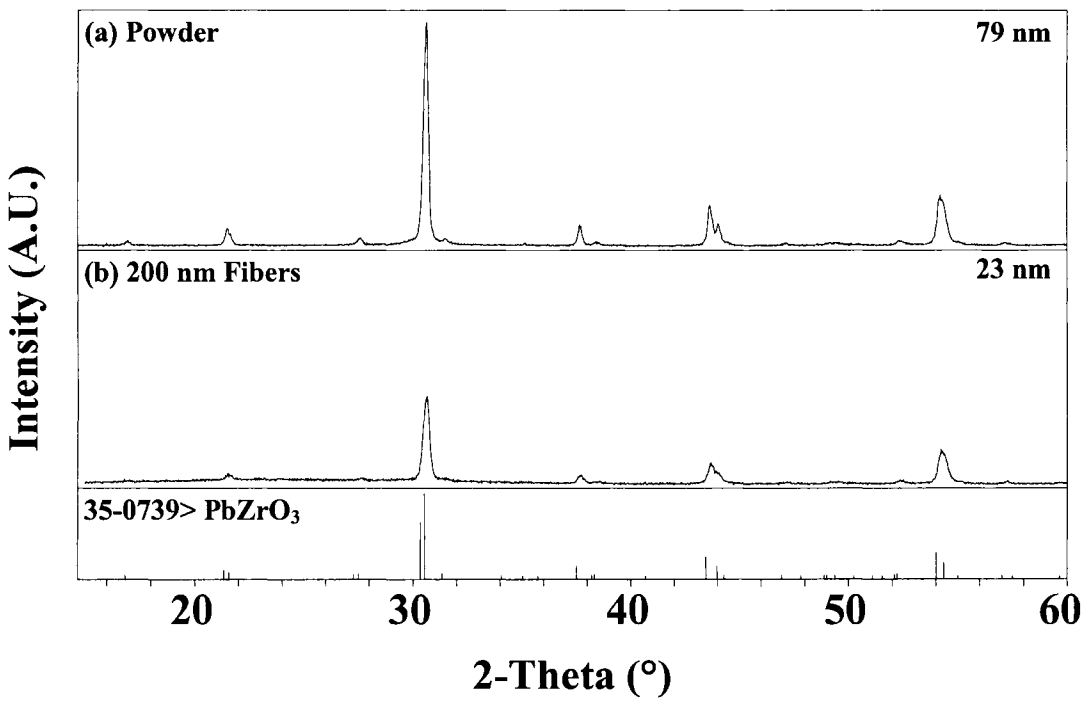

Figure 3.10. PXRD patterns of $PbZrO_3$ (a) bulk powder and (b) 200 nm fibers with average crystallite sizes of 79 and 23 nm, respectively. Both samples were indexed to the orthorhombic phase.

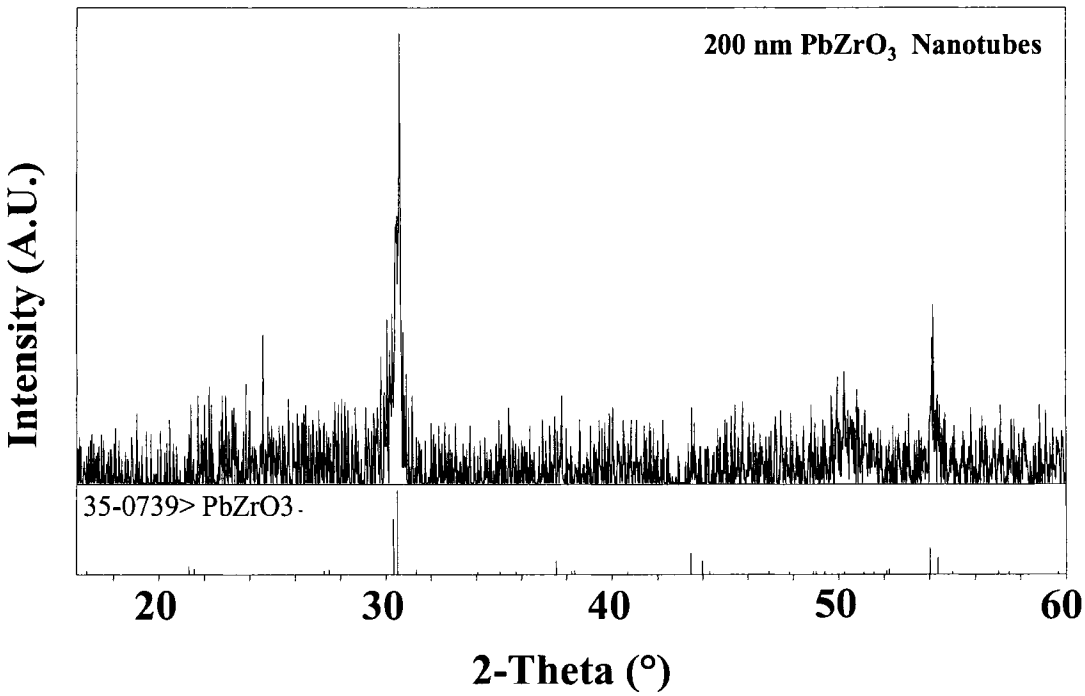

Figure 3.11. PXRD pattern for the $PbZrO_3$ nanotubes indexed to the orthorhombic phase. The average crystallite size to be calculated was 15 nm.

Figure 3.11, was also indexed to the orthorhombic phase and had an average crystallite size of 15 ± 2. Each pattern had line broadening due to the crystallite size effect.

Raman Spectroscopy. The crystalline symmetry of the bulk powder and 200 nm fibers calcined at 650 °C, Figure 3.12, was evaluated at room temperature. The spectrum of the bulk powder calcined at the rate of 50 °C/h up to 650 °C for 6 hours, illustrates the modes of vibration determined for the pure orthorhombic phase of $PbZrO_3$.[55] The peaks have the following assignments: 133, 200, 229, 281, 340, 534, and 668 cm^{-1}. The 200 nm fibers, calcined with the same heating profile, have a mixed-phase spectrum due to the presence of PbO. The low energy $PbZrO_3$ peak found at 134 cm^{-1} has next to it a peak centered at 141 cm^{-1} assigned to PbO, which was not detected by PXRD, Figure 3.10. Small shifts in the $PbZrO_3$ frequency modes have also occurred. Peak assignments for orthorhombic $PbZrO_3$ nanofibers are: 134, 206, 231, 279, 339, and 535 cm^{-1}. The presence of orthorhombic PbO in the Raman spectrum shows that nanofiber's crystallization temperature of 650 °C for 6 hours may need to be elevated because the prsencee of phase separated PbO and ZrO_2. Li et al. showed that powders derived from sol-gel synthesis crystallized from 450-700 °C have strong Raman bands from PbO.[55] Under these reaction conditions, the modes from monoclinic ZrO_3 were only observed at 500 °C.[55] The spectrum of PbO, Figure 3.12c, was obtained from $PbZrO_3$ bulk powders calcined at 650 °C for 15 minutes. Peak assignments for PbO are: 86, 144, 286, 338, and 382 cm^{-1}. Tubes examined by Raman using the Nd:YAG laser did not show any peaks associated with PbO or $PbZrO_3$. Tubes examined by Raman using the argon laser line have not been performed.

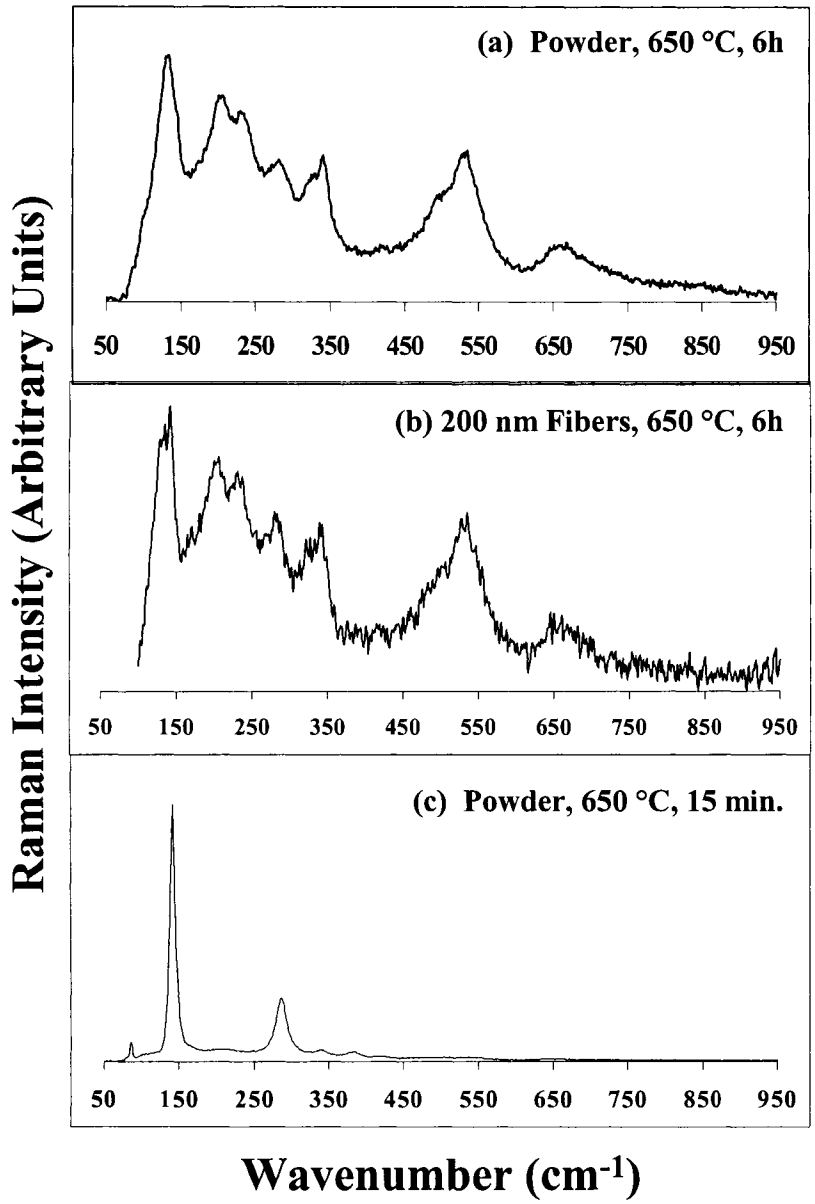

Figure 3.12. Raman spectra of $PbZrO_3$ bulk powders and 200 nm fibers calcined at 650 °C. (a) Orthorhombic modes of vibration for $PbZrO_3$ bulk powder calcined at 50°C/h to 650 °C for 6 h. (b) 200 nm orthorhombic fibers calcined with the same heating profile as the bulk powder (a). Peak at 141 cm^{-1} is due to the presence of PbO. (c) $PbZrO_3$ bulk powders calcined with flash heating. Spectrum illustrates modes of vibration for PbO at at 141 cm^{-1}.

III C. Phase Transformation Behavior of $PbTiO_3$ and $PbZrO_3$ Powders, Tubes and Fibers

The effects of aspect ratio and crystallite size upon the ferroelectric and antiferroelectric phase transition were monitored through differential scanning calorimetry (DSC) which provided an indirect measurement of the polarization.[56] Aspect ratio, which is defined at the average length/diameter for fibers and length/outer diameter for tubes, was 250 for the AAO template, and 200, 100, and 50 for the PC templates used.

Differential Scanning Calorimetery. As a second control, bulk powders that were treated at identical temperatures and conditions as the membrane bound nanotubes were also treated with 6M NaOH, filtered and washed. DSC data showed no difference in T_c or ΔH. Thermal hysteresis and the effects of crystallite size on the ferroelectric phase transition are shown in Figure 3.13 for bulk $PbTiO_3$ powders. Ferroelectric (FE) and antiferroelectric (AF) perovskites undergo displacive transitions that are reversible. The DSC traces, Figure 3.13, show the $PbTiO_3$ tetragonal FE phase being heated, the endotherms resulting from the phase transition to cubic symmetry, and the exotherm for the cubic paraelectric-ferroelctric (PE-FE) transition that occurs when cooled through the Curie temperature. $PbZrO_3$ undergoes a similar displacive transition where the orthorhombic (AF) phase is heated and transitions to the cubic (PE) phase.

Table 3.5 summarizes the FE-PE and AF-PE Curie temperature (Tc_1) that occurs upon heating, its reverse (Tc_2), and their respective ΔH values. Data confirm a decrease in both T_c and ΔH for the bulk samples and nanofibers. As the $PbTiO_3$ crystallite size decreases, the endo- and exotherms become broader and the limitation of DSC is shown. However, when the 29 nm crystallite size does not have a distinct FE-PE T_c upon heating,

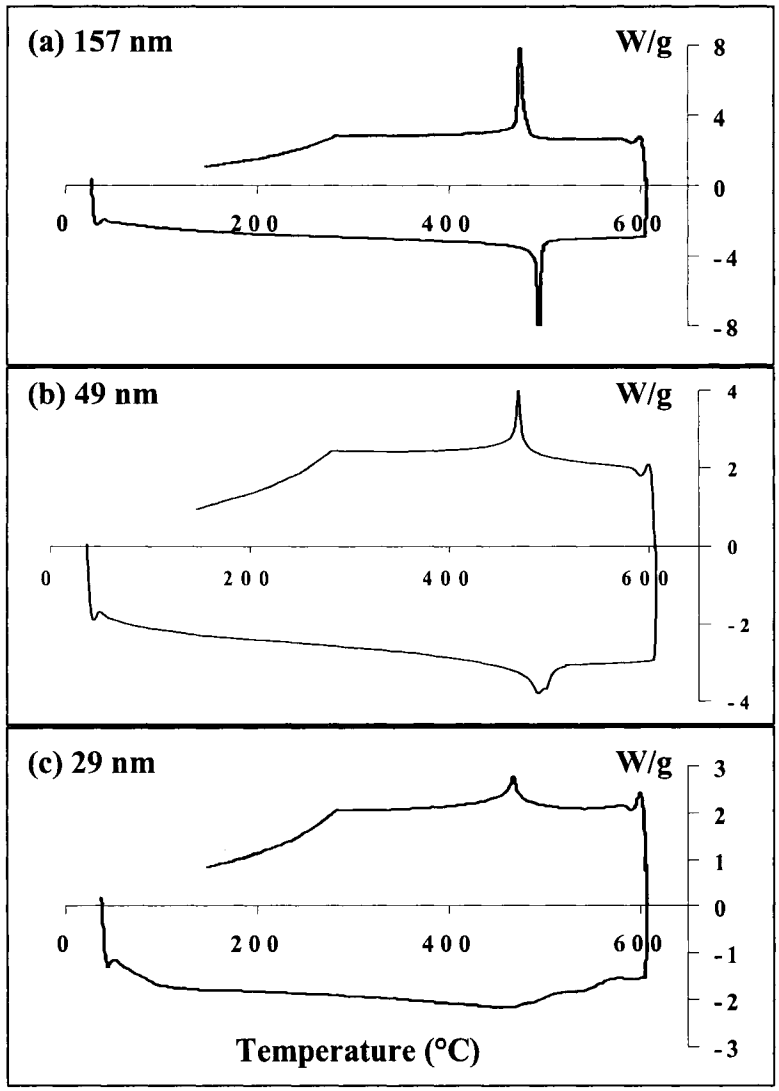

Figure 3.13. DSC scans of bulk $PbTiO_3$ powder with (a) 157, (b) 49, and (c) 29 nm crystallite sizes. The effect of reducing grain and crystallite size upon the Curie transition temperature (T_c), enthalpy of phase transition (ΔH), and the hysteresis of phase behavior is shown.

Table 3.5. Differential Scanning Calorimeter Data for $PbTiO_3$ & $PbZrO_3$ Bulk Powder and Fibers

Material & Processing Temperature	Cryst. Size d_{XRD} (nm)	Aspect Ratio	T_{C1} (°C) FE-PE[a] AF-PE[b]	T_{C2} (°C) PE-FE[a] PE-AF[b]	ΔH_1 (J/g)	ΔH_2 (J/g)
650 °C PT Powder	157	----	494	474	5.1	5.1
550 °C PT Powder	49	----	490	469	2.8	2.0
450 °C PT Powder	29	----	----	468	----	0.86
650 °C 200 nm PT Fibers	73	50	489	470	2.7	1.8
650 °C 100 nm PT Fibers	57	100	490	469	1.6	1.4
650 °C 50 nm PT Fibers	53	200	490	468	2.4	1.5
650 °C PZ Powder	79	---	223	215	1.5	0.75
650 °C 200 nm PZ Fibers	23	50	219	---	1.5	---

[a]Ferroelectric-Paraelectric Transition for $PbTiO_3$
[b]Antiferroelectric-Paraelectric Transition for $PbZrO_3$

the effects of annealing are seen with a discernable PE-FE transition upon cooling. Figure 3.14 displays the representative traces for the 200 nm fibers and the 200 nm tubes made by the template method. DSC thermograms for the 100 and 50 nm $PbTiO_3$ fibers calcined at 650 °C had T_c and ΔH similar to the bulk powders with a 49 nm crystallite size. Cyclic DSC traces for $PbZrO_3$ bulk powders and 200 nm fibers calcined at 650 °C were also performed. The trace for the powder had a small broad endo- and exotherms at Tc_1 = 223 °C and Tc_2 = 215 °C. $PbZrO_3$ 200 nm fibers had a Tc_1 = 219 °C with a similar 4 °C difference observed between the $PbTiO_3$ powders and fibers. Chattopadhay has reported similar T_c values for powder samples with 72 and 32 nm crystallite sizes.[11] The results demonstrated here, indicate that crystallite size, not aspect ratio of the 1-D fibers, contributed to a change in polarization. Examination of the nanotubes showed that the crystallite size was too small to evaluate with DSC.

We previously reported that $PbTiO_3$ nanotubes had a T_c of 234 °C for a sample having a crystallite size of 11 nm and that nanotubes of $PbZrO_3$ and PZT had similar deviations from the bulk phase transition temperature.[57] Upon further examination, it was determined that only endotherms ranging from about 123-266 °C were observed upon heating with no reverse exotherms as seen in Figure 3.14b for the materials made with the AAO template. Therefore, it was not reasonable to assign this endotherm as a ferroelectric phase transition. A second cyclic DSC scan on the same sample of $PbTiO_3$ nanotubes used in Figure 3.14b was performed to see if the heat treatment had an annealing effect on the crystals that would allow for a transition to be monitored by DSC. The results showed no indication of thermal hysteresis associated with displacive phase transformation as seen with our bulk powder and nanofibers.

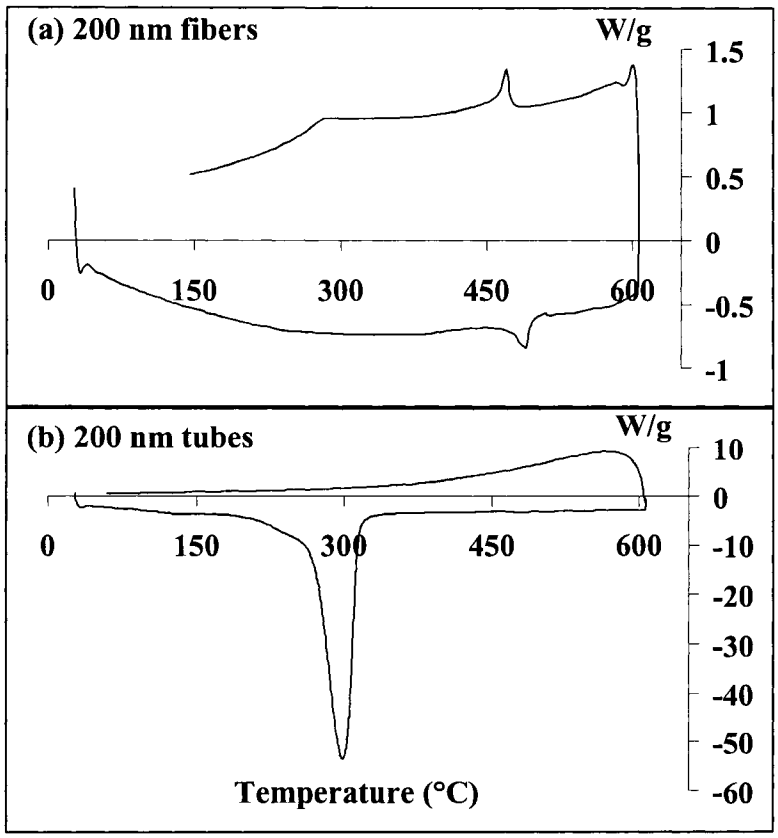

Figure 3.14. DSC traces of the 200 nm $PbTiO_3$ (a) fibers and (b) tubes calcined at 650°C. Thermal hysteresis of phase change is only observed in the fibers.

Performing the cyclic DSC scan within the temperature range of 493 °C for the $PbTiO_3$ nanotubes and observing no annealing effects may invalidate the first assumption - the surface film caused the tetragonal lattice modes to be observed during the Raman experiment. PXRD analysis confirmed that the surface film had an average crystallite size of 30 nm. The DSC trace of the bulk powders with an average crystallite size of 29 nm indicated that annealing effects took place and displayed an exotherm attributable to the PE-FE transition. If these nanotube samples contained a large fraction of the 30 nm crystallites from the surface film, these crystals would have been detected during the DSC analysis.

Thermogravametric Analysis and Mass Spectrometry. TGA results are shown in Figure 3.15a for the $PbTiO_3$ nanotubes calcined at 650 °C, removed from the AAO template with NaOH, rinsed, and dried in an oven at 100 °C overnight. A weight loss of ~20% was observed around 234 °C. The mass spectrum, Figure 3.15b, contained peaks for H_2O (m/z = 18) and OH (m/z = 17). The process for removing the AAO template and the capillary action of the nanotubes allowed water to be stored within them despite extensive drying. This resulted in the observation of endotherms in the DSC to occur between 120-266 °C. The temperature ranges for water evaporation from the tubes were associated with the amount of time they had contact with water. The TGA results indicated that nanotube structures may offer unique storage capabilities for water and other materials.

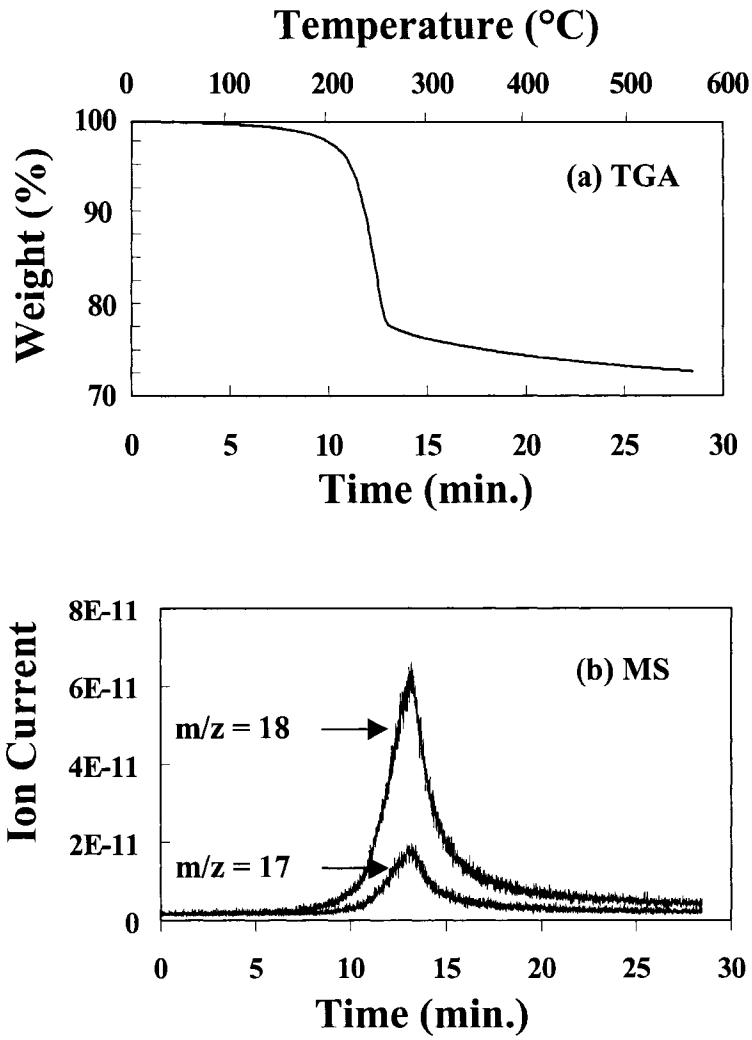

Figure 3.15. (a) Thermogravametric analysis of the tubes calcined at 650 °C show that a weight loss of 20% occurred over the temperature range for the endotherm observed in the DSC analysis. (b) Mass spectrometry of the weight loss, as a function of time, shows water (m/z = 18) as the source of the endotherm.

Understanding how the phase transition temperature (T_c) and enthalpy of transition (ΔH) are influenced by particle size could explain how the spontaneous polarization is affected. According to Equation 3.1,[56]

$$(\Delta H) = 2\pi P^2 T_c / C \qquad (3.1)$$

ΔH is related to the polarization (P), the Curie-Weiss constant (C), and the transition temperature (T_c). From Equation 3.1, it can be seen that a decrease of P and T_c will lead to a decrease in ΔH. This equation is based on using a spherical nanoparticle model, although our structures are not spherical, the polycrystalline grains that comprise the structures could be approximated to a sphere. One explanation for the effects of depolarization have been discussed in terms of a randomly oriented surface charge layer that begins to take precedence over the highly ordered ferroelectric interior as the size of a particle becomes smaller.[56] Eventually, the particle will reach a critical size where polarization becomes zero due to the removal of the ferroelectric core. Using Landau-Devonshire theory, Wang et al. were able to explain this phenomenon and predicted a critical size of 4.2 nm for $PbTiO_3$ particles.[18] This size is smaller than Ishikawa's experimental value of 13.8 nm observed while monitoring T_c by Raman scattering and Akdogan's extrapolated value of 15 nm by XRD.[9,13] It should be noted, however, that in all the reported transition temperatures for sol-gel derived $PbTiO_3$ nanocrystals using DSC, no T_c was reported below 400°C.[10,11,34]

In determining the effects of hydrostatic pressures and temperature on dielectric constants, Samara showed that a single crystal of $PbTiO_3$ had a T_c = 323 °C when placed under ~2.4 GPa. Fu and co-workers have reported a T_c below 400 °C with nanoparticles; however, this was demonstrated through an in situ Raman temperature experiment

wherein crystals with an average size of 7 nm began to show peaks associated with tetragonal symmetry at a T_c of 166 °C.[12] At this temperature, the authors suggested that the 7 nm nanocrystals underwent a phase transition from orthorhombic to tetragonal which implies that a stable orthorhombic phase existed before reaching tetragonal symmetry. The orthorhombic-tetragonal phase transition is never seen in the $PbTiO_3$ system; however, evidence of such behavior has been seen in the $BaTiO_3$ system. Frey's work on submicron $BaTiO_3$ particles showed evidence of Raman active modes arising from orthorhombic symmetry before reaching the tetragonal phase as a function of grain size.[7] The experiments reported in this chapter with the nanotubes showed that measurement of crystallite sizes of perovskites smaller than 20 nm may require scanning probe techniques or in situ Raman temperature experiments to correctly evaluate the polarization of the material and phase transition.

IV. Summary

The sol-gel template synthesis method has been used to fabricate one-dimensional perovskite materials and experiments have shown they are useful models for the investigation of size effects on aspect ratio and dimensionality on ferroelectricity and antiferroelectricity. $PbTiO_3$ and $PbZrO_3$ nanotubes and fibers, made within AAO and PC membranes, were used to study the effects of crystallite size on both lattice structure and polarization. Comparisons between a control group of bulk powders, tubes, and fibers were made. It was found that tetragonality (c/a) and phase transition temperatures (T_c) of $PbTiO_3$ polycrystalline models for fibers and powders deviated from the single crystal data, but were similar to each other based on crystallite size. The crystallite size of the

nanotubes may have hindered the ability to indirectly measure polarization with DSC. Results from DSC measurements indicate that crystallite size, nor aspect ratio play a significant role on the polarizability of the perovskites anlayzed. It was also found serendipitously that nanotube structures are useful in the storage of liquids such as H_2O. Finally, our analysis of the E(1TO) soft mode frequency of $PbTiO_3$ also showed that the crystallites in our structures were not under the hydrostatic pressures of 1-2 GPa that have previously been reported. Thus confirming that surface tension considerations in size effects may be less important, and that the local structure of the Ti^{4+} and the ferroelectric particle core more relevant in determining a mechanism for size effects with pervoskite materials.

References

(1) Patzke, G.; Krumeich, F.; Nesper, R., *Angew. Chem., Int. Ed. Engl.* **2003,** 41, 2446-2461.

(2) Rao, C. N. R.; Nath, M., *Dalton Trans.* **2003,** 1, 1-24.

(3) Rao, C. N. R.; Deepak, F. L.; Gundiah, G.; Govindaraj, A., *Prog. Solid State Chem.* **2003,** 31, 5-147.

(4) Xia, Y.; Yang, P.; Sun, Y.; Wu, Y.; Mayers, B.; Gates, B.; Yin, Y.; Kim, F.; Yan, H., *Adv. Mater.* **2003,** 15, 353-388.

(5) Hernandez, B. A.; Chang, K.-S.; Fisher, E. R.; Dorhout, P. K., *Chem. Mater.* **2002,** 14, 480-482.

(6) Akdogan, E. K.; Leonard, M. R.; Safari, A., Size Effects in Ferroelectric Ceramics. In *Handbook of Low and High Dielectric Constant Materials and Their Applications*, Academic Press: **1999**; pp 61-112.

(7) Frey, M. H.; Payne, D. A., *Phys. Rev. B.* **1996,** 54, 3158-3168.

(8) Akdogan, E. K.; Mayo, W.; Safri, A.; Rawn, C. J.; Payzant, E. A., *Ferroelectrics* **1999,** 223, 11-18.

(9) Akdogan, E. K.; Safari, A. In *Size Effects in Nanophase $PbTiO_3$*, 2000 12th IEEE Interanational Symposium on Applications of Ferroelectrics, Honolulu, Hawaii, U.S. A., 2000; 'Eds.' Honolulu, Hawaii, U.S. A., 2000; pp 487-490.

(10) Baodong, Q.; Bin, J.; Yuguo, W.; Peilin, Z.; Weilie, Z., *Chin. Phys. Lett.* **1994,** 11, 514-517.

(11) Chattopadhyay, S., *Nanostruc. Mater.* **1997,** 9, 551-554.

(12) Fu, D.; Suzuki, H.; Ishikawa, K., *Phys. Rev. B.* **2000,** 62, 3125-3129.

(13) Ishikawa, K.; Yoshikawa, K.; Okada, N., *Phys. Rev. B.* **1988,** 37, 5852-5855.

(14) Jiang, B.; Peng, J. L.; Bursill, L. A.; Zhong, W. L., *J. Appl. Phys.* **2000,** 87, 3462-3467.

(15) Ma, W.; Zhang, M.; Lu, Z., *Phys. Status Solidi A* **1988,** 166, 811-815.

(16) Pandey, D.; Singh, N.; Mishra, S. K., *Indian J. Pure Appl. Phys.* **1994,** 32, 616-623.

(17) Pramanik, P.; Das, R. N., *Mater. Sci and Eng.* **2001,** A304-306, 775-779.

(18) Wang, Y. G.; Zhong, W. L.; Zhang, P. L., *Soild State Commun.* **1994,** 90, 329-332.

(19) Zhong, W. L.; Jiang, B.; Zhang, P. L.; Ma, J. M.; Cheng, H. M.; Yang, Z. H.; Li, L. X., *J. Phys.: Condens. Matter* **1993,** 5, 2619-2624.

(20) Zhou, Q. F.; Zhang, J. X.; Chan, H. L. W.; Choy, C. L., *Ferroelectrics* **1997,** 195, 221-214.

(21) Limmer, S. J.; Cao, G., *Adv. Mater.* **2003,** 15, 427-431.

(22) Limmer, S. J.; Hubler, T. L.; Cao, G., *J. Sol-Gel Sci. Tech.* **2003,** 26, 577-581.

(23) Limmer, S. J.; Seraji, S.; Forbess, M. J.; Wu, Y.; Chou, T. P.; Nguyen, C.; Cao, G., *Adv. Mater.* **2001,** 13, 1269-1272.

(24) Limmer, S. J.; Seraji, S.; Wu, Y.; Chou, T. P.; Nguyen, C.; Cao, G., *Adv. Funct. Mater.* **2002,** 12, 59-64.

(25) Urban, J.; Yun, W. S.; Gu, Q.; Park, H., *J. Am. Chem. Soc.* **2002,** 124, 1186-1187.

(26) Yun, W. S.; Urban, J. J.; Gu, Q.; Park, H., *Nano Letters* **2002,** 2, 447-450.

(27) Schaak, R. E.; Mallouk, T., *Chem. Mater.* **2000,** 12, 3427-3434.

(28) Mao, Y.; Banerjee, S.; Wong, S. S., *Chem. Commun.* **2003**, 408-409.

(29) Akdogan, E. K.; Safri, A., *Jpn. J. Appl. Phys.* **2002,** 41, 7170-7175.

(30) Li, S.; Sr., C., R. A.; Spriggs, R. M., *Spectrosc. Lett.* **1988,** 21, 969-.

(31) Blum, J. B., *Mater. Lett.* **1985,** 3, 360-362.

(32) Boyle, T. J.; Dimos, D.; Schwartz, R. W.; Alam, T. M.; Sinclair, M. B.; Buchheit, C. D., *J. Mater. Res.* **1997,** 12, 1022-1030.

(33) Doeuff, S.; Dromzee, Y.; Taulelle, F.; Sanchez, C., *Inorg. Chem* **1989,** 28, 4439-4445.

(34) Chattopadhyay, S.; Ayyub, P.; Palkar, V. R.; Multani, M., *Phys. Rev. B.* **1995,** 52, 13177-13183.

(35) O'Brien, S.; Brus, L.; Murray, C. B., *J. Am. Chem. Soc.* **2001,** 123, 12085-12086.

(36) Schwartz, R. W., *Chem. Mater.* **1997,** 9, 2325-2340.

(37) Shih, W. Y.; Shih, W.-H.; Akasay, I. A., *Phys. Rev. B: Condens. Matter* **1994,** 20, 15575-15585.

(38) Yu, D. S.; Han, J. C.; Ba, L., *Am. Cer. Soc. Bull.* **2002,** 81, 38-39.

(39) Zhang, Q.; Whatmore, R.; Vickers, M. E., *J. Sol-Gel Sci. Technol.* **1999,** 15, 13-22.

(40) Lakshmi, B. B.; Patrissi, C. J.; Martin, C. R., *Chem. Mater.* **1997,** 9, 2544-2550.

(41) Klug, H. P.; Alexander, L. E., *X-ray Diffraction Procedures For Polycrystalline and Amorphous Materials*. 2nd ed.; John Willey & Sons: New York, **1974**.

(42) Cullity, B. D., *Elements of X-Ray Diffraction.*; Addison-Wesly: Massachusetts, **1978**.

(43) Pena, M. A.; Fierro, J. L. G., *Chem. Rev.* **2001,** 101, 1981-2017.

(44) PDF # 40-0099

(45) Burns, G.; Scott, B. A., *Phys. Rev. Lett.* **1970,** 25, 167-170.

(46) Burns, G.; Scott, B. A., *Phys. Rev. B.* **1973,** 7, 3088-3101.

(47) Fately, W. G.; Dollish, F. R.; McDevitt, N. T.; Bently, F. F., *Infared and Raman Selection Rules For Molecular and Lattice Vibrations*.; Wiley-Interscience: New York, **1972**.

(48) Frey, R. A.; Siberman, E., *Helv. Phys. Acta* **1976,** 49, 1.

(49) Ishikawa, K.; Yoshikawa, K.; Okada, N., *Phys. Rev. B* **1988,** 37, 5852.

(50) Sanjurjo, J. A.; Lopez-Cruz, E.; Burns, G., *Phys. Rev. B* **1983,** 28, 7260-7268.

(51) Fu, D. S.; Iwadaki, H.; Ishikawa, K., *J. Phys.: Condens. Matter* **2000,** 12, 399-414.

(52) Chattopadhyay, S.; Ayyub, P.; Palkar, V. R.; Gurjar, A. V.; Wankar, R. M.; Multani, M., *J. Phys.: Condens. Matter* **1997,** 9, 8135-8145.

(53) Mishra, S. K.; Pandey, D., *J. Phys.: Condens. Matter* **1995,** 7, 9287-9303.

(54) *PDF # 35-0739.*

(55) Li, S.; A., C. R.; Jang, S. D.; Spriggs, R. M., *J. Mater. Sci.* **1989,** 24, 3873-3877.

(56) Asiaie, R.; Zhu, W.; Akbar, S. A.; Dutta, P. K., *Chem. Mater.* **1996,** 8, 226-234.

(57) Chang, K.-S.; Hernandez, B. A.; Fisher, E. R.; Dorhout, P. K., *J. Korean Chem. Soc.* **2002,** 46, 242-251.

CHAPTER 4

Examination of the Optical Properties for Template Synthesized One-Dimensional Ferroelectric $BaTiO_3$ and Paraelectric $SrTiO_3$

I. Introduction:

$BaTiO_3$ and $SrTiO_3$ belong to the alkaline earth perovskites and are known for their high dielectric constants, semiconducting, and opto-electronic properties.[1,2] In addition, $BaTiO_3$ is well known for its ferroelectricity, whereas, $SrTiO_3$ is described as a a quantum paraelectric material.[3,4] A quantum paraelectric is defined as a material where quantum fluctuations prevents the stability of the ferroelectric phase as the crystal symmetry changes from cubic to tetragonal.[5] The effects of size on quantum paraelectricity, using sol-gel derived $SrTiO_3$ powders with 12-40 nm crystallite sizes, have shown similar deviations in Raman soft mode frequencies as those reported for $PbTiO_3$ in Chapter 3. Investigations on the $BaTiO_3$ ferroelectric size effects have been extensively studied and discussed in Chapters 1 and 3.[6] Most recently, the effects of size on the semiconducting properties and room temperature photoluminescence (PL) have been examined for the perovskite materials.[2,7-9] These reports demonstrated a decrease in band gap energy and increased PL intensity as grain and crystallinity of the perovskites were reduced. Single crystals of the perovskites typically have weak PL at cryogenic temperatures.[10] Here, the methodology developed in Chapter 2 was evaluated for the fabrication of one-dimensional $SrTiO_3$ and $BaTiO_3$ for the investigations on size effects of optical properties.

Chapter 3 demonstrated that the templates had an effect on the morphology of the nanostructures. The polycarbonate (PC) template promoted the growth of $PbTiO_3$ fibers, comprising a morphology resembling a string of grains, resulting from the complete filling of the nanopore channels and a slow heating procedure, whereas nanotubes were formed from the incomplete filing of the anodized aluminum oxide (AAO) nanochannels.

The concentration of sol used to produce these two morphologies was 0.8 M. In this chapter, the effects of each template on the morphologies and symmetries of $BaTiO_3$ and $SrTiO_3$ nanostructures made from varying concentrations of chelate sol (0.5-0.8), the effect of crystallization temperature on grain growth, the influence of crystallite size, and aspect ratio of the templates are presented. Finally, the implications of grain/crystallite size on the electronic properties of the 1-D perovskites will be discussed.

II. Experimental Method

The $BaTiO_3$ and $SrTiO_3$ perovskite nanotubes, fibers, and bulk powders were prepared from chelate sol-gels described in Chapter 2. Because of the esterification pathways of the chelate sol and its effect on microstructure, only fresh sols were used to fabricate tubes and fibers.[11,12] AAO and PC templated nanostructures were calcined in air at a rate of 50 °C/hour to 650 °C for 6 hours before being slowly cooled to room temperature at a rate of 30 °C/hour. A second set of PC templated nanostructures was calcined to 1000 °C using the same heating method. The remaining unused sol was allowed to gel and was calcined using the same heating procedures to produce "bulk" powders used as the control sample.

III. Results and Discussion

Morphologies and Microstructures of $BaTiO_3$ and $SrTiO_3$ Bulk Powders, Nanotubes, and Nanofibers. Electron micrographs, Figures 4.1 and 4.2, illustrate the resulting grain sizes and morphologies obtained from two different concentrations of

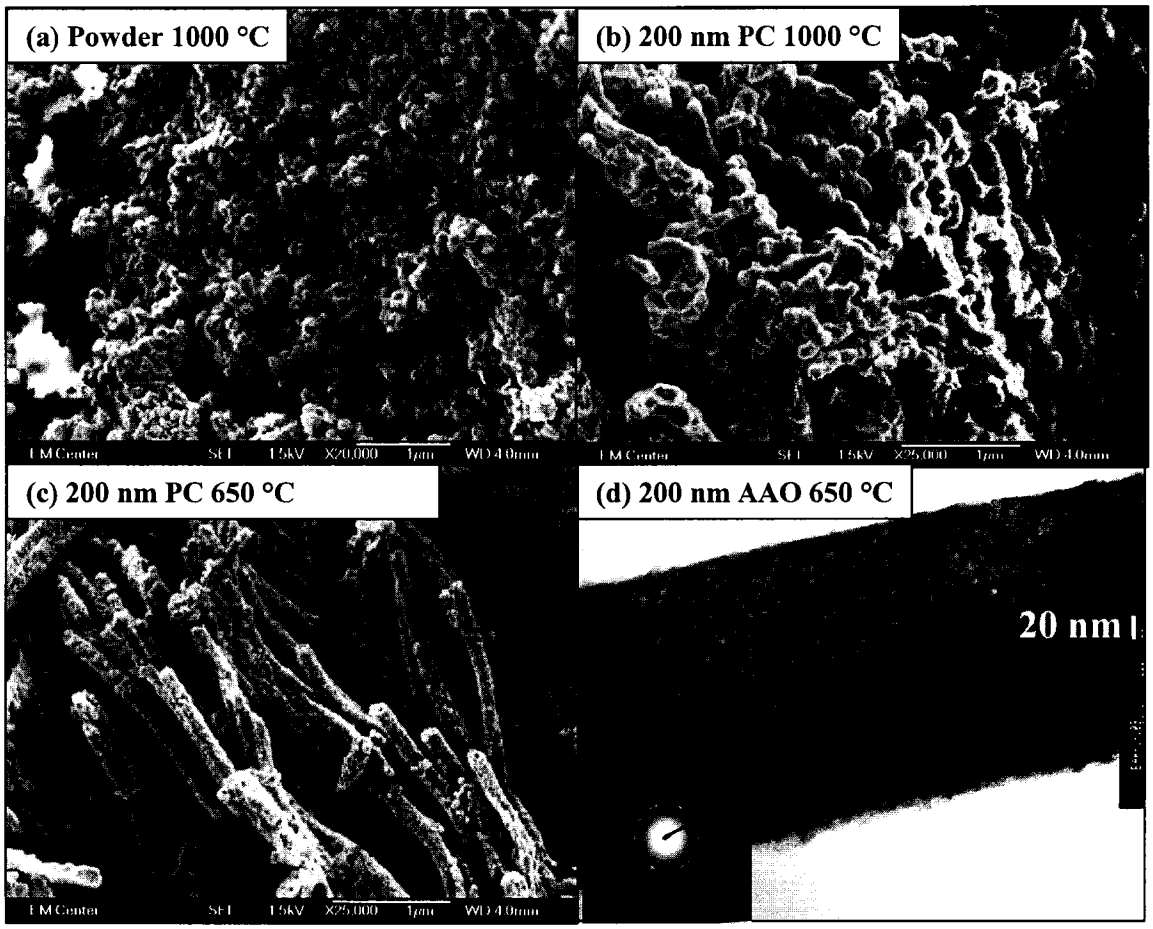

Figure 4.1. A comparison of grain sizes found between $BaTiO_3$ powders, nanofibers, and nanotubes synthesized from a 0.8 M chelate precursor sol-gel. SEM images of (a) bulk powder calcined at 1000 °C (b) 200 nm fibers and calcined at 1000 °C, (c) 200 nm fibers formed in a PC template calcined at 650 °C. TEM image (d) of a single $BaTiO_3$ tube formed in an AAO template and calcined at 650 °C. Inset is the SAD pattern for the nanotube indicating the small grains are polycrystalline.

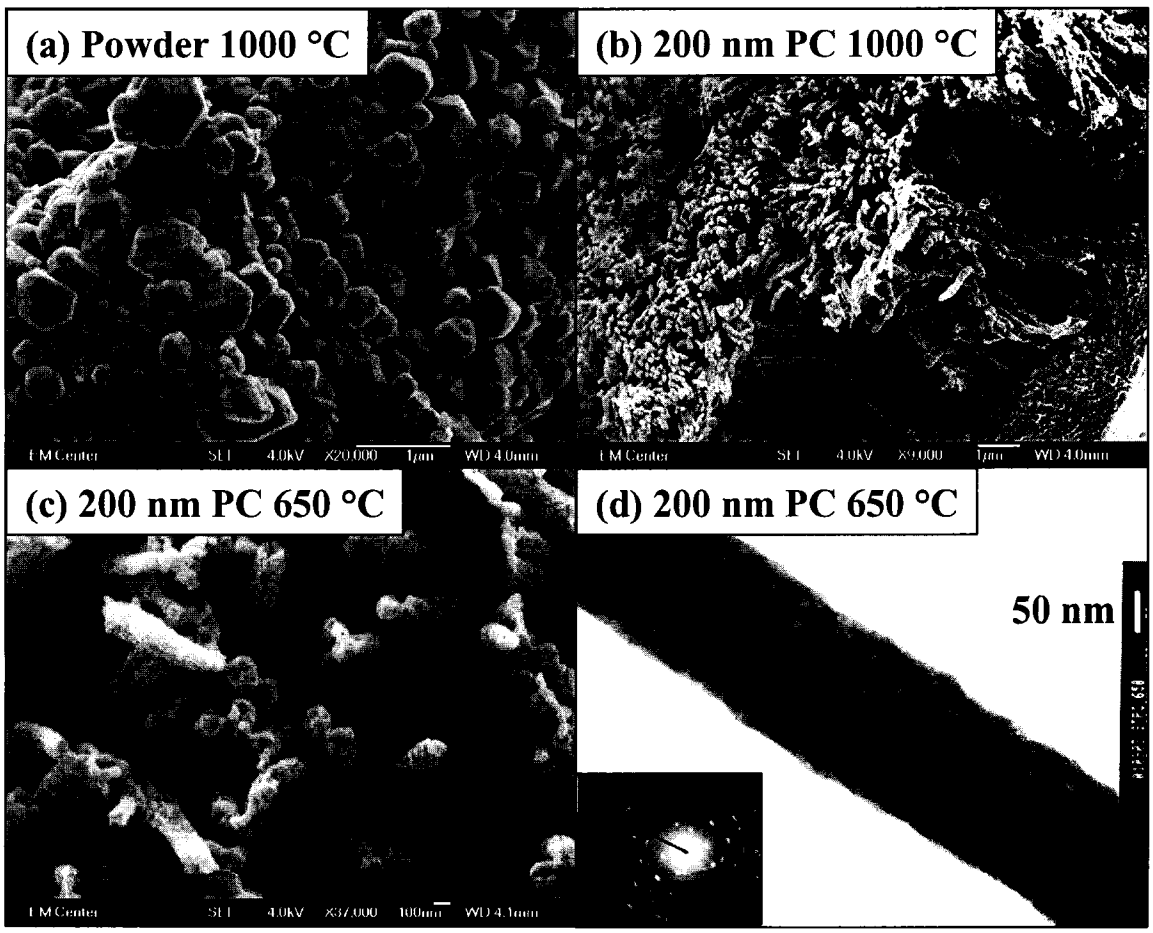

Figure 4.2 A comparison of grain sizes found between $SrTiO_3$ powders, nanofibers, and nanotubes synthesized from a 0.5 M chelate precursor sol-gel. SEM images of (a) bulk powder calcined at 1000 °C (b) 200 nm fibers formed in a PC template and calcined at 1000 °C, (c) 200 nm tubes formed in a PC template calcined at 650 °C. TEM image (d) of a single $SrTiO_3$ tube formed in a PC template and calcined at 650 °C. Inset is the SAD pattern for the nanotube indicates the small grains are polycrystalline.

precursor sol-gel and the heating conditions used to synthesize $BaTiO_3$ and $SrTiO_3$ perovskites.

0.8 M $BaTiO_3$. The SEM image of $BaTiO_3$ bulk powder, Figure 4.1a, calcined at 1000 °C had an average grain size of ~0.3 μm. Bulk powder calcined at 650 °C, not shown, had a grain size of ~0.1 μm. SEM images, Figures 4.1b and 4.1c, reveal two different resulting morphologies for the $BaTiO_3$ nanofibers synthesized in 200 nm PC templates and calcined at 650° and 1000 °C. The string-of-grains morphology, found with PC-templated $PbTiO_3$ calcined at 650 °C, was observed with $BaTiO_3$ fibers calcined at 1000 °C, Figure 4.1b. In contrast, nanofibers similar to those reported by Limmer et al. were observed for $BaTiO_3$ calcined at 650 °C, Figure 4.1c.[13] The two morphologies obtained from our unique heating procedure were the result of different grain sizes that comprised the fibers. Using SEM analysis, fibers calcined at 1000 °C had grain sizes that were ~200 nm in diameter but varied in length along the template channel. Fibers formed at 650 °C had grains 70-100 nm in diameter. The length of the fibers calcined at each temperature was ~6 μm. Smaller diameters of 180-190 nm were found close to the tips of the fibers calcinied at 650 °C, and 200 nm diameters were found at the base of these same fibers. Overall, the dimensions of the PC template were kept within the calcination range of 650°-1000 °C. Arrays of these fibers were typically attached to 1-2 μm thick films. The 0.8 M sol was also applied to the AAO template and calcined at 650 °C. The TEM image, Figure 4.1d, illustrated that only nanotubes were produced from the AAO template. The $BaTiO_3$ nanotubes that formed from the AAO template comprised grains < 20 nm. TEM images of $SrTiO_3$ nanotubes prepared in AAO using a 0.5 M sol were similar to Figure 4.1d.

0.5 M $SrTiO_3$. In contrast to $BaTiO_3$ bulk powders calcined at 1000 °C, the SEM image of $SrTiO_3$, Figure 4.2a, had a grain size distribution of 0.3-1.0 μm. Grain size analysis was not performed on powder calcined at 650 °C because it was identified as a mixed-phase of $SrCO_3$ and $SrTiO_3$ through PXRD. Powder diffraction data will be discussed in the next section. The effect of decreasing the sol-gel precursor concentration was monitored with SEM and TEM. Two different morphologies were observed from the synthesis with 0.5 M sols and 200 nm PC templates, as was observed for experiments at 0.8 M. Nanostructures prepared from these conditions, however, revealed the formation of nanotubes and nanofibers calcined at 650° and 1000 °C, respectively. The SEM image of fibers calcined at 1000 °C, Figure 4.2b, revealed the string-of-grains morphology with an average grain size of ~200 nm in diameter. When the calcination temperature was lowered to 650 °C, the morphology identified by SEM was nanotubes, Figure 4.2c. The image shows the open ends of the tubes. A few capped structures were also observed. The TEM image of a single tube formed from the PC template, Figure 4.2d, illustrates that the fiber was ~170 nm in diameter and comprise polycrystalline grains < 50 nm. Analysis on the fibers with SEM and TEM reveal a distribution of fiber diameters of 170-200 nm, similar to the $BaTiO_3$ fibers calcined at 650 °C. These experiments demonstrated that the formation of a tube structures could be achieved in a PC template.

The explanation for fiber versus tube formation, given in Chapter 3 for 0.8 M solutions, was attributed to the difference in the length of the nanochannels within the templates. Production of a fiber from tube morphology is a result of complete versus incomplete filling of the nanochannels within the template.[14-17] During the coating

process, sol entered the channels through capillary action. Each template used had hydrophilic surfaces and uptake of a polar solution should have easily occurred. As the 0.8 M solution entered the 200 nm channels of different lengths (~50 μm for AAO and ~10 μm for PC) incomplete filling or coating of the AAO template for the longer channel may have resulted while complete filling was observed in the PC channel. In effect, the shorter channel length allowed for more solution to enter. Therefore, to form nanotubes with PC templates, the less material forming within the sol was needed. The 0.5 M and lower concentration precursor sol-gels should produce tube morphologies in PC templates when calcined at the lowest crystallization temperature required to synthesize single-phase materials and prevent large grain growth.

In addition to substrate effects, the morphology differences between the string of grain fibers, fibers with small grain sizes, and tubes with small grains result from annealing effects. Templates and the calcination temperature helped control the grain sizes of the tubes and fibers. All perovskite nanotubes synthesized in AAO templates, by our method, typically had grain sizes < 20 nm. This inorganic substrate and the incomplete filling of the template helped control grain size for samples calcined at 650 °C. Experiments with the PC templates demonstrated that the effects of annealing which promoted different grain sizes could change the morphology of the perovskite fibers and affect the formation of tubes versus fibers.

Evaluating Room-Temperature Lattice Structure of $BaTiO_3$ and $SrTiO_3$ Powders, Tubes and Fibers. The average room-temperature crystal structures were evaluated with PXRD. Lattice parameters and average crystallite sizes calculated from the PXRD data, Figures 4.3-4.6, are summarized for $BaTiO_3$ and $SrTiO_3$ in Table 4.1.

Table 4.1. Cell Parameters and Crystallite Size For $BaTiO_3$ and $SrTiO_3$

Material & **Processing Temp.**	**a (Å)**	**c (Å)**	**V ($Å^3$)**	**c/a**	**Crystallite Size (nm)[a]**
BT Reference 18	4.031	----	65.5	----	----
BT Reference 19	3.994	4.038	64.4	1.011	----
BT Powder 1000 °C	3.983(1)	4.032(3)	64.0	1.012	59 ± 6
BT Powder 650 °C	4.011(1)	----	64.6	----	26 ± 2
BT 200 nm PC fibers 650 °C	3.992(2)	4.002(7)	63.8	1.003	28 ± 3
BT 200 nm PC fibers 1000 °C	3.995(1)	4.004(2)	63.9	1.003	34 ± 3
BT 200 nm AAO tubes 650 °C	4.032	----	65.5	----	13 ± 2
ST Reference 39	3.905	----	59.6	----	----
ST Powder 1000 °C	3.889(2)	----	58.8	----	97 ± 10
ST 200 nm fibers 1000 °C	3.887(3)	----	58.7	----	35 ± 4
ST 200 nm fibers 650 °C	3.889(1)	----	58.81	----	27 ± 3
200 nm AAO tubes 650 °C	3.890(4)	----	58.86	----	17 ± 2

[a]Crystallite size calculated from the (111) reflection of $BaTiO_3$ and the (110) reflection of $SrTiO_3$

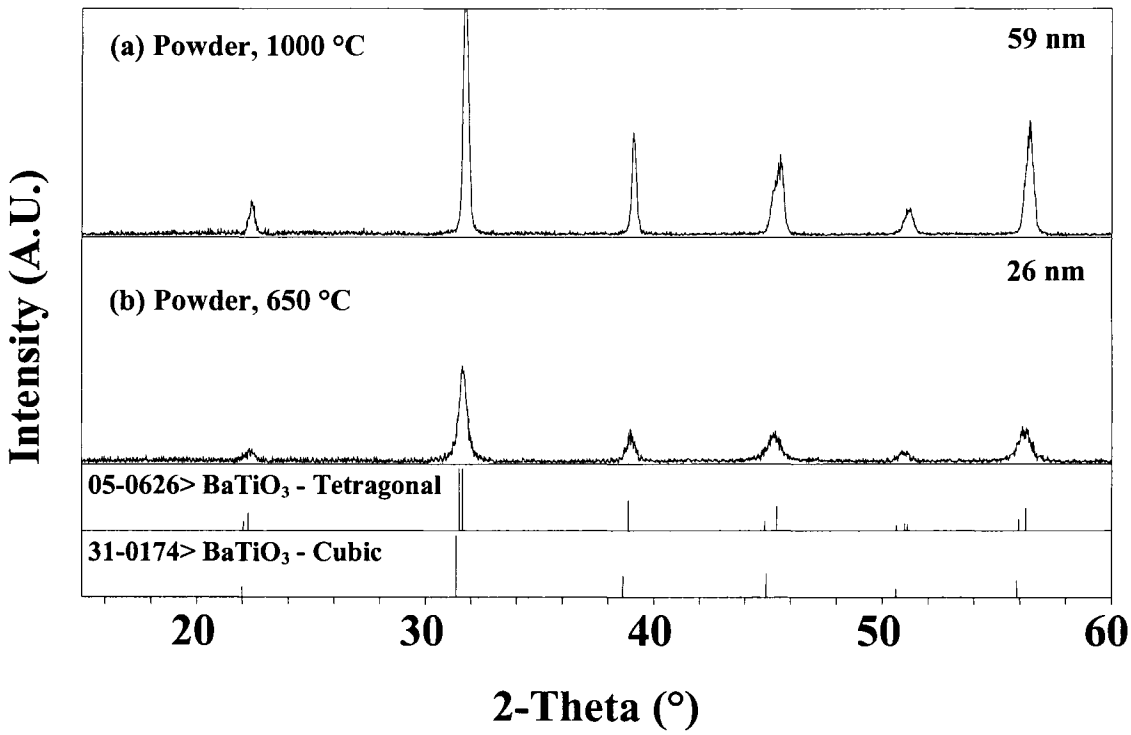

Figure 4.3. PXRD Patterns for $BaTiO_3$ bulk powders calcined at (a) 1000 °C and (b) 650 °C. The (111) reflection was used to calculate an average crystallite size of 59 and 26, respectively. Due to the crystallite size, peak broadening occurs and both patterns are indexed to have the cubic phase.

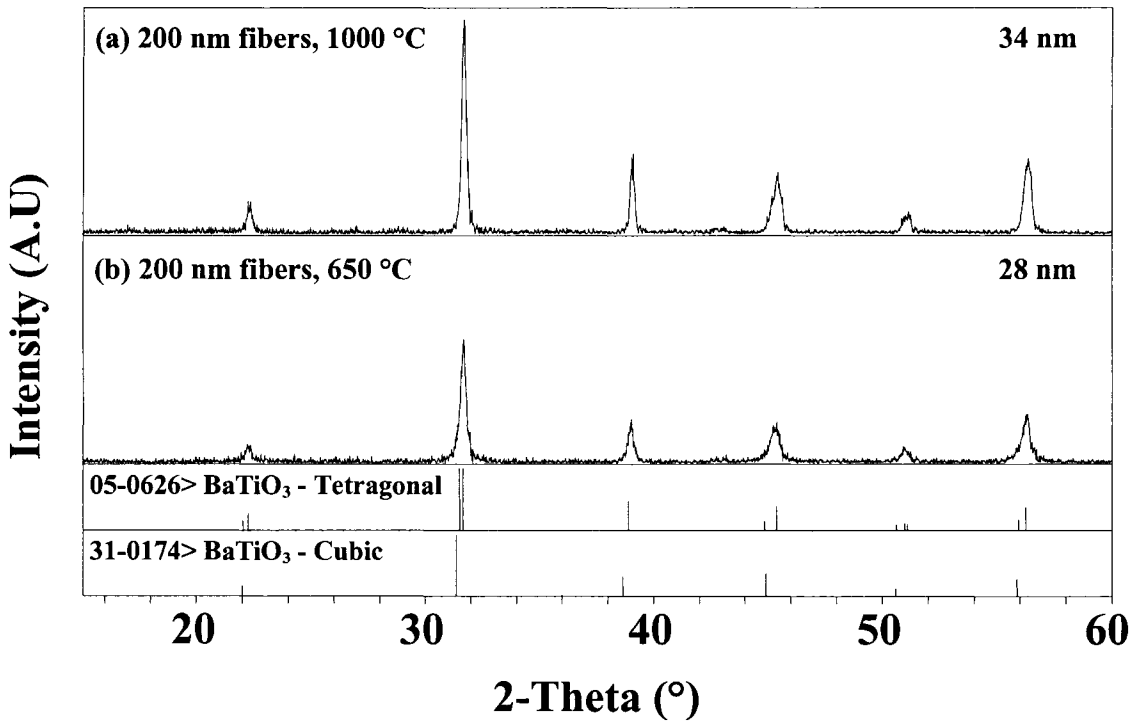

Figure 4.4. PXRD patterns of $BaTiO_3$ nanofibers formed within 200 nm PC templates and heated at (a) 1000 °C and (b) 650 °C for 6 h. Both samples have been assigned to the psuedocubic phase and an average crystallite size of 34 and 28 nm were calculated for the respective calcination temperatures.

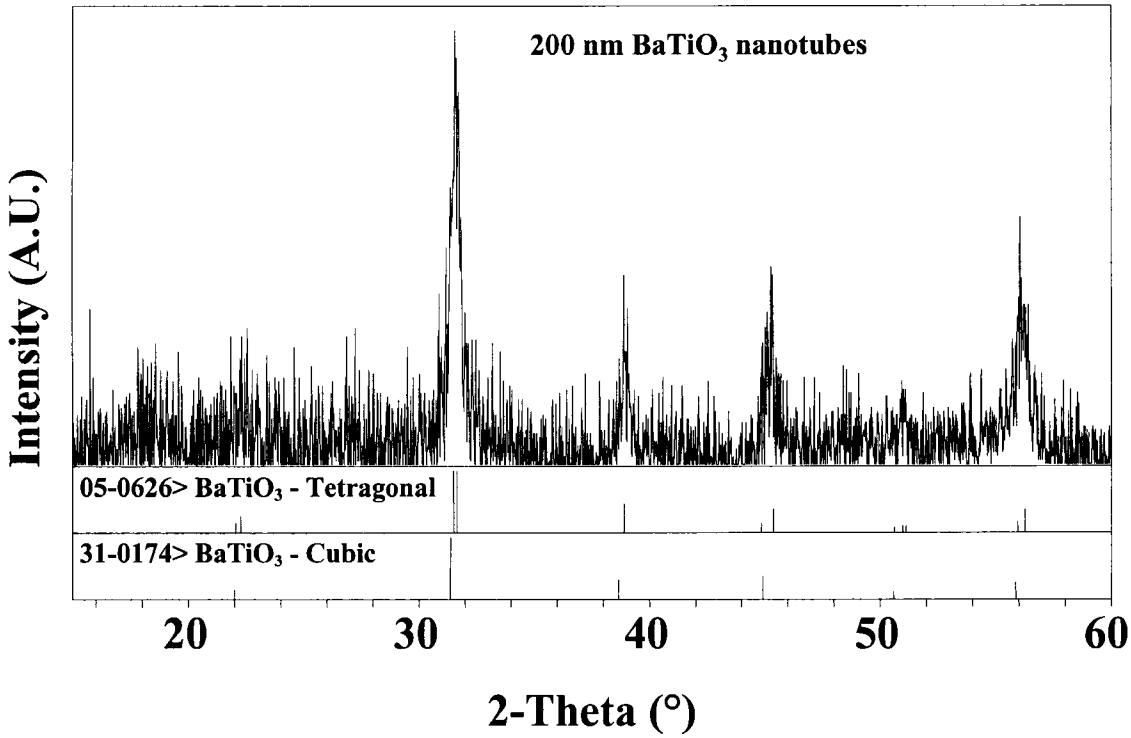

Figure 4.5. PXRD pattern for $BaTiO_3$ nanotubes formed within the AAO template and calcined at 650 °C for 6 h. Tubes were assigned to the cubic phase of $BaTiO_3$ and have an average crystallite size of 13 nm.

III A. Examination of 1-D Ferroelectric $BaTiO_3$ Materials

Powder X-ray Diffraction of $BaTiO_3$. Bulk powders were calcined at 650° and 1000 °C and their respective powder patterns, Figure 4.3, illustrate the effects of crystallite size on the relative intensity and broadening of the peaks. Both patterns had peak positions in good agreement with the tetragonal unit cell and space group P4mm (99).[18] Due to the crystallite size of the powders, broadening was observed and the patterns appeared best indexed as the cubic (Pm3m) symmetry. [18-21] The tetragonal phase of $BaTiO_3$ is often identified by the characteristic peak separation of the (200) into the (200) and (002) reflections near $2\theta = 45°$.[2,22-24] The peak separation results from the introduction of new plane spacings, caused by a non-uniform distortion between the a- and c- unit cell parameters.[21] In contrast to $PbTiO_3$, the relative difference between the c- and a- axes is only 1%, which is often not observable in PXRD experiments on small crystallites.[25] Nevertheless, the room temperature transition from cubic to tetragonal symmetry can be observed by PXRD for $BaTiO_3$ synthesized by the sol-gel process and calcined between 1000 ° and 1350 °C through the gradual separation of the (200) peak.[26] Peak analysis and cell refinement was performed to identify the symmetry and unit cell parameters of the two powders. $BaTiO_3$ powders calcined at 650° and 1000°C were determined to be cubic with a = 4.011(1) and psuedocubic with a = 3.983(1) and c = 4.032(3), respectively.[27]

The average crystallite sizes found within the submicron grains of the bulk powders were 26 ± 2 and 59 ± 6 nm for the respective heating conditions. The crystallite sizes were calculated from the (111) reflection using the single line parameterized Warren-Averbach method, which measures crystallite size (column length) and

microstrain. Akogdan's recent work on the measurement of critical size using diffraction techniques illustrated that microstrain increased for $BaTiO_3$ nanoparticles < 150 nm and therefore is not negligible for mesocopic ferrolectrics when evaluating size.[28] As seen in Chapter 3, the electron micrographs revealed that our powders are agglomerated and both tubes and fibers have grains that are under some strain to form the morphology; thus, it could not be assumed that microstrain had no effect The effect of crystallite size on the relative tetragonality (c/a) of the powder calcined at 1000 °C was similar to the c/a = 1.011 from the PDF file and the c/a = 1.000 for the powder calcined at 650 °C.[18]

Diffraction patterns of the nanofibers, Figure 4.4, formed in the 200 nm pores of PC templates and calcined at 650° and 1000 °C were also indexed to the psuedocubic phase. Crystallite sizes for the fibers were determined to be 28 ± 3 and 34 ± 3 nm, respectively. It is important to note that these results are based on crystallites measured from an array of 6 μm long fibers attached to a 1 μm thick film, each with different grain sizes. Both morphologies of the fibers had a decrease of ~0.8% with the c/a = 1.003. This value is close to the lowest c/a of 1.002 determined for 70 nm $BaTiO_3$ particles measured by TEM.[29] A critical size of 67 nm crystallites, determined by neutron diffraction, also has a c/a = 1.002.[28] Figure 4.5 shows PXRD pattern for $BaTiO_3$ nanotubes formed form the 200 nm AAO template. The phase of the nanotubes was identified as cubic with an average crystallite size of 13 nm which is in accordance with the grain size measurement from TEM, Figure 3.2d, and may be single-domain.[30]

Raman Spectroscopy of $BaTiO_3$. The crystal symmetry of $BaTiO_3$ was confirmed by Raman spectroscopy at room temperature. The modes of vibration are summarized in Table 4.2 and were assigned based on single crystal data reported by

Table 2. Raman Scattering Data for $BaTiO_3$ Bulk Powders, Tubes and Fibers

Material & Processing Temperature	PXRD Symm. d_{XRD} (nm)	$\nu_1(cm^{-1})$ (TO)	$\nu_2(cm^{-1})$ (LO)	$\nu_3(cm^{-1})$ (LO,TO)	$\nu_4(cm^{-1})$ (TO)	$\nu_5(cm^{-1})$	$\nu_6(cm^{1})$ (LO)	$\nu_7(cm^{1})$
Powder,	Cubic	182	266	306	520	636	716	---
1000 °C	59							
Powder,	Cubic	---	---	306	522	632	721	1057
650 °C	26							
200 nm Tubes,	Cubic	---	---	---	525	639	725	---
650 °C	13							
200 nm Fibers,	Cubic	---	265	305	521	---	787	---
1000 °C	34							
200 nm Fibers,	Cubic	---	---	305	523		---	914
1000 °C	28							

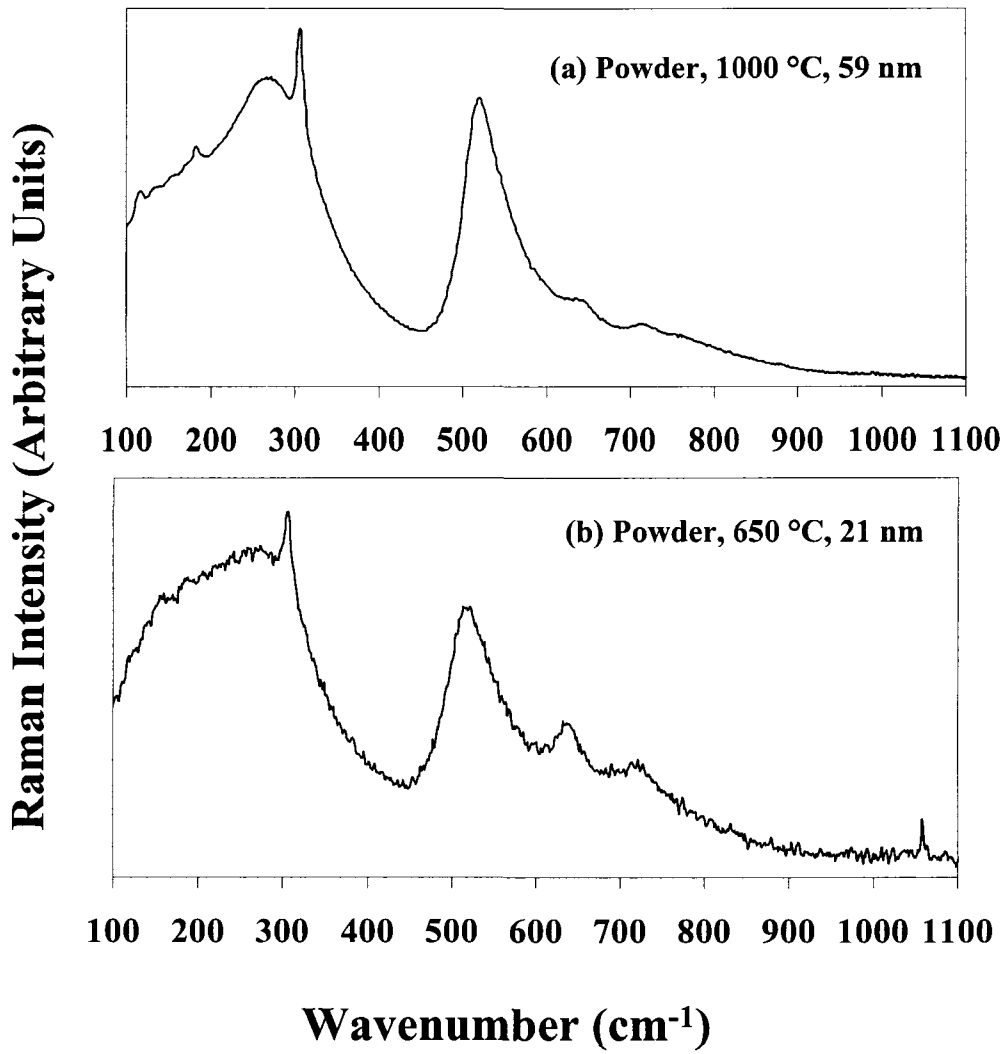

Figure 4.6. Room temperature Raman spectra for $BaTiO_3$ powder calcined at (a) 1000 °C and (b) 650 °C. The average crystallite size is 59 and 26 nm, respectively.

Perry and Hall.[31] Room temperature Raman spectra for bulk powders, Figure 4.6, calcined at 650° and 1000 °C have vibrational modes associated to the tetragonal phase. Based on group theory, all four of the optical modes of cubic perovskite-type materials should be Raman inactive, whereas seven of the optical modes for the polar tetragonal phase should be Raman active.[22,32] The discrepancy between PXRD and Raman data for $BaTiO_3$ suggests that the powders have more than phase or that PXRD was unable to resolve the closely spaced (001) and (100) peaks.[33] According to Perry and Hall, the following peaks centered at identify the room temperature tetragonal phase of $BaTiO_3$: 269, 306, 516, and 720 cm^{-1}.[31] Bulk powder calcined at 1000 °C had two peaks not identified with the tetragonal phase. A peak, centered at 182 cm^{-1} is attributable to the orthorhombic phase of $BaTiO_3$. These two phases have similar spectra and are differentiated by weak peak intensities found in the range of 180-195 cm^{-1}.[26,31] A small amount of CO_3^{-2} impurity was identified with the peaks centered at 1057 cm^{-1} for powder calcined at 650 °C and shoulders found near 636 cm^{-1} for powders calcined at 650° and 1000 °C.[34] The carbonate impurity arises from the presence of $BaCO_3$ for the temperature ranges employed above.[34,35]

Raman spectra for 200 nm fibers formed from the polycarbonate template, Figure 4.7, also reveal the presence of tetragonal symmetry. However, the difference in calcination temperatures did cause the formation of phase pure tetragonal nanofibers. The spectrum of fibers calcined at 1000 °C, Figure 4.7a, had only tetragonal peaks assignable, whereas fibers calcined at 650 °C showed the presence of the CO_3^{-2} peak at 914 cm^{-1}. These spectra also illustrate the effect of crystallite size on the tetragonality of $BaTiO_3$ through the sharpness of the peak at 305 cm^{-1}. Peak intensity has been shown to

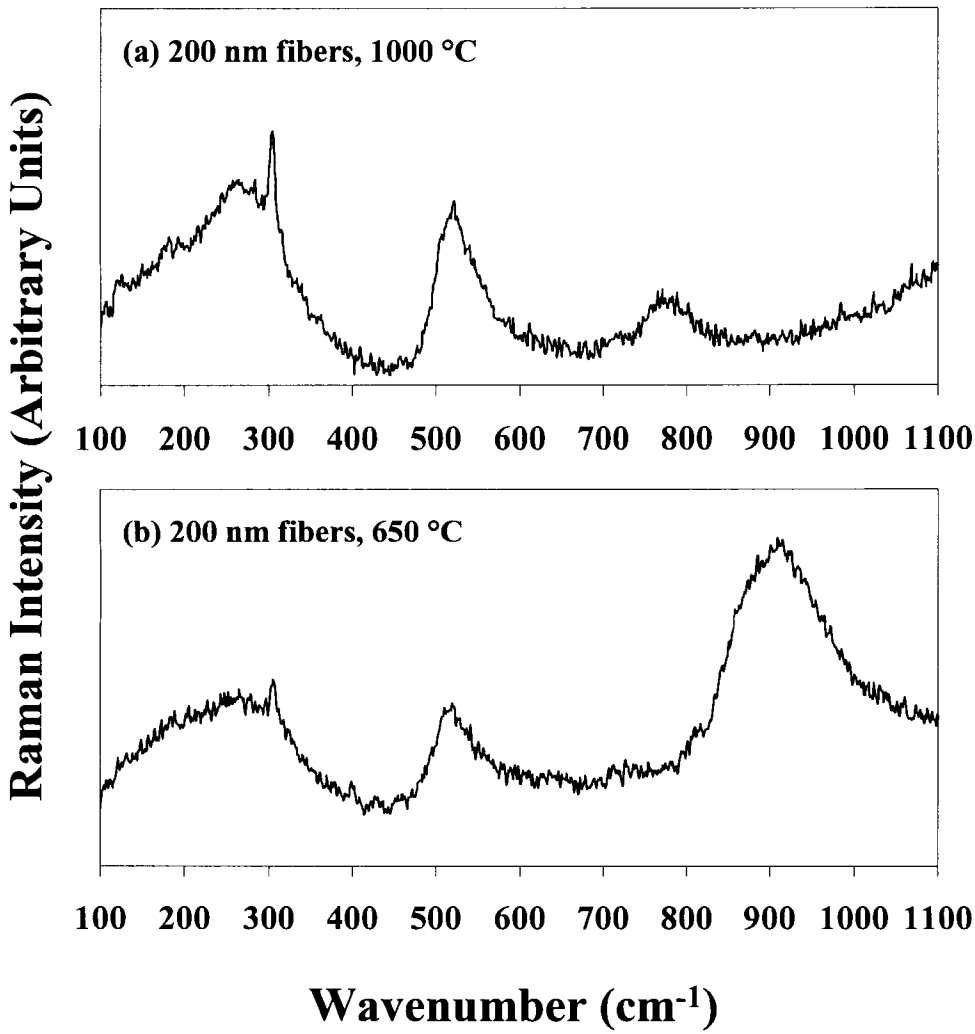

Figure 4.7. Room temperature Raman spectra for the 200 nm $BaTiO_3$ fibers calcined at (a) 1000 °C and (b) 650°C verifying tetragonal symmetry in both samples.

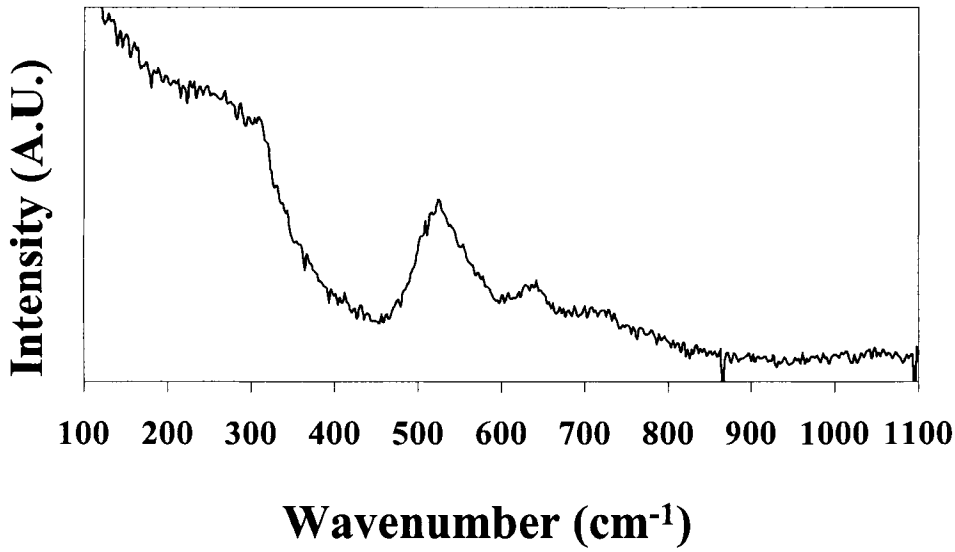

Figure 4.8. Room temperature Raman spectrum verifying the tetragonal symmetry of the 200 nm $BaTiO_3$ nanotubes (AAO template) calcined at 650 °C.

increase as $BaTiO_3$ undergoes the phase change from the cubic into tetragonal phase for both single crystal and polycrystalline materials.[22,26,31] Nanotubes formed from the AAO template were examined by Raman, Figure 4.8, and have a general features for both the tetragonal ferrolectric phase and $BaCO_3$. The peak at 305 cm^{-1} was not clearly observed; however, peaks at 525 and 725 cm^{-1} were present. Results from the Raman experiment indicate that the materials are ferroelectric.

Differential scanning calorimetery was used to monitor the phase transition temperature of $BaTiO_3$ in all the materials described above. $BaTiO_3$ undergoes a ferrolectric to paraelectric phase transition, T_c, at 120 °C.[36] DSC analysis on all the samples did not show phase transformation behavior. Crystallite sizes determined from the study were apparently too small for DSC to observe the enthalpy of transiton. A better understanding of the polarizabilty of the $BaTiO_3$ nanostructure may be realized with other analytical techniques. Recently, the Park group demonstrated that single crystalline $BaTiO_3$ nanowires with diameters of 10-60 nm could be polarized under high vacuum conditions using scanning probe techniques.[37] Using X-ray absorption near-edge structure (XANES) spectroscopy of $BaTiO_3$ nanocrystals, Rumpf et al. observed a pronounced distortion in the lattice symmetry in particles less than 20 nm.[38] Crystallite sizes within our $BaTiO_3$ one-dimensional materials, determined from PXRD, fall within this range.

III B. Examination of 1-D Paraelectric $SrTiO_3$ Materials

Powder X-ray Diffraction. The average room-temperature crystal structure was evaluated with PXRD. Lattice parameters and average crystallite size calculated from the PXRD data are summarized in Table 4.2. $SrTiO_3$ bulk powder, fibers and tubes formed within 200 nm PC templates, Figure 4.9, were indexed to have the cubic unit cell and space group Pm3m (221).[39] Bulk powder calcined at 650 °C for 6-12 hours was typically a mixed phase of $SrTiO_3$, TiO_2, and $SrCO_3$. Powders, calcined at temperatures above 900 °C, gave the single cubic phase of $SrTiO_3$. PXRD results of the nanotubes calcined at 650 °C did not reveal the presence of $SrCO_3$ or TiO_2 indicating that the solid-state reaction was completed. This may have occurred because the smaller grain sizes of the nanotubes may have allowed for diffusion of the reactants to occur.

The average crystallite size for the respective samples calculated from the (110) reflection were 97 ± 10, 35 ± 4, and 27 ± 3 nm. The diffraction pattern for the nanotubes formed in the AAO template, Figure 4.10, was also indexed to the cubic phase and had an average crystallite size of 17 ± 2 nm . The cubic lattice parameters were calculated and found to be ~0.4% smaller than the reference data, indicating a strain on the unit cell. All four samples were characterized by PXRD and found to be in the paraelectric phase.

Room temperature Raman experiments were not performed because the cubic phase is Raman inactive. Room temperature $SrTiO_3$ will never have tetragonal symmetry because it is considered to be a quantum paraelectric, and therefore is not stable in the ferroelectric phase.[40] $SrTiO_3$ undergoes only a structural transition from cubic to tetragonal at T_o = -163 °C.[5] Raman scattering experiments have been performed on sol-

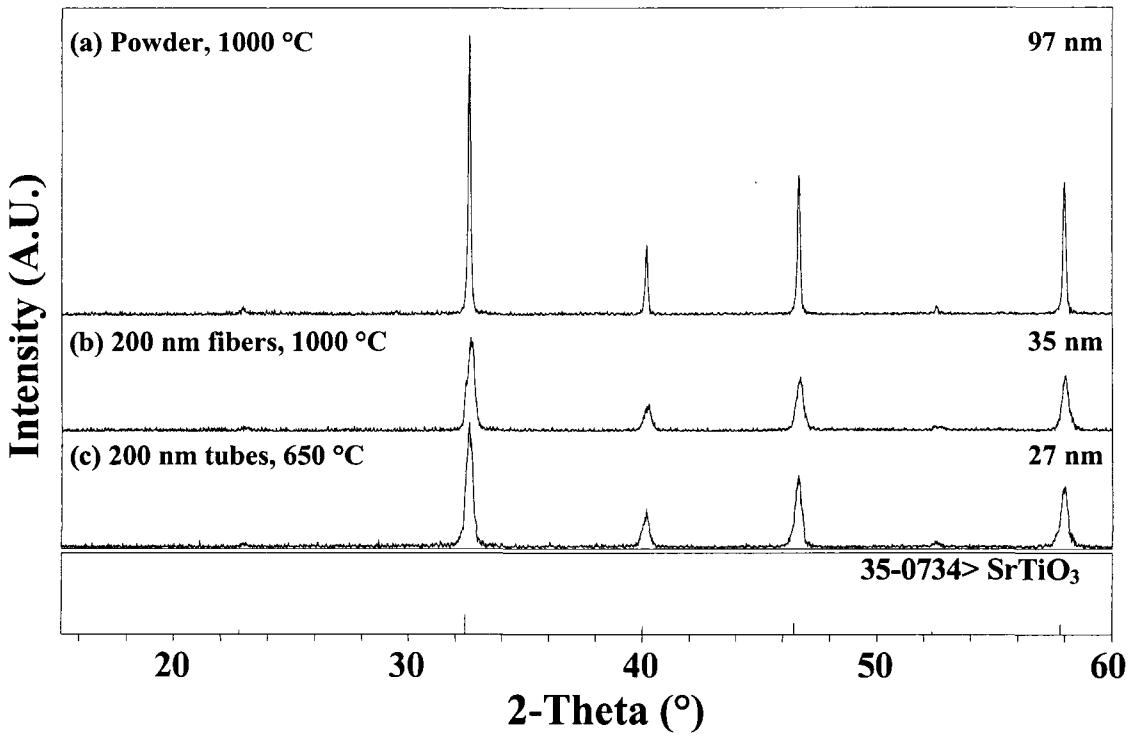

Figure 4.9. Powder XRD patterns for the bulk material calcined at (a) 1000 °C, 200 nm fibers (PC) calcined at (b) 1000 °C, and (c) tubes (PC) calcined 650 °C with 97, 35, and 27 nm crystallite sizes, respectively. Each sample was indexed to have the cubic phase and illustrates the effects of grain/crystallite size on the relative intensity and broadening of the peaks.

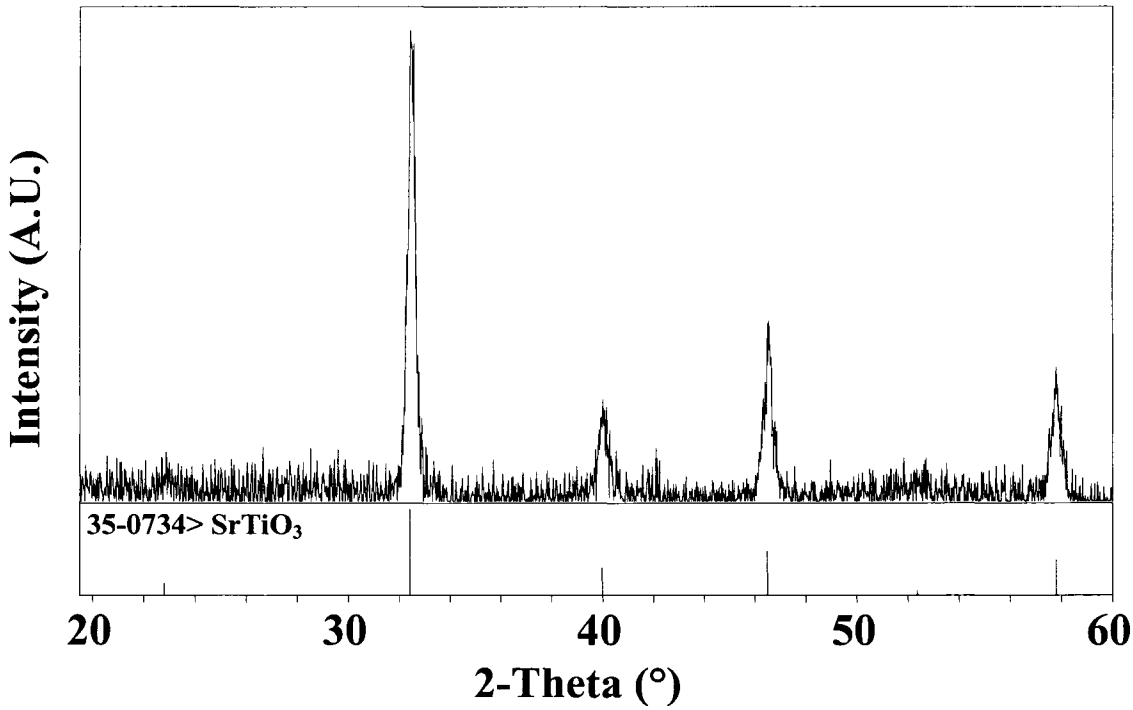

Figure 4.10. Powder XRD pattern for the $SrTiO_3$ nanotubes (AAO) indexed to the cubic phase. The average crystallite size calculated was 17 nm.

gel deposited $SrTiO_3$ thin films and sol-gel derived powders, demonstrating the effectiveness of identifying structural change within the temperature range of –203 to 307 °C.[40] Size effects on the paraelectricity has been recently investigated by Song, et al.[5] Similar to $PbTiO_3$ Raman experiments discussed in Chapter 3, symmetry changes from the cubic to tetragonal symmetries at low temperatures caused frequency shifts and intensity changes for the soft mode. Also demonstrated was the size effect on the dielectric properties and the quantum paraelectric phase transition temperature of $SrTiO_3$.[5] As particle size decreased, both dielectric constant and transition temperature increased. Based on the Raman experiments utilized to observe size effects of $PbTiO_3$ and $BaTiO_3$, our $SrTiO_3$ nanotubes and fibers are excellent candidates to study the effects of size on quantum paraelectricty.

III. C. Analysis of UV-Visible Reflectance Edge Energy

UV-visible optical diffuse reflectance spectra of $BaTiO_3$ and $SrTiO_3$ powders, fibers, and tubes were calculated from reflectance data using the Kubelka-Munk function,[41]

$$\alpha/S = (1-R)^2/2 \qquad (4.1)$$

where R is the reflectance at a given wavelength, and α is the scattering coefficient. The optical band gap energy, Eg, is extracted from the $(\alpha/S)^2$ versus energy plot. Eg is taken as the point where the extrapolated linear portion of the plot intersects the energy axis at $(\alpha/S)^2 = 0$. This energy is the minimum photon energy required to excite an electron from the highest unoccupied molecular orbital (HOMO) found in the valence

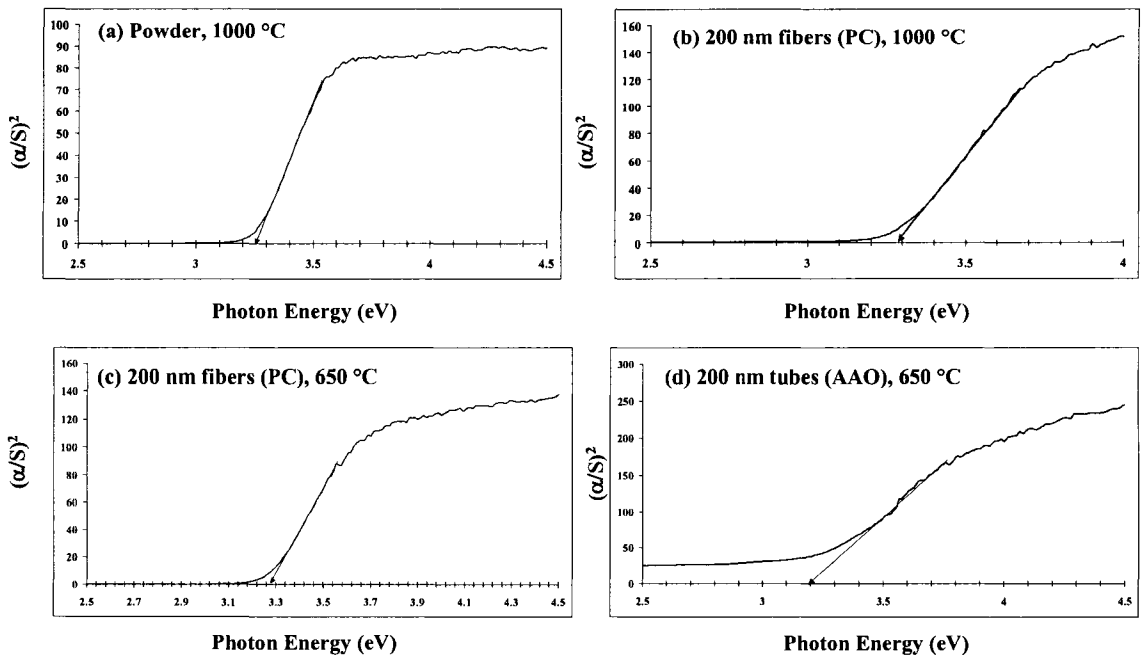

Figure 4.11. Diffuse reflectance UV-Vis spectra of $BaTiO_3$ (a) powder calcined at 1000 °C, (b) 200 nm fibers (PC) calcined at 1000 °C, (c) 200 nm fibers (PC) calcined at 650 °C, and (d) 200 nm tubes (AAO) calcined at 650 °C.

band to the lowest unoccupied molecular orbital (LUMO) found in the conduction band.[42] In semiconducting materials, a direct or indirect electronic transition can occur. These transitions influence the energy dependence of scattering coefficient

$$\alpha \propto (h\nu - Eg)^{\eta}/(h\nu) \qquad (4.2)$$

Through the exponent η= 1/2, 3/2, 2, and 3 for direct allowed, direct forbidden, indirect allowed, and indirect forbidden transitions, respectively.[42] While $BaTiO_3$ and $SrTiO_3$ have been evaluated for both direct and indirect transitions, there is still a debate over which electronic transition best describes the perovskite semiconductors, and so both η= 1/2 and 2 have been used in the literature. [2] Therefore, the method used in this chapter is only an approximation to the actual bandgap energy calculated using the direct transition exponentη= 1/2.

The reflectance spectra of $BaTiO_3$ bulk powder, fibers, and nanotubes are presented in Figure 4.11. Similar spectra were observed for $SrTiO_3$. No significant crystallite size effect was observed for the materials analyzed. Eg = 3.24, 3.28, 3.25, and 3.20 eV were observed for bulk powder (1000 °C), nanofibers (1000° and 650°C), and nanotubes (650°C), respectively. These values fall within the range of reported energies of 2.95-3.95.[2] Optical band gap energies of $SrTiO_3$ bulk powder, 200 nm fibers and tubes formed in PC had values of Eg = 3.10, 3.13, and 3.16 eV, respectively. The energies found are similar to an optical band gap of Eg = 3.18 reported for nanocrystalline $SrTiO_3$.[7] These results suggest that room temperature photoluminescence of the perovskite nanostructures would not be observed. Investigations on the roles of defects in crystallites on room temperature PL, has shown that amorphous $SrTiO_3$ has changes in optical band gap energy to Eg = 2.69 eV and intense PL in the visible region when an

excitation wavelength of 488.0 nm was used.[7] All of our samples were crystalline and did not show PL at room temperature. This is in agreement with bulk materials at room temperature.

IV. Summary

An investigation to study and promote the change of grain size observed for fibers and forming nanotube structures was performed on $SrTiO_3$ and $BaTiO_3$ made within PC templates. The formation of perovskite nanotubes within the channels of the PC templates was demonstrated for the first time. The effects of annealing and incomplete filling of the PC template were determined responsible for the morphologies observed. Large grains formed the "string of grains" morphology, while small grains formed either fibers similar to Limmer or nanotubes, which have not been prepared before by PC templates. Structural characterization of the perovskites symmetry identified the (ferroelectric) tetragonal symmetry for $BaTiO_3$ and (paraelectric) cubic symmetry of $SrTiO_3$. Electronic phase transitions were not monitored for $BaTiO_3$ using DSC because crystallite sizes found within the grains were too small to be well resolved. The examination of structure and electronic properties was performed by UV-vis diffuse reflectance spectroscopy. UV-visible absorption edge analysis of the optical bandgap of the perovskites was calculated and compared to literature values. Significant band gap energy changes and room temperature photoluminescence have been observed in the literature for amorphous perovskite nanoparticles, however, the crystalline 1-D perovskites exhibited no significant size effects when compared to the macrocrystalline bulk powders.

References

(1) Robertson, J., *J. Appl. Phys.* **2003,** 93, 1045-1059.

(2) Golego, N.; Studenikin, S. A.; Cocivera, M., *Chem. Mater.* **1998,** 10, 2000-2005.

(3) Pfaff, G., *J. Mater. Chem.* **1992,** 2, 591-594.

(4) Pfaff, G., *J. Mater. Chem.* **1993,** 3, 721-724.

(5) Song, T. K.; Kim, J.; Kwun , S.-I., *Ferroelectrics.* **1997,**197, 135-130.

(6) Akdogan, E. K.; Leonard, M. R.; Safari, A., Size Effects in Ferroelectric Ceramics. In *Handbook of Low and High Dielectric Constant Materials and Their Applications*, ed.; Academic Press: **1999**;pp 61-112.

(7) Pinheiro, C. D.; Longo, E.; Leite, E. R.; Pontes, F. M.; Magnani, R..; Varela, J. A.; Pizani, P. S.; Boschi, T. M.; Lanciotti, F., *Appl. Phys. A* **2003,** 77, 81-85.

(8) Zhang, L.; Zhong, W.-L.; Kleemann, W., *Phys. Lett. A* **2000,** 276, 162-166.

(9) Zhang, J.; Lee, B. I.; Besson, J. J.; Mann, L., Structure and Dielectric Characterization of $BaTiO_3$ Composite Thick Films By Sol-Gel Powder Coating Process. In *Electronic Ceramic Materials and Devices*; American Ceramic Society: pp 541-549.

(10) Lanciotti, F.; Pizani, P. S.; Campos, C. E. M.; Leite, E. R.; Santos, L. P. S.; Carreno, N. L. V.; Longo, E., *Appl. Phys. A* **2002,** 74, 787-789.

(11) Boyle, T. J.; Dimos, D.; Schwartz, R. W.; Alam, T. M.; Sinclair, M. B.; Buchheit, C. D., *J. Mater. Res.* **1997,** 12, 1022-1030.

(12) Doeuff, S.; Dromzee, Y.; Taulelle, F.; Sanchez, C., *Inorg. Chem* **1989,** 28, 4439-4445.

(13) Limmer, S. J.; Seraji, S.; Wu, Y.; Chou, T. P.; Nguyen, C.; Cao, G., *Adv. Funct. Mater.* **2002,** 12, 59-64.

(14) Patzke, G.; Krumeich, F.; Nesper, R., *Angew. Chem., Int. Ed. Engl.* **2003,** 41, 2446-2461.

(15) Rao, C. N. R.; Nath, M., *Dalton Trans.* **2003,** 1, 1-24.

(16) Rao, C. N. R.; Deepak, F. L.; Gundiah, G.; Govindaraj, A., *Prog. Solid State Chem.* **2003,** 31, 5-147.

(17) Xia, Y.; Yang, P.; Sun, Y.; Wu, Y.; Mayers, B.; Gates, B.; Yin, Y.; Kim, F.; Yan, H., *Adv. Mater.* **2003,** 15, 353-388.

(18) *PDF # 31-0174.*

(19) *PDF # 05-0626.*

(20) Zhou, Q. F.; Zhang, J. X.; Chan, H. L. W.; Choy, C. L., *Ferroelectrics* **1997,** 195, 221-214.

(21) Cullity, B. D., *Elements of X-Ray Diffraction.* 2nd ed.; Addison-Wesly: Massachusetts, **1978**.

(22) Asiaie, R.; Zhu, W.; Akbar, S. A.; Dutta, P. K., *Chem. Mater.* **1996,** 8, 226-234.

(23) Ma, Y.; Vileno, E.; Suib, S.; Dutta, P. K., *Chem. Mater.* **1997,** 9, 3023-3031.

(24) Yukawa, K.; Wakino, K., *Interg. Ferroelect.* **1998,** 20, 107-115.

(25) Schlag, S.; Eicke, H.-F.; Stern, W., *Ferroelectrics* **1995,** 173, 351-369.

(26) Frey, M. H.; Payne, D. A., *Phys. Rev. B.* **1996,** 54, 3158-3168.

(27) Jade; Inc., M. D., *XRD Pattern Processing* **1999**.

(28) Akdogan, E. K.; Mayo, W.; Safri, A.; Rawn, C. J.; Payzant, E. A., *Ferroelectrics* **1999,** 223, 11-18.

(29) Sakabe, Y.; Wada, N.; Hamaji, Y., *J. Korean. Phys. Soc.* **1998,** 32, S260-S264.

(30) Akdogan, E. K.; Safari, A. In *Size Effects in Nanophase $PbTiO_3$*, 2000 12th IEEE Interanational Symposium on Applications of Ferroelectrics, Honolulu, Hawaii, U.S. A., 2000; Honolulu, Hawaii, U.S. A., 2000; pp 487-490.

(31) Perry, C. H.; Hall, D. B., *Phys. Rev. Lett.* **1965,** 15, 700-702.

(32) Fately, W. G.; Dollish, F. R.; McDevitt, N. T.; Bently, F. F., *Infared and Raman Selection Rules For Molecular and Lattice Vibrations*. Wiley-Interscience: New York, **1972**.

(33) Frey, M. H.; Payne, D. A., *Phys. Rev. B* **1996,** 54, 3158-3168.

(34) Duran, P.; Capel, F.; Guiterrez, D.; Tartaj, J.; Banares, M.; Moure, C., *J. Mater. Chem.* **2001,** 11, 1828-1836.

(35) Frey, M. H.; Payne, D. A., *Chem. Mater.* **1995,** 7, 123-129.

(36) Jona, F.; Shirane, G., *Ferroelectric Crystals*. ed.; MacMillan: New York, **1962**.

(37) Yun, W. S.; Urban, J. J.; Gu, Q.; Park, H., *Nano Letters* **2002,** 2, 447-450.

(38) Rumpf, H.; Modrow, H.; Hormes, J.; Glasel, H.-J.; Hartmann, E.; Erdem, E.; Bottcher, R.; Hallmeir, K.-H., *J. Phys. Chem. B.* **2001,** 105, 3415-3421.

(39) *PDF # 35-0734.*

(40) Gupta, S.; Katiyar, R. S., *J. Raman Spectrosc.* **2001,** 32, 885-891.

(41) Kortum, G., *Reflectance Spectroscopy: Principles, Methods, Applications*, Springer-Verlag: New York, **1969**; p 111.

(42) Barton, D. G.; Shtein, M.; Wilson, R. D.; Soled, S. L.; Iglesia, E., *J. Phys. Chem. B.* **1999,** 103, 630-640.

CHAPTER 5

Template Synthesis and Characterization of $NdNiO_3$ Nanofibers: Possible Models for The Examination of Metal-Insulator Transition

I. Introduction

The rare earth nickel oxide perovskites ($RENiO_3$, nickelates), with the exception of $LaNiO_3$, are a unique class of metal oxides that posses metal-insulator (MI) phase transitions. $LaNiO_3$ is the only nickelate that is considered to be purely metallic while Pr, Nd, Sm, Eu, and Gd become insulators below the phase transition temperature, with T_{MI} = -143°, -73°, 127°, 207°, and 227 °C, respectively.[1] The phase transition temperature decreases as the rare earth ion becomes larger and increases the distortion from the ideal cubic unit cell. The distortion arises from the tilt and rotation of the NiO_6 octahedra to fill the space around the rare earth's decreasing ionic radii.[2] The decrease in atomic radius is known as the lanthanide contraction cause by the 4f-orbitals poor shielding properties.[3]

The nickelates have become important to the investigation of MI because, unlike other metal oxides, they have the advantage of not requiring electron or hole doping to induce MI.[4] It has been proposed that the of Ni-O-Ni angle has an influence on the behavior of the material and that the MI transition is brought about by the charge-transfer from the oxygen p-orbitals to the Ni d-orbitals.[5] The $RENiO_3$ perovskites also have antiferromagnetic ordering that arises near or at the MI transition.[4] Simultaneous electronic, magnetic, and structural changes have made it difficult to determine the exact cause of the MI. These unique physical changes and the associated structure-property relationships make the nickelates attractive to the investigation of one-dimensional $RENiO_3$ morphologies. These metal oxides have not been explored by template synthesis, nor have they been synthesized to form 1-D materials. This chapter describes the synthetic route used to form the first $NdNiO_3$ nanofibers.

Polycrystalline $NdNiO_3$ has been synthesized through both traditional solid-state reactions and by sol-gel routes.[6,7] These two synthetic methods have used a combination of variable O_2 pressures and temperatures. Demazeau et al. used solid-state synthesis for $NdNiO_3$, and other rare-earth nickelates isotypic with $LaNiO_3$, from a mixture of NdO_3, NiO, and $KClO_3$.[6] A series of investigations have explored the alternative sol-gel routes and a synopsis of their work is presented below. It should be noted that with this literature is a reported wide variability of the T_{MI} determined from polycrystalline samples made through solution routes and crystallized under different heating regimes. Both orthorhombic and rhombohedral Bravais Lattice symmetry have been reported yielding different T_{MI}. This observation may indicate that crystallite size and symmetry play a pivotal role in understanding the structural changes accompanying the metal-insulator transition.

The first report using solution techniques was by Vassiliou et al.[8] The decomposition of well mixed nitrates, where Nd_2O_3 and NiO were dissolved with HNO_3, and the sol-gel method using the Pechini route were used.[8] Chapter 1 discusses the Pechini process in further detail.[9] Both methods produced powders that were cold pressed at 4 kbar and calcined at 650 °C for 120 hours under streaming O_2 (1 atm). The resulting $NdNiO_3$ phase, synthesized by these two synthetic routes, possessed the low-pressure and temperature rhombohedrally-distorted perovskite structure. The rhombohedral pattern observed by powder X-ray diffraction was similar to $LaNiO_3$. The investigation on the MI transition for $NdNiO_3$ revealed a T_{MI} of –123 °C.

The work of Lacorre et al. also demonstrated that the decomposition of well-mixed nitrates yielded the high-pressure and temperature phase for the $NdNiO_3$. Dried

powders synthesized from the decomposition of mixed metal nitrate were calcined at 600 °C for several hours, pressed into pellets, and fired again at 1000 °C under 150-200 bar of O_2. Powders had to be reground, repressed, and fired several times to get a single phase. The symmetry produced under these heating conditions was similar to the orthorhombic phase of $GdFeO_3$ with a T_{MI} of -73 °C.[10] Since this work, others have used the Pechini sol-gel method and varied heating and pressure conditions to produce the orthorhombic phase of $NdNiO_3$.

The powders synthesized by Blasco et al. were prepared by heating the solids under O_2 at 400 °C overnight. The powders were then pressed into pellets at 4kbar, and sintered for 10 days at 650 °C under an O_2 flow.[11] The phases of the polycrystalline powders formed under these conditions were monitored during the heating process and removed from the heat, reground, and heated again. One sample that was heated for 10 days was sintered once more at 750 °C to yield the orthorhombic phase. This sample was reported to have a T_{MI} = -68 °C. TGA results indicated that the sample was the oxygen deficient: $NdNiO_{2.91\pm0.03}$. There is only one other report on oxygen deficient $NdNiO_3$ using the Pechini method.[12] Tiwari et al. followed the synthetic procedure set forth by Vassiliou with the exception of refluxing the Pechinni sol at 87 °C for 24 hours.[12] Pressed powders were sintered for 12 hours at 650 °C under streaming O_2. From this synthetic route, an orthorhombic oxygen deficient $NdNiO_{2.88}$ was determined to have anomalous thermoelectric power and a T_{MI} = -93 °C.

Other chemistries have been compared to the Pechini sol-gel route to synthesize $NdNiO_3$ and have shown not to be as effective in producing single-phase samples. Escote et al. compared the physical properties of $NdNiO_3$, $SmNiO_3$, and $PrNiO_3$ prepared

by sol-gel, hydroxide precipitation, and the solid-state reaction of simple oxides.[7] Pressed powders (1kbar) were heated from 800 ° to 1000 °C under O_2 pressures up to 50 bar. Of the three synthetic methods, only the sol-gel process generated single-phase orthorhombic $RENiO_3$ when calcined at 1000 °C. SEM analysis of the powders showed different grain sizes generated by the three different methods. Grain sizes of ~3, 2, and <1 μm were formed, respectively, for the simple oxide, hydroxide precipitation, and sol-gel routes. Escote proposed that the smaller grain size and single phase obtained, demonstrated that sol-gel methods were more suitable for the precise microstructural control of the nickelates. Using DSC, $NdNiO_3$ was examined and found to have a $T_{MI} = -83$ °C

And most recently, Fernandes et al. used the Pechini method to generate powders that were heated at 800 °C for 6, 12, 18, and 40 hours, producing single-phase orthorhombic $NdNiO_3$ with crystallite sizes ranging from 12-20 nm. The 20 nm $NdNiO_3$ was found to have the lowest reported room temperature resistance (1.1×10^{-4} Ωcm) and a $T_{MI} = -123$°C. Clearly there is debate in the literature about which phase is contributing to the measured MI transitions. These results may indicate that there is a possible crystallite size effect on the electronic properties of the nickelates.

II. Experimental Methods.

$NdNiO_3$ nanofibers and bulk powders were prepared using the low temperature and low-pressure synthetic route described in Chapter 2. In contrast to the literature, bulk powders were prepared from gels that were dried at atmospheric pressure overnight at 90 °C. Powders were not pressed into pellets before the calcination process. Heating

conditions described by Fernandes et al. and Vassiliou et al. were followed but modified with the addition of our heating profile.[8,13] Loose powders were calcined at a rate of 50 °C/hour to 800 °C. Two samples were heated in air for 40 hours and for 120 hours, whereas the third was heated under streaming O_2 (25 sccm, Cole Palmer flow meter) for 40 hours. Powders were cooled to room temperature at a rate of 30 °C/hour.

Masked PC templates were coated with the clear green sol and were allowed to air-dry overnight. Prior to the calcination process, templates were reinforced by inserting them between Al_2O_3 plates (dimensions of a microscope slide) and placed upright in a combustion boat. The templates were calcined in air at a rate of 50 °C/hour to 800 °C, and were kept at this temperature for 40 hours for the 100 nm PC templates and 120 hours for the 200 nm templates before being slowly cooled to room temperature at a rate of 30 °C/hour.

III. Results and Discussion

Powder X-ray Diffraction. A series of heating conditions were initially examined to produce single-phase $NdNiO_3$ bulk powders. PXRD patterns, Figure 5.1, show the results obtained for three of the heating conditions explored. The heating profile chosen was based on the synthetic route reported by Fernandes, who calcined loose powders in

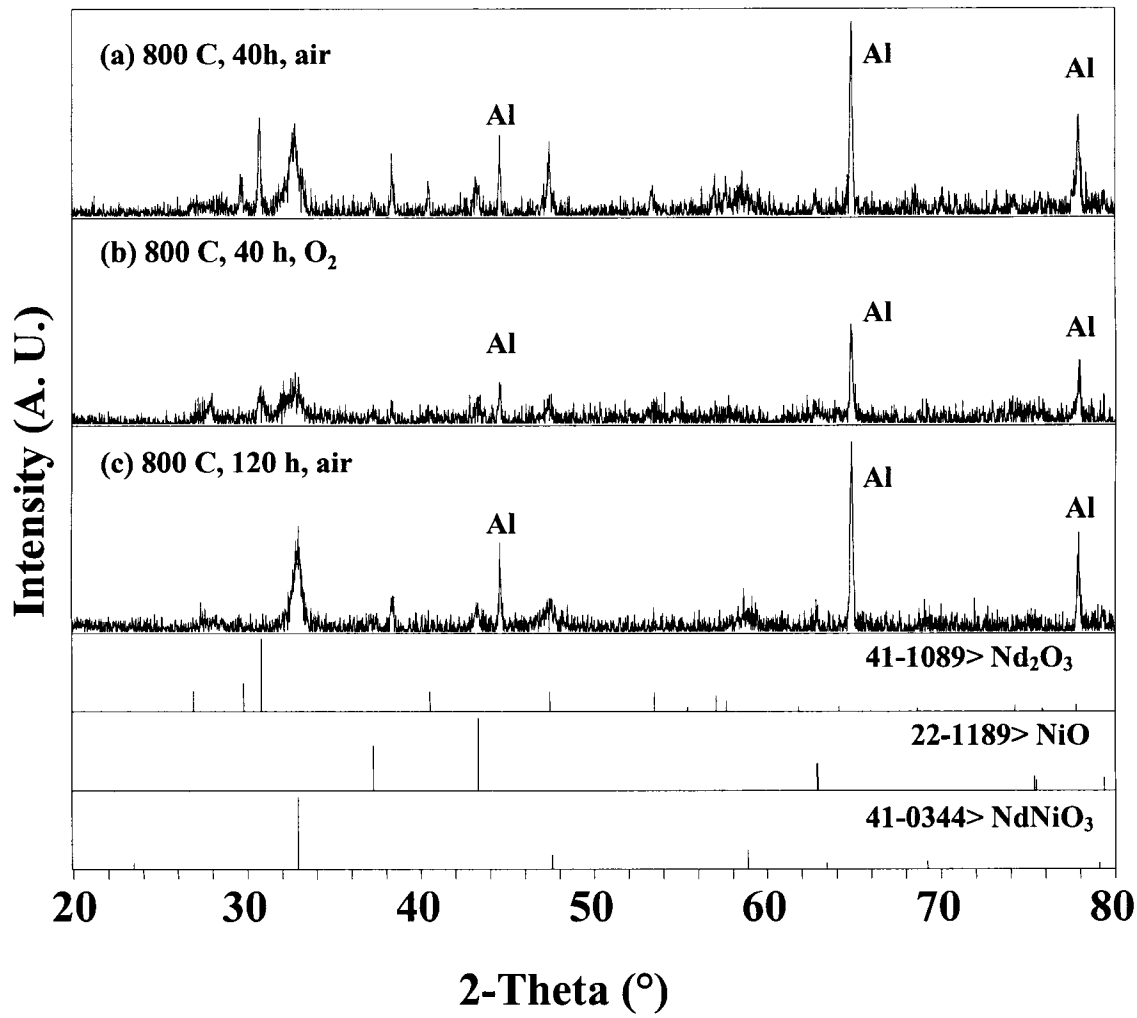

Figure 5.1. PXRD patterns of bulk powders synthesized with various heating conditions. All samples were mounted in an aluminum holder. (a) Bulk powder calcined at 800 °C for 40 h in air. (b) Bulk powder calcined at 800 °C for 40 h under streaming O_2. (c) Bulk powder calcined at 800 °C for 120 h in air.

air at 800 °C for 40 hours.[13] This synthetic procedure was attractive because it yielded the orthorhombic (Pbnm) phase of $NdNiO_3$ without the use of high pressure and oxygen.[13] Powder calcined in air for 40 hours, Figure 5.1a, had a mixed-phase pattern of Nd_2O_3, NiO, and the low-pressure rhombohedral phase of $NdNiO_3$ determined by Vassiliou and not the high-temperature and pressured orthorhombic phase.[8,10] This result indicated that the reaction time needed to be increased for the completion of the solid-state reaction of the nickelates:

$$RE_2O_3 + 2NiO + \tfrac{1}{2}O_2 \rightarrow 2RENiO_3 \qquad (5.1)$$

and/or an oxidizing atmosphere was required to help stabilize the Ni(III).[10] Increasing the temperature to 900 °C to obtain a pure phase was not pursued because of the oxygen loss that can occur at higher temperatures when calcined at 1 atm. DTA-TGA experiments under N_2 have confirmed that the following reaction:

$$2NdNiO_3 \rightarrow Nd_2NiO_4 + NiO + \tfrac{1}{2}O_2 \qquad (5.2)$$

began at 900 °C and peaked at 960 °C, whereas under an O_2 atmosphere the reaction peaked at 1050 °C.[8] A second set of heating conditions was investigated to determine the optimal oxygen atmosphere and dwell time required to complete the reaction. Powder calcined under O_2 for 40 hours, Figure 5.1b, contained the same mixed-phases found in powder calcined in air. A third powder sample was calcined in air for 120 hours, Figure 5.1c, had the lowest peak intensities for Nd_2O_3 and NiO yet, their presence still indicated the reaction was not complete after 120 hours at 800 °C.

The long reaction time needed for the synthesis of phase-pure $NdNiO_3$ generated concern about annealing effects on grain size and identification of nanostructure

morphology that could be produced with 40 and 120 hour reaction times. Heating profiles used in the previous chapters for PC templates had dwell times of 6 hours at the desired temperature to obtain phase-pure perovskite nanostructures. Typically, $PbTiO_3$ fibers with a string of grain morphology were observed when a 0.8 M chelate sol-gel was applied to PC templates and calcined at 650 °C. Tube formation using PC templates could be achieved, as demonstrated with $SrTiO_3$, Chapter 4, when the molarity of the sol was reduced and templates were calcined at 650 °C. However, it was also observed that reaction temperature changed the morphology of the $SrTiO_3$ from nanotubes to nanofibers when the 0.5 M sol was used and templates were calcined at 1000 °C. These results demonstrated that the reaction conditions affected the grain size and morphologies of the nanomaterials. One hypothesis is that template synthesis would yield one-dimensional structures at shorter calcination times and that one thick film comprising overgrown grains may be the result of longer calcination times.

Polycarbonate tempates with 200 nm and 100 nm pores were coated with sol-gel and calcined at 800 °C in air for 120 and 40 hours, respectively. PXRD patterns for the nanostructures, Figure 5.2, were both indexed to the rhombohedrally distorted cubic perovskite phase for $NdNiO_3$ determined by Vassiliou et al.[8] The $NdNiO_3$ pattern was indexed to the psuedocubic phase. [8] Similar to crystallite size effects described in Chapter 4, line broadening prevents the observation of peak splitting found for the rhombohedral R-3c or its equivalent hexagonal D^6_{2d} symmetry.[8] The low intensity peaks, not indexed, are associated to NiO and Nd_2O_3 found during the bulk powder synthesis. Cell parameters and the crystallite size were calculated and are summarized in Table 5.1, along with the cell parameters for the rhombohedral and hexagonal phases of $NdNiO_3$.

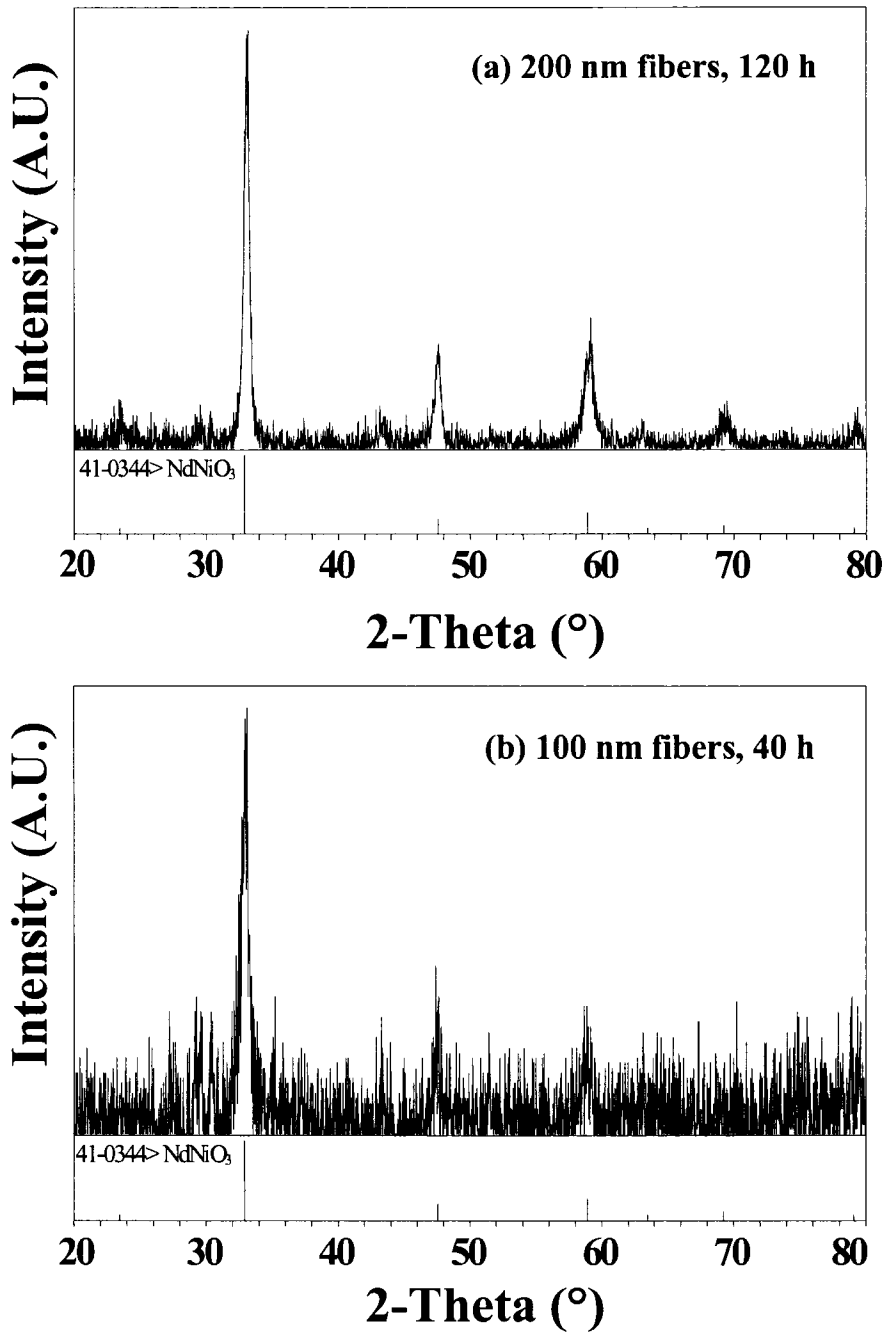

Figure 5.2. PXRD patterns for the NdNiO3 nanofibers sintered at 800 °C. (a) 200 nm fibers heated for 120 h and (b) 100 nm fibers heated for 40 h. Both samples were indexed to the rhombohedral phase of $NdNiO_3$. The average crystallite size calculated was 18 nm and 15 nm for fibers heated for 120 h and 40 h, respectively.

Table 1. Cell Parameters and Crystallite Size for $NdNiO_3$ Fibers Sintered at 800 °C

Material	a (Å)	c (Å)	Vol ($Å^3$)	Crystallite Size (nm)
Reference 8 & 15 (hex)	5.44	13.17	337.5	~17.5
Reference 8 (rhomb)	5.40	---	112.6	---
200 nm fibers, 120 hours	5.421(6)	13.166(24)	335.0	18 ± 3
100 nm fibers, 40 hours	5.430(3)	13.091(27)	334.3	15 ± 5

* Crystallite size determined with the Scherrer method using FWHM at 33.0 (°2θ)

Using the Powder Diffraction File details, the Jade software program was used to calculate the hexagonal lattice parameters.[14,15] The calculated lattice parameters fell between the values reported for the hexagonal and rhomobedral systems and there was a 0.7 and 0.9 % decrease in the hexagonal unit cell volume for the 200 nm fibers calcined at 120 hours and the 100 nm fibers calcined for 40 hours, respectively. The average crystallite size was determined using the FWHM at 33.0° (2θ) using the Scherrer Equation described in Chapter 1.[16] The 200 nm fibers had a crystallite size of 18 nm and the 100 nm fibers was 15 nm.

Electron Microscopy. SEM images, Figure 5.3, illustrate the formation of ~6 μm long fibers for both the (a) 200 nm and (b) 100 nm PC templates used. Fibers were typically attached to ~1 μm thick films, however; Figure 5.3b, illustrates fibers free of film formation. The images indicated that longer reaction times and proposed negative annealing effects at 800 °C did not interfere in the preparation of a nanostructured morphology for the $NdNiO_3$ system. The 200 nm fiber microstructure were examined with SEM and found to comprise a string of grains. The average grain size within the fiber was ~200 nm in diameter, similar to that seen with $PbTiO_3$ calcined at 650 °C and $SrTiO_3$ and $BaTiO_3$ calcined at 1000 °C (Chapters 3 and 4). TEM was used to analyze the 100 nm fibers, Figure 5.4, confirmed that fibers also comprised a string grains. The diameters of the grain sizes formed within the 100 nm PC template were measured to be on average 90-100 nm.

Differential Scanning Calorimetery. The MI transition of $RENiO_3$ can be measured through both DSC and the four-probe method.[7] The T_{MI} of the rhombohedral

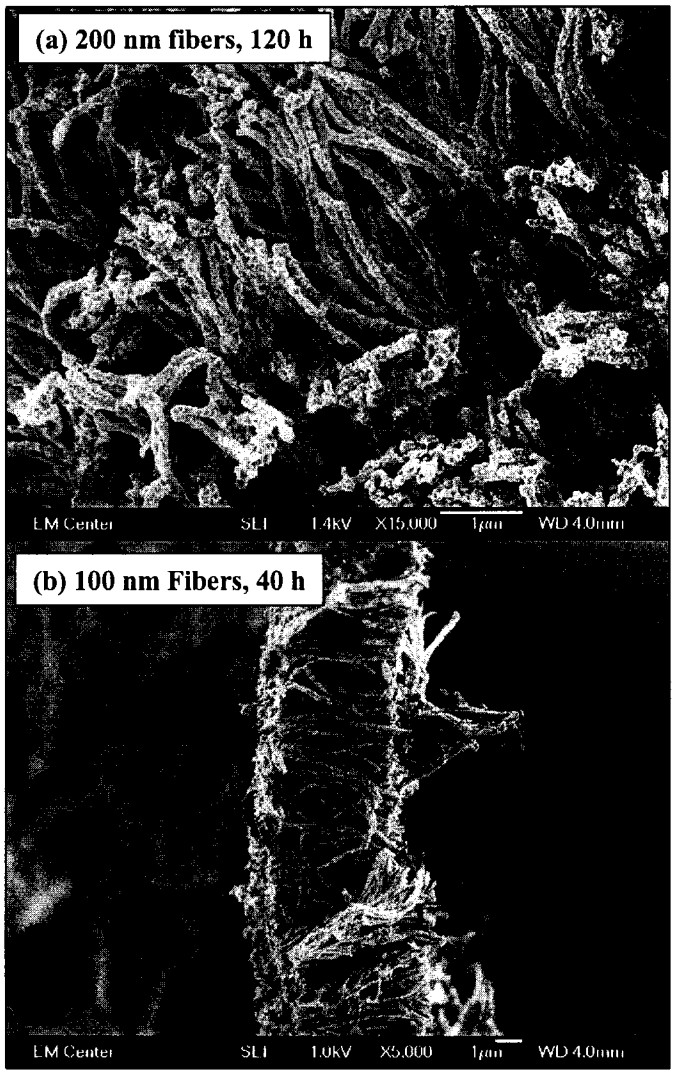

Figure 5.3. SEM images of the $NdNiO_3$ nanofibers sintered at 800 °C. (a) Top view of fibers formed within 200 nm PC templates and heated for 120 h (magnification ×15,000). The base of the fibers are attached to a ~1mm thick surface film. (b) Side view of 100 nm fibers formed within 100 nm PC templates and heated for 40 h (magnification ×5,000). Fibers are ~ 6 μm long and are free of surface film.

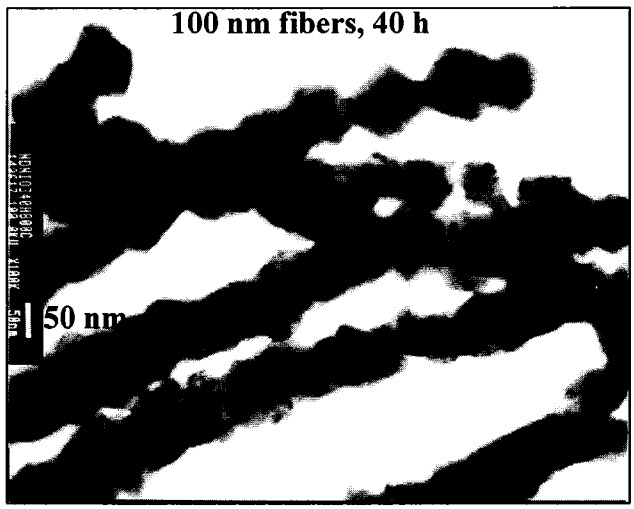

Figure 5.4. TEM image of the 100 nm $NdNiO_3$ fibers sintered at 800 °C for 40 h. Scale bar is 50 nm long. Image confirms the fibers are made up of a string of grains. The diameters of the grain sizes were measured to be on average 90-100 nm.

phase of $NdNiO_3$ has been identified at -83 °C through the four-probe method to measure resistance versus temperature, but has not been measured by DSC.[8] To investigate if the nanofibers had a T_{MI}, the 200 nm fibers were monitored under N_2 flow at 10 °C/ minute in the temperature range of –150 to 0 °C. A cyclic heating procedure was used to determine if the hysteresis in the MI transition was present. The DSC scan of the 200 nm fibers was flat and did not reveal a T_{MI} upon heating or cooling through the expected temperature range. This result may be due to the crystallite size or caused by the metal oxides present within the sample. Escote et al. showed the absence an endothermic peak, and a broad exothermic (ΔH~0.4 J/g) for $SmNiO_3$ synthesized from the simple metal oxides process.[7] PXRD detected the phases of Sm_2O_3 and NiO indicating their sample was not stoichiometeric. The single-phase sol-gel sample had a greater enthalpy of transition, ΔH~1.1 J/g, as compared to the simple metal oxide sample.

Suggested Future Work. Upon examination of both bulk powders and nanofibers with PXRD, it was revealed that a reaction time of 120 hours in air was not sufficient to produce single-phase $NdNiO_3$. Another set of experiments with the bulk powders and nanofibers needs to be performed. The first experiment should be the calcination of the materials at 800 °C for 120 hours (5 days) under an O_2 atmosphere. If these conditions do not generate a single-phase material, longer calcination times in combination with an oxidizing atmosphere should be evaluated. The heating conditions used by Blasco et al. included heating pressed powders for 10 days under oxygen flow to yield single phase orthorhombic $NdNiO_3$.[11] Once a synthetic protocol has been established to provide either the single rhombohedral or orthorhombic phase, an examination of crystal symmetry, electronic, and magnetic properties of 1-D $NdNiO_3$ can

be initiated. This is an exciting area of research, because to date there are no reports on the synthesis or characterization of 1-D $RENiO_3$ materials.

IV. Summary

The preparation of first 200 and 100 nm $NdNiO_3$ nanofibers through sol-gel template synthesis has been achieved. PXRD of the fibers indicated that the low-temperature and low-pressure rhombohedral phase was the dominant phase present and should be considered for future studies. Optimization of the synthetic conditions needs to be examined further to produce single-phase materials. Application of the synthesis protocols should include $EuNiO_3$ and $PrNiO_3$ nanofibers for the investigation of the MI properties of the $RENiO_3$ 1-D fibers.

References

(1) Medarde, M.; Lacorre, P.; Conder, K.; Rodriguez-Carvajal, J.; Rosenkranz, S.; Fauth, F.; Furrer, A., *Physica B* **1998,** 241-243, 751-757.

(2) Piamonteze, C.; Tolentino, H. C. N.; Ramos, A. Y.; Massa, N. E.; Alonso, J. A.; Martinez-Lope, M. J.; Casais, M. T., *Physica B* **2002,** 320, 71-74.

(3) Shriver, D.; Atkins, P., *Inorganic Chemistry*. 3rd ed.; W. H. Freeman and Company: New York, **1999**; p 25.

(4) Vobornik, I.; Perfetti, L.; Zacchigna, M.; Grioni, M.; Margaritondo, G.; Medarde, M.; Lacorre, P., *Phys. Rev. B* **1999,** 60, R8426-R8429.

(5) Torrance, J. B.; Lacorre, P.; Nazzal, A. I.; Ansaldo, E. J.; Niedermayer, C., *Phys. Rev. B* **1992,** 45, 8209-8212.

(6) Demazeau, G.; Marbeuf, A.; Pouchard, M.; Hagenmuller, P., *J. Solid State Chem.* **1971,** 3, 582.

(7) Escote, M. T.; da Silva, A. M. L.; Matos, J. R.; Jardim, R. F., *J. Solid State. Chem.* **2000,** 151, 298-307.

(8) Vassiliou, J. K.; Hornbostel, M.; Ziebarth, R.; Disalvo, F. J., *J. Solid State Chem* **1989,** 81, 208-216.

(9) Lessing, P. A., *Ceram. Bull.* **1989,** 68, 1002-1007.

(10) Lacorre, P.; Torrance, J. B.; Pannietier, J.; Nazzal, A. I.; Wang, P. W.; Huang, T. C., *J. Solid State. Chem.* **1991**.

(11) Blasco, J.; Castro, M.; Garcia, J., *J. Phys.: Condens. Matter* **1994,** 6, 5875-5889.

(12) Tiwari, A.; Rajeev, K. P., *Mod. Phys. Lett. B* **1997,** 11, 1161-1167.

(13) Fernandes, J. D. G.; Araujo Melo, D. M.; Zinner, L. B.; Salustiano, C. M.; Silva, Z. R.; Alves Junior, C.; da Costa, J. A. P.; Longo, E., *J. Alloys Compd.* **2002,** 344, 157-160.

(14) Jade; Inc., M. D., *XRD Pattern Processing* **1999**.

(15) *PDF # 41-0344.*

(16) Cullity, B. D., *Elements of X-Ray Diffraction*. ed.; Addison-Wesly: Massachuesetts, **1978**; p.

CHAPTER 6

Final Comments and Future Directions

I. Application of Template Synthesis to WO_3 and Fluorocarbon Fibers

The successful demonstrations of template synthesis of one-dimensional materials have initiated several new investigations on size and dimensionality of materials. Chapter 5 reviewed the preliminary results for the investigation on the rare earth nickelates and is the beginning phase in the study of nickelate and tungstenate materials. The nickelates, with the exception of $LaNiO_2$ nanotubes, have not been studied in nanowire form. The physical properties of the nickelates range from thermoelectricity, ionic conductivity, electrochromic behavior, and magnetism.[1,2] The tungenates are another class of materials that exhibit electrochromic behavior, which make them attractive for sensor applications.[3]

The synthetic routes described in Chapter 2 have been applied to WO_3. Both AAO and PC templates were used in conjunction with the sol-gel solution preparation also described in Chapter 2. A previous report on the formation of WO_3 nanotubes prepared from the AAO template was initially examined.[4] Through EDS and XPS analysis, the method of removing the template from an epoxy film had dissolved the WO_3. Elemental analysis verified that fiber structures left-behind were composed of epoxy. WO_3 nanotubes was probably formed within the AAO template, and may have drawn up the epoxy while it was still a gel. However, WO_3 is soluble in alkaline solutions and was removed during the dissolution process.[5] The PC template was also used to form WO_3 fibers. The SEM image, Figure 6.1, of WO_3 calcined at 650 °C reveal fibers composed of large grains. The PXRD pattern, Figure 6.2, indicates that it is a mixed phase of monoclinic and orthorhombic WO_3. These results suggest that the calcination temperature should be modified to obtain single-phase material.

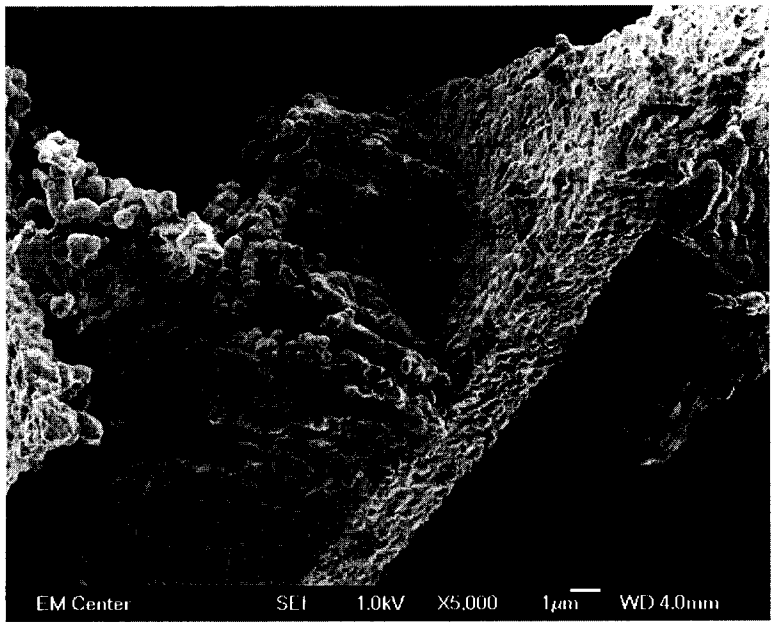

Figure 6.1. SEM image of WO_3 nanofibers attached to a surface film. Sample was calcined at 650 °C.

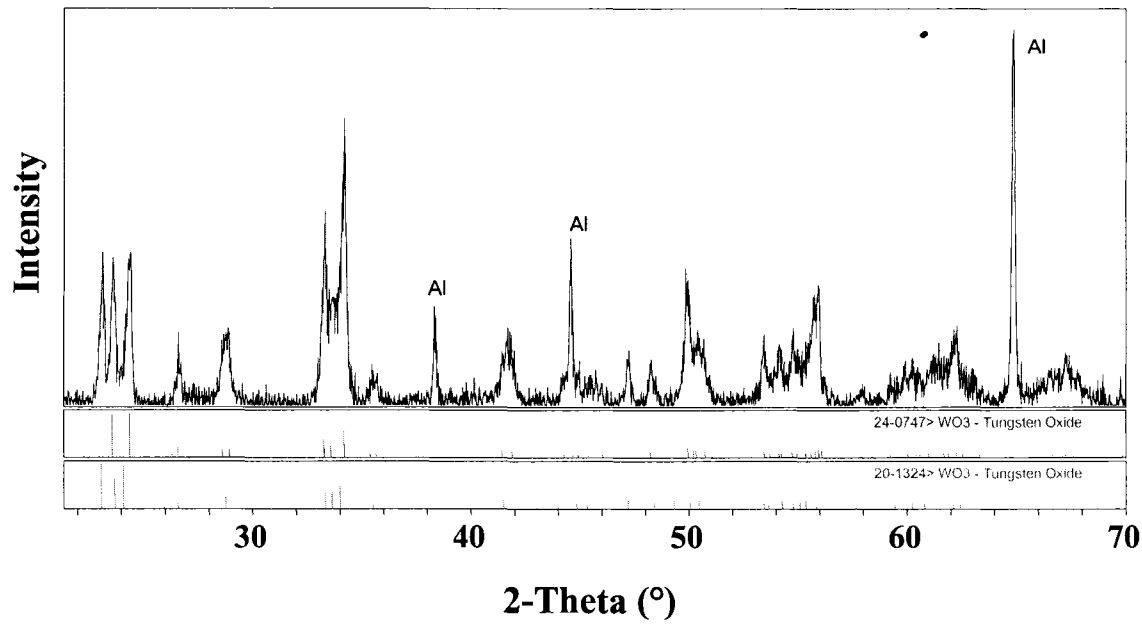

Figure 6.2. PXRD of Bulk WO_3 powder calcined at 700 °C. Sample was mounted in an aluminum holder.

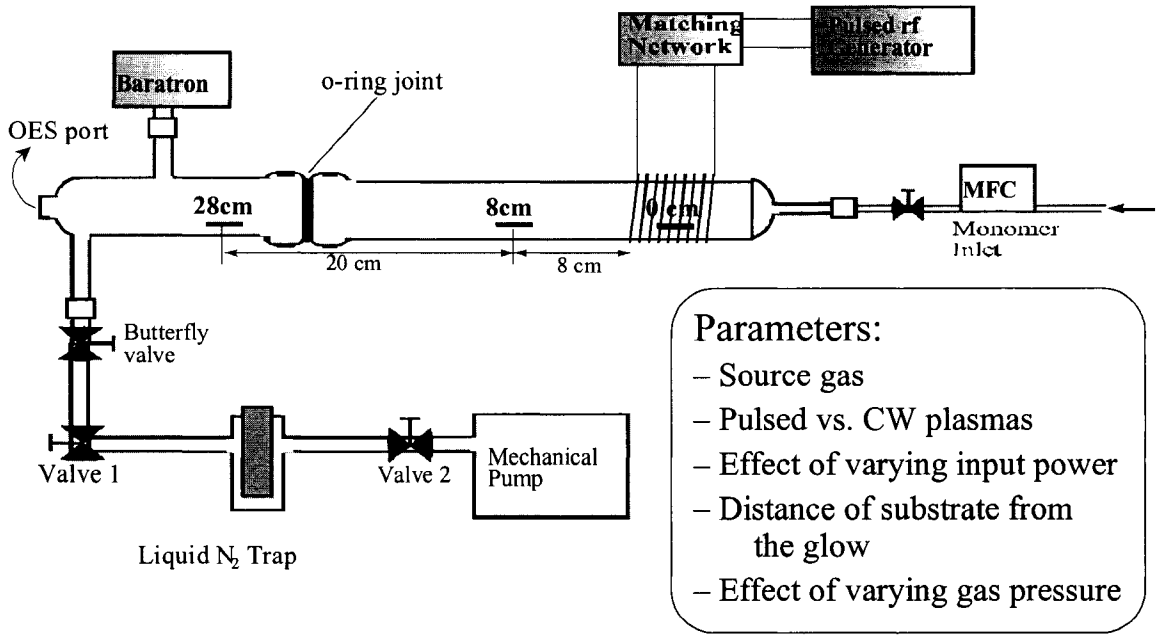

Figure 6.3. Plasma reactor used for C_4F_8 depositions to reduce template pore diameter.

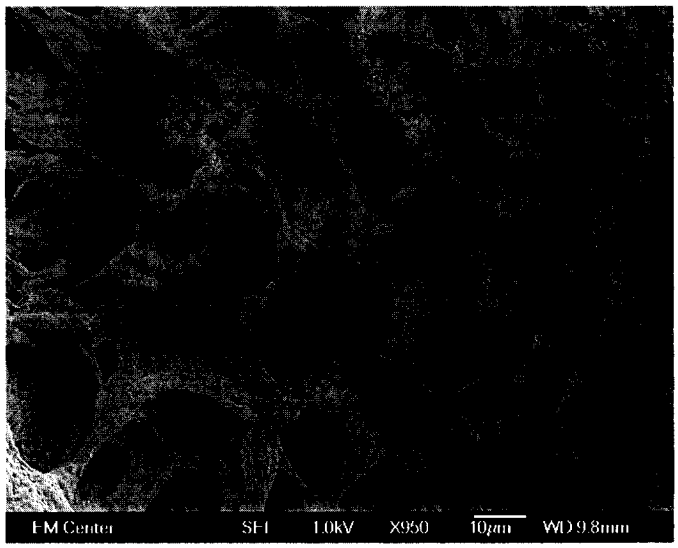

Figure 6.4. SEM of fluorocarbon nanofibers formed from within the AAO template.

The Fisher and Dorhout research groups are also interested in synthesizing composite materials. A preliminary investigation on changing the aspect ratio of the AAO templates included the filling of the pore channel to reduce the diameter. The material used to fill the channel was a flurocarbon polymer using plasma deposition with C_4F_8 as the monomer gas. Figure 6.3, is a schematic of the plasma reactor used in this study. AAO templates were placed at 0, 8, and 28 cm downstream from the plasma glow. An applied rf power of 25 W and deposition times of 10 minutes to 1 hour led to the formation of flurocarbon nanofibers, Figure 6.4. The structures formed here may be modified to form tubes and be used in composite materials.

II. Future Directions and Final Conclusions

The template assisted growth of 1-D perovskites using commercially available track-etched polycarbonate and anodized aluminum oxide membranes proved to be a successful method in fabricating models for the investigation on size effects. The synthetic methods developed for this research produced the first perovskite nanotubes and nanofibers resembling strings-of-grains. Reaction conditions affected the morphologies formed within templates, demonstrated the effectiveness of controlling grain size and shape not previously observed with powder processing methods. And the utility of this method enabled the systematic investigation on size effects not previously demonstrated. Tubes formed from the AAO template were found to be a possible storage material for solvents. Ultimately, One drawback to this synthetic technique is the surface film generated by the coating process. However, the beneficial side to having the nanostructures attached to a surface film is the formation of nanostructured arrays on

micron thick films. 1-D materials are currently being sought as interconnects for the electronics industry and there is a need to connect nanoscale materials to micron scale materials.[6]

In Chapter 3 the nanostructures were used to systematically study size effects on polarization; the proposed explanations for the effects of particle size on the ferroelectric properties are depolarization effects, the absence of long-range cooperative interactions, structural defects, elastics constraints, and surface tension effects.[7] Analysis of the crystal chemistry was performed with PXRD and Raman spectroscopy, and the enthalpy of phase transitions was monitored with DSC. Results from this study were able to rule out surface tension effects as a cause for decreasing ferroelectric properties. Structural analysis using Raman probed the symmetry of the Bravais Lattice within crystallite sizes of 13-157 nm and demonstrated that they possessed the non-centrosymmetric phase required for ferro- and antiferroelectric polarization. The E1(TO) soft mode behavior examined, as a function of crystallite size, had minor shifts in frequency. Relative to high-pressure experiments, the results indicate that the crystallites were not under hydrostatic pressures of 1-2 GPa. Observation of the tetragonal symmetry for nanotubes with 11 nm crystallite size led the conclusion that distortion around Ti^{+4} is more relevant to ferroelectric mechanism than surface considerations.

Another hypothesis to evaluate with our 1-D perovskites, is that structural defects within the grain boundaries of the nanomaterials cause a decrease in ferroelectric properties. Recently, high resolution TEM (HRTEM) was used to identify twinning, intergrowth defects, and phase separations within 10 nm diameter particles of $BaTiO_3$.[8] Jaing et al. concluded that chemical defects, not surface depolarization, caused the

reduction in ferroelectricity through retention of the cubic symmetry in nanocrystalline materials. A natural progression of this research on 1-D materials would be the analysis of crystalline defects. Analysis of the synthetic procedures described in Chapter 2 on the crystallites should be investigated to verify if synthetic conditions could be modified to control the crystal chemistry. Based on the grain sizes observed with nanotubes formed from the AAO template (< 20 nm), these structures would be suitable for evaluation with HRTEM. This investigation would fall under the key goal of controlling composition, size, and crystallinity of nanomaterials through chemistry.[9]

Overall, the investigation on the crystal chemistry and dimensionality of the perovskites synthesized in this research illustrated that neither crystallite size nor aspect ratio influenced the electronic properties for the range of materials examined. Due to the length scales and aspect ratios of the templates used, formation of morphologies with polycrystalline grains were observed. Simply put, the template pores were too large to facilitate the growth of single crystalline nanorods or wires to prove otherwise. Evidence for this conclusion was based on observing no significant deviations in structure-property relationships analyzed through in band gap energies, transition temperatures, and enthalpy, and crystalline symmetry between the nanostructures formed in PC templates and the control powders. Further analysis on nanotubes formed within AAO templates is needed to verify if this hypothesis is accurate.

Finally, application of AAO templates with 20 nm pore sizes from Nanomaterials Research Corp, and from the group of Thomas Mallouk, along with 20 nm PC templates to the synthetic techniques developed are being investigated in the Fisher-Dorhout

research group. Structures formed from these templates and those demonstrated by Park should help clarify the effects of crystallite size

References

(1) Blasco, J.; Castro, M.; Garcia, J., *J. Phys.: Condens. Matter* **1994,** 6, 5875-5889.

(2) Tiwari, A.; Rajeev, K. P., *Mod. Phys. Lett. B* **1997,** 11, 1161-1167.

(3) Nishide, T.; Yamaguchi, H.; Mizukami, F., *J. Mater. Sci.* **1995,** 30, 4946.

(4) Lakshmi, B. B.; Dorhout, P. K.; Martin, C. R., *Chem. Mater.* **1997,** 9, 857-862.

(5) Physical Constants of Inorganic Compounds. In *CRC Handbook of Chemistry and Physics*, 76th ed.; CRC Press: Boca Raton, **1995**;pp 4-93.

(6) Dai, Z. R.; Pan, W. Z.; Wang, Z. L., *Adv. Funct. Mater.* **2003,** 13, 9-20.

(7) Frey, M. H.; Payne, D. A., *Phys. Rev. B.* **1996,** 54, 3158-3168.

(8) Jiang, B.; Peng, J. L.; Bursill, L. A.; Zhong, W. L., *J. Appl. Phys.* **2000,** 87, 3462-3467.

(9) Rao, C. N. R.; Deepak, F. L.; Gundiah, G.; Govindaraj, A., *Prog. Solid State Chem.* **2003,** 31, 5-147.